

UNIVERSITÀ DEGLI STUDI DI NAPOLI FEDERICO II

DOTTORATO IN INGEGNERIA INDUSTRIALE – XXXV CICLO

Settore Scientifico Disciplinare: ING-IND/05  
Impianti e Sistemi Aerospaziali

# **GNC AND IMAGING APPROACHES FOR MINI-UAV BASED RADAR**

**Giuseppe Esposito**

## **Relatore**

Prof. Ing. Giancarmine Fasano

## **Tutori**

Ing. Ilaria Catapano

Ing. Francesco Soldovieri

## **Coordinatore**

Prof. Ing. Michele Grassi



# Keywords

UAV, Radar, GPR, Radar Imaging, Signal Processing, Inverse Scattering, Microwave Tomography, TSVD, Motion Compensation, GNSS, CDGPS, Flight Tests, Experimental Results.

# Abstract

Radar imaging from Unmanned Aerial Vehicles (UAVs) is a dynamic research topic attracting huge interest due to its practical fallouts. This thesis deals with mini-UAV based radar imaging and faces several open issues related to surface and subsurface imaging from microwave data collected by a radar system mounted on board a mini UAV.

Initially, a brief review of the radar imaging technologies dealing with the state of the art systems, the required hardware components and the applicative fields is presented.

Thereafter, the main open issues are introduced. These are: 1) the need for effective filtering strategies to reduce the clutter; 2) the need for accurate UAV positions estimation during the data acquisition; 3) the need for obtaining from radar data accurate and high resolution images of the observed scene, while keeping acceptable the computing times and the computer resources in terms of memory space and processor velocity. In this regard, this thesis reviews the data filtering procedures commonly adopted in Time Domain (TD) Ground Penetrating Radar (GPR) literature, it analyses different possible solutions for obtaining accurate UAV positioning information, and proposes two different strategies to account for the UAV positioning estimates. Both the strategies, referred to as Strategy 'A' and Strategy 'B' respectively, use filtering strategies operating in time domain, the Fast Fourier Transform to transform data in the frequency domain, and a microwave tomography approach to process data. This latter addresses the imaging as a linearized inverse scattering problem. As said, the strategies differ from each other in the way they account for UAV positioning information.

Strategy 'A' implements a Motion Compensation (MoCo) step that accounts for the UAV motion deviations with respect to nominal trajectory and exploits the UAV positioning information to realign the radar data and ensure their uniform spacing along a straight trajectory. This strategy also involves the use of the 'Shift and Zoom' procedure to improve the computational efficiency of the microwave tomographic (MWT) approach adopted to face the radar imaging problem. The Shift and Zoom consists in dividing the observation domain and the investigation one into smaller and

partially overlapping subdomains in which the MWT approach is used to obtain tomographic reconstructions that are then combined together to obtain the reconstruction of the entire domain under test. It should be noted that having data uniformly spaced along a straight trajectory at constant altitude and using the 'Shift and Zoom' approach allow a particularly efficient implementation of MWT because it is sufficient to calculate the scattering operator, i.e. the mathematical operator linking the data and the unknown, once and for reduced dimensions of the observation domain and the investigation one.

Strategy 'B', conversely, uses the platform positioning data directly into the reconstruction step, i.e. in the implementation of the MWT approach. This avoids possible data alterations due to the resampling and the interpolation required by the MoCo step of Strategy 'A'. In addition, Strategy 'B' is suitable for arbitrary flight geometries, i.e. not only for straight trajectories.

It is worth noting that both strategies 'A' and 'B' have been used to process experimental data.

A further, and maybe most important, contribute of this thesis regards the design of MWT approaches to face the imaging of surface or subsurface targets from radar data collected by using a mini UAV as observation platform. It is worth pointing out that the radar imaging problem has been addressed in the case of two-dimensional geometry considering both the vertical imaging plane, i.e. the plane defined by the flight path and the pointing direction of the transmitting and receiving antennas, and the horizontal imaging plane, i.e. the plane at constant altitude. Accordingly, after a brief review of the basic concepts regarding MWT, the approaches developed during the PhD activity are presented. These MWT approaches differ from each other for the scattering model adopted to describe signal propagation while using the same mathematical tools to solve the inverse scattering problem and allowing the exploitation of some figures of merit for analysing the achievable spatial resolution limits.

In this frame, a strategy called MIA (Multiline Imaging Approach) is also proposed. MIA considers the imaging in the vertical plane and exploits the radar data collected on one or more measurement lines to reconstruct 2D domains (slices), which are then interpolated to provide a pseudo-3D representation of the investigated volume.

The computational burden of MIA is significantly reduced compared to that required by a full 3D approach.

This thesis also envisages the use of UAV radar systems for inspections of surface and subsurface scenarios. Specifically, two high frequency radar systems are considered, referred to as System HI and System HII, and two low frequency radar systems, System LI and System LII. These systems were used in various measurement campaigns concerning objects placed on the surface (Systems HI and HII) and buried (Systems LI and LII) and the acquired radar data were used for the experimental validation of the proposed strategies and of the designed MWT approaches.

Specifically, Strategy 'A' was successfully tested on radar data acquired through the System HI and allowed the comparison of radar imaging performance when using standalone and differential Global Navigation Satellite System (GNSS) positioning information. In this case the Strategy 'A' was implemented by using the MWT approach based on the vertical imaging model for free-space propagation.

Strategy 'B' was tested both on high-frequency radar data acquired via System HI, and on low-frequency radar data acquired via System LI. In the first case, Strategy 'B' was implemented by exploiting a MWT approach formulating the imaging in the horizontal plane and considering the electromagnetic propagation model in free space. Moreover, the reconstruction capabilities of the system were analysed showing the effect of the radar parameters, i.e. the flight altitude and the spatial offset between antennas and targets, on the resolution limits, and the consistency of the results with the theoretical resolution limits was demonstrated. Results also demonstrated that when a target is observed off-nadir, a slightly curved trajectory can help distinguishing the real target from the ghost target related to left-right ambiguity. In the second case, Strategy 'B' was implemented by using a MWT approach formulating the imaging in the vertical plane and considering the presence of the air-ground interface. Specifically, among the vertical imaging models proposed for the subsurface propagation, the Equivalent Permittivity (EP) model was used to describe the electromagnetic propagation in a non-homogeneous medium. The obtained results validate the ability to identify and locate buried objects, specifically a metal plate placed about 30 cm below the air-ground interface.

The MIA strategy was tested on the data acquired via System HII at the archaeological park of Paestum and Velia and the obtained results demonstrated good ability to focus and localize the targets in the investigated scene.

Finally, this thesis reports some preliminary results referred to the System LII, which was designed and realized during the abroad PhD period. The System LII was realized by using a Vector Network Analyzer (VNA), was calibrated by performing reference measurements, and was tested by inspecting the internal structure of a concrete wall. The obtained experimental results were compared with results obtained from numerical simulations.

# Table of Contents

Keywords .....	i
Abstract .....	ii
Table of Contents .....	vi
List of Figures .....	viii
List of Tables.....	xii
Acronyms .....	xiii
<b>Chapter 1: Introduction.....</b>	<b>1</b>
1.1 Thesis Outline .....	3
<b>Chapter 2: UAV-based Radar imaging: State of the Art .....</b>	<b>7</b>
2.1 Systems .....	7
2.2 Hardware Design.....	16
2.3 Applications .....	17
<b>Chapter 3: Radar Imaging from UAV .....</b>	<b>25</b>
3.1 Radar Clutter and Filtering Operations .....	25
3.2 UAV Positioning.....	27
3.3 Radar Data Processing Chains .....	29
<b>Chapter 4: Microwave Tomography: Fundamentals .....</b>	<b>36</b>
4.1 Basics of Radar Imaging .....	36
4.2 Integral Formulation of the Scattering Equations .....	39
4.3 Linear MWT .....	41
4.4 Figures of Merit for Resolution Analysis.....	45
<b>Chapter 5: UAV-based Radar Imaging via MWT .....</b>	<b>47</b>
5.1 Vertical imaging model for Free-Space Propagation.....	47
5.2 Vertical Imaging Models for Sub-Superficial Propagation.....	49
5.3 Multilines Imaging Approach (MIA).....	53
5.4 Horizontal Imaging Model for Free Space Scenario.....	57
<b>Chapter 6: High Frequency Radar Imaging System by UAV.....</b>	<b>59</b>
6.1 Developed Prototypes .....	59
6.2 Experimental Results .....	62
<b>Chapter 7: Low Frequency Radar Imaging Systems by UAV .....</b>	<b>98</b>
7.1 UAV-based GPR systems .....	98
7.2 Subsurface Imaging with System LI.....	101
7.3 Preliminary Results with System LII.....	104
<b>Chapter 8: Conclusions.....</b>	<b>113</b>

**Bibliography** ..... 117

# List of Figures

<b>Figure 1.</b> Picture of the UAV-GPR system developed at University of Oviedo, Gijon, Spain. ....	9
<b>Figure 2.</b> Picture of the UAV GPR system developed at the Department of Industrial Engineering (DII) of University of Naples “Federico II” .....	10
<b>Figure 3.</b> Picture of the UAV GPR system developed at the Deutsches Zentrum für Luft- und Raumfahrt (DLR), Germany. ....	11
<b>Figure 4.</b> Picture of the UAV GPR system developed at University of Maribor, Maribor, Slovenia. (a) UAV platform; (b) transceiver module; (c) cable interconnections. ....	12
<b>Figure 5.</b> Picture of the UAV GPR System developed by the Dyrecta Lab., Conversano, Italy. ....	12
<b>Figure 6.</b> Radar data processing chain: strategy ‘A’. ....	30
<b>Figure 7.</b> The Unmanned Aerial Vehicle (UAV)-borne radar imaging system, (a) actual imaging scenario; (b) starting schematic configuration; (c) schematic configuration after range alignment; (d) schematic configuration after along-track interpolation. ....	32
<b>Figure 8.</b> Shift and Zoom Algorithm Description for Vertical Imaging. ....	34
<b>Figure 9.</b> Direct use of GNSS positioning information into the MWT imaging step: Strategy ‘B’. ....	35
<b>Figure 10.</b> (a) A-scan. (b) B-scan (i.e. radargram). ....	38
<b>Figure 11.</b> Focused radar image. ....	38
<b>Figure 12.</b> Radar imaging scenario. ....	40
<b>Figure 13.</b> UAV-based radar imaging. Vertical imaging for superficial scenario. ....	48
<b>Figure 14.</b> GPR imaging scenario characterized by a two-layered medium: the upper half space ( $z < 0$ ) is air, while the lower half space ( $z > 0$ ) is soil, which is assumed to be homogeneous. The antennas move along a rectilinear path $\Gamma$ at a constant height $h$ . IRP stands for Interface Reflection Point. ....	50
<b>Figure 15.</b> Multilines imaging scenario. ....	54
<b>Figure 16.</b> MIA strategy flowchart. ....	56
<b>Figure 17.</b> UAV-based radar imaging. Horizontal imaging scenario. ....	57
<b>Figure 18.</b> Discretization of the UAV-based radar horizontal imaging problem. ....	58
<b>Figure 19.</b> M-UAV radar imaging system (System HI): (a) DJI F550 hexacopter with onboard equipment; (b) ground-based GPS station. ....	60
<b>Figure 20.</b> System HII. (a) DJI S900 hexacopter with onboard equipment. (b) Components of the payload. (c) Payload architecture. ....	62

<b>Figure 21.</b> First test case: radar imaging scenario.....	63
<b>Figure 22.</b> Test 1-Track 1: (a) raw data; (b) east–north UAV positions estimated by GPS (solid blue line) and CDGPS (solid red line), along-track direction defined by GPS (dashed blue line) and CDGPS (dashed red line); (c) UAV Altitude estimated by GPS (solid blue line) and CDGPS (solid red line), average altitude defined by GPS (dashed blue line) and CDGPS (dashed red line).....	64
<b>Figure 23.</b> Test 1-Track 2: (a) raw data; (b) east–north UAV positions estimated by GPS (solid blue line) and CDGPS (solid red line), along-track direction defined by GPS (dashed blue line) and CDGPS (dashed red line); (c) UAV Altitude estimated by GPS (solid blue line) and CDGPS (solid red line), average altitude defined by GPS (dashed blue line) and CDGPS (dashed red line).....	65
<b>Figure 24.</b> Processed radargram Test 1-Track 1: (a) aligned ad interpolated radargram by exploiting GPS information and after filtering operations; (b) aligned ad interpolated radargram by exploiting CDGPS information and after filtering operations.....	66
<b>Figure 25.</b> Processed radargram Test 1-Track 2: (a) aligned ad interpolated radargram by exploiting GPS information and after filtering operations; (b) aligned ad interpolated radargram by exploiting CDGPS information and after filtering operations.....	67
<b>Figure 26.</b> Tomographic images Test 1-Track 1 obtained by Shift and Zoom TSVD algorithm: (a) GPS based motion compensation (MoCo); (b) CDGPS based MoCo. ....	69
<b>Figure 27.</b> Tomographic images Test 1-Track 2 obtained by Shift and Zoom TSVD algorithm: (a) GPS based MoCo; (b) CDGPS based MoCo.....	69
<b>Figure 28.</b> Measurement scenario. ....	70
<b>Figure 29.</b> Track 1. (a) Raw data.(b) East–north UAV positions estimated by GPS (solid blue line) and CDGPS (solid red line), along-track direction defined by GPS (dashed blue line) and CDGPS (dashed red line). (c) UAV Altitude estimated by GPS (solid blue line) and CDGPS (solid red line), average altitude defined by GPS (dashed blue line) and CDGPS (dashed red line).....	72
<b>Figure 30.</b> Track 2. (a) Raw data; (b) East–north UAV positions estimated by GPS (solid blue line) and CDGPS (solid red line), along-track direction defined by GPS (dashed blue line) and CDGPS (dashed red line). (c) UAV Altitude estimated by GPS (solid blue line) and CDGPS (solid red line), average altitude defined by GPS (dashed blue line) and CDGPS (dashed red line).....	73
<b>Figure 31.</b> Tomographic images for the Track 1 obtained by Shift and Zoom TSVD algorithm: (a) GPS based MoCo; (b) CDGPS based MoCo.....	75
<b>Figure 32.</b> Tomographic images of Track 2 obtained by Shift and Zoom TSVD algorithm: (a) GPS based MoCo; (b) CDGPS based MoCo. ....	75

<b>Figure 33.</b> Map of the investigated area. Base layer: Google Earth and picture of the area. ....	78
<b>Figure 34.</b> Raw radargram for the overall flight. ....	79
<b>Figure 35.</b> Multilines trajectories $\Gamma k$ (red) and investigated domains $D_i$ (blue). ....	80
<b>Figure 36.</b> Tomographic reconstruction of the investigated volume $V$ at constant $z$ -slice: (Left) $z = 3.29$ m, (Center) $z = 2.58$ m, and (Right) $z = 1.37$ m. ....	81
<b>Figure 37.</b> Binary tomographic reconstruction of the investigated volume $V$ at constant $z$ -slice overlapped with Google Earth image: (Left) $z = 3.29$ m, (Center) $z = 2.58$ m, and (Right) $z = 1.37$ m. ....	81
<b>Figure 38.</b> Tomographic reconstruction of the investigated volume $V$ at constant $y$ -slice: $y=11$ m. ....	82
<b>Figure 39.</b> Single measurement line and horizontal imaging plane scenario. ....	82
<b>Figure 40.</b> Radar imaging with an ideal rectilinear flight path: (a) 3D view; (b) view in the $y$ - $z$ plane. ....	84
<b>Figure 41.</b> Contour plot of the across-track resolution $\Delta y$ versus $d$ and $h$ , expressed in meters, in the case of a rectilinear flight trajectory. ....	85
<b>Figure 42.</b> Point spread function (PSF) amplitude for a flight altitude $h = 5$ m: ideal rectilinear trajectory and point like target with offset: (a) $d = 0$ m, (b) $d = 2$ m. Curved trajectory as described by Equation (4.10) and point-like target located with offset: (c, e) $d = 0$ m, (d, f) $d = 2$ m. The white dashed line represents the trajectory and the white circle denotes the target. ....	86
<b>Figure 43.</b> PSF amplitude for $h = 10$ m and a curved trajectory: (a) point like target at $d = 0$ ; (b) point like target at $d = 2$ . The white dashed line shows the trajectory; the white circle denotes the target. ....	87
<b>Figure 44.</b> Reconstruction of a point target on image planes at different elevations. The true target (black triangle) is illuminated at the radar nadir and its reconstruction is represented by the red rectangles. ....	89
<b>Figure 45.</b> Reconstruction results in a three-target scenario (a) image plane at $z = 0$ m; (b) image plane at $z = 0.2$ m; (c) image plane at $z = 0.4$ m ....	90
<b>Figure 46.</b> The UAV-borne radar imaging scenario. ....	92
<b>Figure 47.</b> Raw radargrams. (a) Track 1; (b) Track 2. The white dotted line represents the variable UAV flight altitude $h$ estimated by the CDGPS and transformed into the equivalent travel time by: $th = 2h/c_0$ . ....	94
<b>Figure 48.</b> Filtered radargrams: (a) Track 1; (b) Track 2. The white dotted line represents the variable UAV flight altitude $h$ estimated by the CDGPS and transformed in the equivalent travel time by: $th = 2h/c_0$ . ....	95

<b>Figure 49.</b> Focused image of the scenario under test: (a) Track 1; (b) Track 2. The dotted white line represents the flight path as projected onto the investigated domain. ....	96
<b>Figure 50.</b> System LI. ....	99
<b>Figure 51.</b> System LII. Components connection. ....	100
<b>Figure 52.</b> System LII. ....	100
<b>Figure 53.</b> Experimental test site: (a) aerial view of the area with UAV flight trajectory (red line) and target (black rectangle) superimposed; (b) photo of the buried metal plate. ....	101
<b>Figure 54.</b> Signal processing scheme for data acquired with System LI. ....	102
<b>Figure 55.</b> UAV GPR raw radargram. ....	102
<b>Figure 56.</b> UAV GPR filtered radargram. ....	103
<b>Figure 57.</b> Focused image. ....	104
<b>Figure 58.</b> Metallic target with a rectangular cross-section. ....	105
<b>Figure 59.</b> A-scan without target. ....	105
<b>Figure 60.</b> A-scan with the target. ....	106
<b>Figure 61.</b> Difference between the A-scan with target and the A-scan without target. ....	106
<b>Figure 62.</b> Radargram of the signal difference. ....	107
<b>Figure 63.</b> Target at 88cm: (a) Difference between the A-scan with target and the A-scan without target. (b) Radargram of the signals difference. ....	107
<b>Figure 64.</b> Target at 128cm: (a) Difference between the A-scan with target and the A-scan without target. (b) Radargram of the signal difference. .....	108
<b>Figure 65.</b> High Bay Lab concrete wall with buried reinforced rebars. ....	109
<b>Figure 66.</b> Horizontal slice of the wall. ....	109
<b>Figure 67.</b> Measured results. ....	110
<b>Figure 68.</b> Simulated scenario. ....	111
<b>Figure 69.</b> Simulation results. ....	112

# List of Tables

<b>Table 1.</b> UAV radar imaging systems. ....	13
<b>Table 2.</b> Operative Radar System Parameters: First Test Case. ....	63
<b>Table 3.</b> Signal Processing Parameters: Track 1. ....	68
<b>Table 4.</b> Signal Processing Parameters: Track 2. ....	68
<b>Table 5.</b> Operative radar system parameters ....	71
<b>Table 6.</b> Signal Processing Parameters: Track 1 ....	74
<b>Table 7.</b> Signal Processing Parameters: Track 2 ....	74
<b>Table 8.</b> CDGPS operative conditions.....	76
<b>Table 9.</b> Computational time .....	77
<b>Table 10.</b> MIA implementation parameters.....	80
<b>Table 11.</b> Along- and across-track resolution values. ....	88
<b>Table 12.</b> Estimated and true target positions for different imaging planes.....	91
<b>Table 13.</b> Radar system parameters.....	92
<b>Table 14.</b> Maximum errors of the CDGPS technique. ....	95
<b>Table 15.</b> Along- and across-track resolution values ....	97
<b>Table 16.</b> System LI components and specifications. ....	99
<b>Table 17.</b> System LII components and specifications. ....	100
<b>Table 18.</b> Radar system parameters.....	101
<b>Table 19.</b> Signal-processing parameters.....	103
<b>Table 20.</b> VNA parameters for calibration. ....	105

# Acronyms

UAVs	Unmanned Aerial Vehicles
EM	Electromagnetic
Radar	RAdio Detecting And Ranging
LiDAR	Light Detection And Ranging
GPRs	Ground Penetrating Radars
TD	Time Domain
GNSS	Global Navigation Satellite System
MIA	Multilines Imaging Approach
EP	Equivalent Permittivity
ARTINO	Airborne Radar for Three-dimensional Imaging and Nadir Observation
FHR	Fraunhofer Institute for High-Frequency Physics and Radar Techniques
SAR	Synthetic Aperture Radar
DGPS	Differential Global Positioning System
SDR	Software-Defined Radio
GPS	Global Positioning System
IMU	Inertial Measurement Unit
UWB	Ultra-Wide-Band
FMCW	Frequency-Modulated Continuous-Wave
RTK	Real-Time Kinematic
UWiBaSS	Ultra-Wide-BAnd Snow Sounder
UWB	Ultra-Wide-Band
RHCP	Right-Handed Circular Polarization
LHCP	Left-Handed Circular Polarization
IREA	Institute for the Electromagnetic Sensing of the Environment
CNR	National Research Council of Italy
PCB	Printed Circuit Board
CDGPS	Carrier-phase Differential Global Positioning System
DII	Department of Industrial Engineering
DLR	Deutsches Zentrum für Luft- und Raumfahrt
SFCW	Stepped Frequency Continuous Wave
CBD	Commerce Business Daily
IDS	Ingegneria Dei Sistemi
MIMO	Multi Input Multi Output
DJI	Da-Jiang Innovations
LPY26	Logi-Log Periodic Y26
TEM	Transmission Electron Microscopy
VNA	Vector Network Analyzer
GNC	Guidance, Navigation and Control
CPU	Central Processing Unit
PPK	Post Processing Kinematic
SDR	Software-defined radio
ROC	Receiver-Operating Characteristic
ISAR	Inverse SAR
AP	Anti-Personnel
AT	Anti-Tank
TX	Transmitting

RX	Receiving
PSF	Point Spread Function
SVD	Singular Value Decomposition
DAF	Desired Angular acceleration Function
MWT	Microwave Tomography
MoCo	Motion Compensation
DFT	Discrete Fourier Transform
TSVD	Truncated Singular Value Decomposition
IFT	Inverse Fourier Transform
AI	Artificial Intelligence
SPEC	Spectral Content
MIA	Multiline Imaging Approach
FP	Free-space Propagation
IRP	Interface Reflection Point
SD	Spectral Domain
RB	Ray-Based
EP	Equivalent Permittivity
Lab	Laboratory
WGS84	World Geodetic System 1984
USERE	User Equivalent Range Error
HDOP	Horizontal Dilution of Precision
VDOP	Vertical Dilution of Precision
VESTA	Valorizzazione E Salvaguardia del patrimonio culturale attraverso l'utilizzo di tecnologie innovative
LiPO	Lithium-POLymer
USB	Universal Serial Bus
RAM	Random Access Memory
LAN	Local Area Network
DC	Direct Current
GDOP	Geometric Dilution Of Precision
PDOP	Positional Dilution Of Precision
DPI	Discovery Partners Institute
UIC	University of Illinois at Chicago
LPDA	Log-Periodic Dipole Array
PC	Portable personal Computer
IMAA	Institute of Methodologies for Environmental Analysis
IF	Intermediate Frequency
q.e.d.	quod erat demonstrandum
PEC	Perfect Electric Conductor
RINEX	Receiver Independent Exchange Format
GLONASS	GLObalnaya NAVigatsionnaya Sputnikovaya Sistema
QZSS	Quasi-Zenith Satellite System
SBAS	Space Based Augmentation System
PPP	Precise Point Positioning
E/N/U	East/North/Up

# Chapter 1: Introduction

---

The Unmanned Aerial Vehicles (UAVs), commonly referred to as drones, represent nowadays a widely diffused technology in many different contexts and applications. Many ways of classifying UAVs exist according to the performance characteristics, the working altitude, the endurance, the operative range, the maximum take-off weight, the propulsion system. While UAVs classification is almost uniform for large UAVs, it becomes blurry when trying to distinguish between small, mini and micro UAVs [1]. In accordance with [1], in the following we will refer to rotary UAVs with a maximum take-off weight smaller than 30 Kg as ‘mini UAVs’.

The main advantages of mini UAVs stand in their limited costs, easy use and high flexibility thanks to their vertical take-off and landing capabilities and their ability to hover. Conversely, the main disadvantages are the limited endurance, which typically stands at 20 minutes, and the limited payload mass. Furthermore, depending on the type of application, other aspects can become disadvantageous, such as the non-smooth flight dynamics or the magnetic sensitivity of the on board navigation sensors. However, the prospect of greatly simplifying measurement campaigns by allowing access to challenging areas represents the greatest advantage of this type of technology and is the reason why, despite all the drawbacks mentioned, it has been widely adopted in various fields. Electromagnetic (EM) remote sensing is one of these fields.

EM remote sensing consists in detecting and monitoring the physical characteristics of an area by measuring the emitted and reflected radiation at a certain distance. There are two primary types of remote sensing instruments: active and passive. Passive sensors exploit natural sources, like sun light, and measure energy emitted or reflected from an object. Examples of passive sensors are optical, thermal, infrared, multispectral cameras, electric potential and magnetic sensors. Active sensors are those exploiting their own source to emit the probing wave, which is transmitted from the sensor towards the target of interest, and then reflected back to the sensor. Radar and LiDAR are examples of active sensors.

The word radar stands for RAdio Detecting And Ranging. The radar working principle is similar to the echo principle: extremely short bursts of radio energy traveling at the speed of light are transmitted, reflected off a target and then returned

as an echo. In this way, a radar system can determine the distance (also referred to as ranging), the angle, and the radial velocity of target objects. The main advantage of using radar is that it works in all weather and in day/night conditions, practically overcoming the limits imposed by passive sensors such as optical cameras. Another important feature of radar is that thanks to the ability of electromagnetic waves to penetrate visually opaque materials, they are able to image buried and hidden objects. This is the principle behind ground penetrating radars (GPRs).

Time Domain (TD) GPR systems are commonly used to perform non-destructive surveys of optically opaque media and generate images from which to infer the presence of targets. The raw radar image, also referred to as radargram, is an image where the intensity value associated to each pixel represents the amplitude of the measured component of the backscattered electric field at a certain time instant into the observation time window. The radargram is obtained by moving the antennas along a line, referred to as measurement line or radar track, and it depicts the measurement points on the horizontal axis, and the time of flight that the signal takes going from the antennas to the targets and come back on the vertical axis. Therefore, the objects depicted in the radargram are not represented according to their true shape, but as hyperboles. For this reason, interpretive effort is always required when looking at a radargram.

The joint use of mini UAVs and radar allow us combining the advantages of both technologies. Despite that, new challenges arise. One of this is the necessity of georeferencing radar data. While for traditional on-cart mounted radar systems the process of georeferencing the radar data is managed through odometers, these latter are no more available when UAV platforms are considered. Therefore, new georeferencing techniques are necessary. Note that an incorrect spatial association between the acquired radar tracks and the positions flown by the drone during the measurement results in defocused and delocalized representations of the targets in the radar image.

In this framework, different solutions have been proposed. One of these consists of using a Global Navigation Satellite System (GNSS) for the estimate of the UAV positions during the flight, and then associating each of them to the acquired radar scans. The requirement for a correct georeferencing process is that the accuracy on the UAV positioning estimate is at least smaller than the half of the transmitted radar wavelength. Since standalone GNSS performance are in the order of the meter,

sometimes this kind of technology is not sufficient for guarantying the needed accuracy levels. This is the case of radar systems working at frequencies from some hundred MHz up to a few GHz, which have wavelengths of the order of ten centimetres. In this case, differential GNSS solutions have to be adopted for successful UAV-based radar imaging surveys.

Other challenges, typical of mini UAV-based radar imaging systems, are the radar clutter and the need of effective data processing approaches. These problems typically concern GPR applications and become more relevant when the sensor is mounted on a drone. Indeed, while in the case of traditional on-cart GPR systems the antennas are moved close to the terrain, with UAV-based radar systems the antennas operate at a certain not negligible distance from the ground, which significantly increases radar clutter due to all the objects within the antenna footprint. In addition, for UAV-based radar systems it must be taken into account that the reflection from the air-soil interface as well as the signal attenuation make it difficult to distinguish responses from shallow targets because they give rise to weak backscattered signals masked by other strong signals.

## **1.1 THESIS OUTLINE**

The present thesis deals with mini-UAV based radar imaging and faces several open issues related to surface and subsurface imaging from data collected by means of radar mounted on board a mini UAV. It is organized as follows.

Chapter 2 provides an overview of the mini UAV-based radar imaging systems proposed in the reference literature, describing the state of the art systems, the required hardware components and the applicative contexts.

Chapter 3 faces the main issues affecting radar imaging from UAV, that are: a) the need for effective clutter filtering procedures; b) the need for accurate positioning information of the UAV platform during the radar data acquisition; c) the need for obtaining, from radar data, accurate and high resolution images of the scenario under test, while keeping acceptable the computing times and the computer resources in terms of memory space and processor velocity. In this frame, the Chapter 3 reviews the filtering procedures working in time domain and commonly adopted in GPR literature. Moreover, Chapter 3 deals with some possible UAV flight positions estimation solutions, as standalone Global Positioning System (GPS) and Carrier-phase Differential GPS (CDGPS) techniques, and discuss their accuracy. Chapter 3

also proposes two different strategies to account for the UAV positioning information. Both the strategies, referred to as Strategy ‘A’ and Strategy ‘B’, exploit time domain filtering procedures to reduce clutter, transform radar data in the frequency domain by means of the Fast Fourier Transform and process radar data by using a Microwave Tomography (MWT) approach. Strategy ‘A’ implements the Motion Compensation and the Shift and Zoom approaches; Strategy ‘B’ exploits the accurate UAV positioning information directly into the implementation of the MWT approach. It is worth noting that Strategy ‘A’ and Strategy ‘B’ can be regarded as general tools that can be applied to face different kind of radar imaging problems. Indeed, it is sufficient to change the adopted MWT approach according to the specific imaging problem to be solved. As a consequence, the proposed two strategies allow to face both the vertical and the horizontal 2D imaging of surface or subsurface objects from radar data collected along a single measurement line.

Chapter 4 deals with the fundamentals of radar imaging, the integral formulation of the inverse scattering equations, the linear microwave tomographic approaches and the figures of merit for the resolution analysis. This chapter reviews the mathematical tools adopted in the MWT approaches whose design is presented in Chapter 5.

Chapter 5 deals with the design of new MWT approaches, which consists in the definition of different scattering models for the formulation of superficial and sub-superficial radar imaging problems, both in the vertical plane and in the horizontal one. Therefore, the first part of Chapter 5 presents the scattering models for the formulation of the superficial and the sub-superficial radar imaging problems in the vertical plane defined by the measurement line and the Nadir direction of the transmitting and receiving radar antennas. Then, Chapter 5 tackles the case of data collected along multiple measurement lines and introduces the Multiline Imaging Approach (MIA). Finally, the scattering model adopted to design the MWT approach facing the horizontal imaging in a free-space scenario is described.

Chapter 6 and 7 deal with the experimental validation of the strategies ‘A’, ‘B’ and MIA as well as the different MWT approaches, which can be used inside them. Moreover, these chapters describe the radar systems adopted to collect the experimental data.

Specifically, Chapter 6 deals with two high frequency UAV radar system prototypes, i.e. System HI and System HII. The first part of the chapter describes the

hardware components of the two systems. The second part of the chapter deals with the experimental results obtained by applying strategies ‘A’, ‘B’ and MIA on data acquired in different measurement campaigns. Results about a theoretic analysis of horizontal imaging performances is also presented with the aim of investigating how the reconstruction capabilities of the adopted radar imaging approach are affected by the measurement configuration parameters.

Chapter 7 proposes two different low frequency radar imaging systems suitable to be mounted on UAV, i.e. System LI and System LII. After the description of the hardware components of the two systems, data acquired with System LI are processed with Strategy ‘A’ by implementing the Equivalent Permittivity (EP) Model. Calibration tests and preliminary experimental results obtained with System LII are also presented. Experimental results are compared with numerical results.

Finally, Chapter 8 draws the conclusions of this thesis work.



# Chapter 2: UAV-based Radar imaging: State of the Art

---

This chapter reviews briefly the UAV-borne radar imaging systems operating in down-looking mode proposed in literature so far. Section 2.1 treats the state-of-the-art from a chronological perspective, starting from the first conceptual studies [7] up to the recent commercial systems [21-23]. On the base of the state-of-the-art, Section 2.2 derives an indication about the main components of a typical UAV-based radar imaging system. Section 2.3 provides an overview of the main applicative contexts wherein formerly described UAV radar imaging prototypes are used. These include landmine detection [2], glaciers and snowpack investigations [3], soil moisture mapping [5], search and rescue activities [4] and cultural heritage [6].

## 2.1 SYSTEMS

The first radar imaging system specifically developed for a UAV platform was the Airborne Radar for Three-dimensional Imaging and Nadir Observation (ARTINO) [7], designed at the Fraunhofer Institute for High-Frequency Physics and Radar Techniques (FHR). ARTINO combined the real aperture, made by a linear array of nadir-pointing antennas, with the Synthetic Aperture Radar (SAR) technology spanned by the moving UAV platform. Despite ARTINO had no penetration capabilities, flying at a reference altitude of 200 m, it could illuminate a ground strip width of approximately 230 m producing a 3D image of the scene with a cubic cell resolution of about  $20\text{ cm} \times 20\text{ cm} \times 20\text{ cm}$ . The navigation unit of this system is composed of a differential global positioning system (DGPS) integrated with acceleration sensors and gyroscopes for each axis.

In 2016, at University of Texas, a commercial radar system was mounted on board a micro-UAV platform coupled with an optical camera. The radar module was the ultra-wideband Pulson P410 sensor operating in the frequency range of 3.1–5.3 GHz, which achieves a 10 cm range resolution. This system [8] also lacked penetration capabilities and it was tested with superficial detection purposes looking for cars, people and trees.

In 2017, a research group at the Pontificia Universidad Javeriana in Colombia designed a custom lightweight GPR based on the Software-Defined Radio (SDR) technology [9]. This System was equipped with two Vivaldi Antipodal antennas characterized by a symmetrical radiation pattern in the frequency range of 1.5–9.0 GHz, mounted in bistatic configuration with an inclination of 45°. Thanks to the navigation control unit made up of GPS (Global Positioning System), IMU (Inertial Measurement Unit) and laser sensor, the system was able to fly steadily at 50 cm above the ground.

In 2018, an Ultra-Wide-Band (UWB) GPR system [10] developed by the University of Ulm was designed for landmine detection in collaboration with Endress and Hauser GmbH company and the University of Applied Sciences and Arts of Northwestern in Switzerland. The GPR front-end was based on the Frequency-Modulated Continuous-Wave (FMCW) technology, working in the frequency range of 1–4 GHz. The GPR was equipped with two lightweight 3D-printed horn antennas (1 TX and 1 RX), which could operate both in standard down-looking and side-looking modes. This system uses a Real-Time Kinematic (RTK) Global Navigation Satellite System (GNSS) module interconnected with the UAV autopilot in order to follow the planned path and correct the position deviations in real time. In addition, the GPR and the navigation devices are connected with the data logger, which stores the data and provides a time stamp to each measurement, thus ensuring the data synchronization.

Another system developed in 2018 is the Ultra-Wide-Band Snow Sounder (UWiBaSS) GPR developed by Norut Northern Research Institute for snowpack surveying [3]. The radar module was the M-Sequence UWB sensor developed by the German company ILMSENS (<https://www.uwb-shop.com/>, accessed on 9 June 2022) with a weight of 4 kg. This sensor can perform two parallel acquisitions by exploiting two receiving channels controlled by an on-board computer with customized software. The GPR is equipped with one transmitting spiral antenna and two receiving Vivaldi antennas mounted with 90 degrees offset one to each other. This experimental set-up allowed the detection of phase differences between the target radar cross-sections. The measurement bandwidth was equal to 5.05 GHz and covered the frequency range of 0.95–6 GHz. The radar module could achieve a 5 cm range resolution in the air with an unambiguous range of 5.75 m. This system exploited the Kraken octocopter as a UAV platform, which allowed a maximum take-off weight of 20 kg; the weight of the empty system is 8.5 kg, while the maximum payload mass is about 11.5 kg. This

system includes a LIDAR, a GPS receiver, and a RTK module as auxiliary navigation devices. The LIDAR is mounted on one of the eight arms of the UAV and accurately tracks the range distance from the ground.

The research group at University of Oviedo gave a significant contribution to the research theme of UAV-based radar imaging too. In 2018, in conjunct work with Universities of Madrid and Vigo, they exploited a custom version of DJI Spreading Wings S1000 as a UAV platform [11] (Figure 1). This last could support a maximum payload of 6 kg and can fly for 15 min with a 2 - 3Kg weight. The employed radar sensor was the Pulson P410 UWB module, already described before, equipped with two customized helix antennas, one having right-handed circular polarization (RHCP), and the other left-handed circular polarization (LHCP). Concerning UAV positioning and geo-referring system, a single-band RTK module providing cm-level accuracy was selected. In 2019, in [12], they proposed significant improvements to the previous system, i.e. a radar unit working at a considerably lower frequency with respect to the Pulson P410 radar and an enhanced positioning system, whose accuracy was greatly increased. Regarding the radar subsystem, an M-sequence Ultra-Wide-Band (UWB) radar covering a frequency range from 100 MHz to 6 GHz was selected. It was equipped with two Vivaldi Antennas working from 600 MHz to 6 GHz. Regarding the positioning system, a dual-band multi-constellation RTK system was selected with expected accuracy of 0.5 cm in the horizontal plane and 1 cm in the vertical direction. Recently this system was equipped with two log-periodic antennas [13].



**Figure 1.** Picture of the UAV-GPR system developed at University of Oviedo, Gijon, Spain.

In 2018, the collaboration between the Institute for the Electromagnetic Sensing of the Environment (IREA) of the National Research Council of Italy (CNR)

and the University of Naples “Federico II” led to the development of a UAV-born GPR prototype [14] based on a custom DJI F550 hexacopter allowing for a maximum payload mass of 1 kg (Figure 2). The UAV was equipped with the Pulson P440 radar module, which was the updated version of the Pulson P410 cited before. The radar was equipped with two log-periodic PCB antennas (Ramsey LPY26) one transmitting and one receiving, operating in down-looking mode. The system was recently upgraded [15] thanks to the use of a ground-based GNSS station allowing for the implementation of the Carrier-phase Differential GPS (CDGPS) technique, which allowed achieving centimetre level accuracy in the UAV positioning estimate. This system lacked penetration capabilities and it was exploited to investigate how GNSS-radar data association affects the objects localization, which was performed by developing ad hoc microwave tomographic approach.



**Figure 2.** Picture of the UAV GPR system developed at the Department of Industrial Engineering (DII) of University of Naples “Federico II”.

Still in 2018, the collaboration between the German Aerospace Center (DLR) and the Karlsruhe Institute of Technology led to a customized version of the DJI® Matrice 600 pro equipped with a FMCW radar module operating in the frequency interval 500 MHz–3GHz [16] (Figure 3). The system was equipped with two Vivaldi Antennas operating in bistatic configuration with a beam-width of about 70 degrees in the azimuth plane. This system was able to operate in both SAR stripmap mode and circular mode. In the SAR stripmap mode it provided a 2D image with a 6 cm × 6 cm range and azimuth resolutions, respectively, while in the circular mode it allowed to achieve a 3D radar image with resolutions of about 4 cm × 4 cm × 4 cm. This system was also designed to send all data (radar, camera, and navigation data) to a ground station by exploiting a 433 MHz data link allowing for the reception of the SAR image

and for the reconstruction of a 3D model of the ground surface in near real time. However, at present, a part of the data is stored on board and another part is transferred to the ground station, where the image processing is carried out offline.



**Figure 3.** Picture of the UAV GPR system developed at the Deutsches Zentrum für Luft- und Raumfahrt (DLR), Germany.

The system [17], proposed by Wu et al. in 2019, was a UAV-borne GPR prototype based on a vector analyser equipped with a specially designed antenna. The vector analyser is the Planar R60 model by Copper Mountain Technologies, configured to work as stepped frequency continuous wave (SFCW) radar in the frequency range of 1 MHz - 6 GHz. It is equipped with a hybrid horn dipole antenna covering the typical GPR frequency range, i.e. 250–2800 MHz. The used UAV platform was the X8 model made of eight motors and four arms, with a maximum payload of 7 kg. The imaging capabilities of this system were assessed by retrieving the soil moisture map of the surveyed area.

In 2020, the research group of University of Maribor in Slovenia assembled a light UAV-based GPR system [18] (Figure 4) made up of a SFCW radar module operating in quasi-monostatic configuration and equipped with two hybrid Vivaldi-Horn antennas whose frequency range goes from 550 MHz up to 2.7 GHz and whose bandwidth is 2.15 GHz. The GPR total weight was about 780 g. The UAV drone platform was the DJI Matrice 600 Pro.

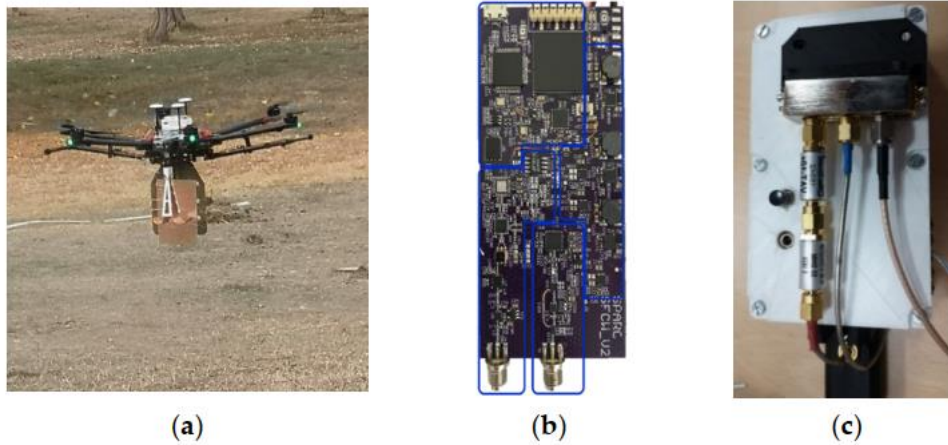


**Figure 4.** Picture of the UAV GPR system developed at University of Maribor, Maribor, Slovenia. (a) UAV platform; (b) transceiver module; (c) cable interconnections.

In [19] the COBRA Plug-in SE-150 monostatic antenna was mounted on the DJI Matrice 600 Pro platform also equipped with an automatic terrain-follow sensor, which estimates the sensor to ground distance with high precision (Figure 5). The radar module operates at 120 MHz with 240 MHz bandwidth. The radar system is able to explore the subsoil with a nominal vertical resolution up to 27 cm and a penetration depth up to 40 m in a medium with a relative dielectric permittivity equal to 5.



**Figure 5.** Picture of the UAV GPR System developed by the Dyrecta Lab., Conversano, Italy.

SPH Engineering Company developed a UAV GPR system [20], which is capable of exploiting three different commercial GPR sensors: Cobra Plug-In GPR [21] and Cobra CBD GPR [22] (both produced by Radarteam, Boden, Sweden), and the radar systems' Zond-12e (manufactured by Radar Systems Inc., Riga, Latvia) [23]. This system exploits two UAV platforms: DJI® Matrice M600 and M600pro. These platforms are able to fly for about 15 min with a payload of about 6 kg. Initially, this

system was equipped with a barometric altimeter, later removed since the accuracy provided by such altimeter was not enough to keep the drone at a constant distance from surface. Therefore, the system was up-graded with a more precise laser altimeter. Thanks to its multi-platform and multi-radar features, the system was used in various applicative contexts, such as for identifying archaeological site foundations, search and rescue missions, landmine detection, etc.

In 2021, the Department of Environment, Land, and Infrastructure Engineering of Polytechnic of Torino proposed a UAV GPR prototype [24] assembled by mounting the pulsed K2 IDS radar module on board a UAV platform based on the Venture VFF\_H01 model, with a size of about 80 cm (height)  $\times$  2 m (width). While the UAV platform is able to fly for about 15 min with a maximum payload of 7 Kg, the radar module is equipped with a 900 MHz antenna. The navigation control unit is composed by a barometric sensor, a laser rangefinder, gyroscopes, 3-axes accelerometers, and a GNSS receiver. This system was tested in the Alps region to assess its imaging capabilities for glacier monitoring and snow cover mapping.

Table 1 briefly summarizes the characteristics of the reviewed systems.

**Table 1.** UAV radar imaging systems.

<b>System</b>	<b>Radar Technology</b>	<b>Frequency Range</b>	<b>Antenna</b>	<b>Measurement Configurations</b>	<b>UAV Platform</b>
[7]	FMCW	Ka band	Linear array	MIMO	Small airplane
[8]	Pulsed Pulson P410	3.1-5.3 GHz	Helix	Bistatic (quasi-monostatic)	DJI Phantom 2
[9]	Software-defined radio	Carrier frequency: 2GHz (bandwidth not specified)	Antipodal Vivaldi antennas	Bistatic configuration with a 45° inclination	Hexacopter
[10]	Stepped frequency	1-4 GHz	Horn	Bistatic (quasi-monostatic)	DJI Matrice 600 Pro
[3]	M-Sequence UWB radar sensor	System bandwidth: 5.05 GHz (0.95-6 GHz)	1 TX custom designed spiral + 2 RX Vivaldi antennas	Two Vivaldi	‘Kraken’ octocopter

[11]	Pulsed Pulson P410	Frequency band: 3.1-5.1 GHz	Helix antennas	Quasi-monostatic	DJI Spreading Wings S1000+
[12]	M-sequence UWB radar	100 MHz-6 GHz	Two UWB Vivaldi antennas or two log-periodic antennas	Quasi-monostatic	DJI Spreading Wings S1000+
[14]	Pulsed Pulson P440	Frequency bandwidth: 3.1-4.8 GHz Carrier Frequency: 3.95 GHz	Two log-periodic PCB antennas (Ramsey LPY26)	Quasi-monostatic configuration: down-looking	Self-assembled DJI F550 hexacopter
[16]	FMCW	0.5-3 GHz	Vivaldi patch antennas	Bistatic (quasi monostatic)	DJI Matrice 600 Pro
[17]	SFCW Planar R60 VNA	Selected frequency step: 10 MHz Selected frequency bandwidth: 500-700 MHz	Hybrid horn-dipole antenna transmitting and receiving, combining a tapered TEM horn and a half-wave dipole	Monostatic stepped-frequency continuous wave (SFCW)	X8 model made of 8 motors and 4 arms (2 motors per arm) from RCTakeOff
[18]	SFCW	0.55-2.7 GHz	Hybrid Vivaldi-Horn antenna	Bistatic (quasi-monostatic)	DJI Matrice 600 Pro
[19]	Pulsed Cobra Plug-in GPR	0.5-260 MHz	COBRA Plug-in SE-150	Monostatic	DJI Matrice 600 Pro
[20]	Pulsed Cobra Plug-in GPR Cobra CBD Zond-12e	0.5-1000 MHz	COBRA Plug-in SE-70	Monostatic	DJI Matrice 600 DJI Matrice 600 Pro

			COBRA Plug-in SE- 150 COBRA CBD 200/400/800		
[24]	Pulsed K2 IDS radar	Carrier frequency: 900 MHz (bandwidth not specified)	Not specified	Monostatic	Venture VFF_H01

Contents of this section have been tackled in detail in [25], a review article analyzing the evolution over time of mini-UAV-based down-looking radar imaging systems and the relative challenges.

## 2.2 HARDWARE DESIGN

Based the review of the systems introduced in the previous Section, it is useful to extract a rough indication about the features of the hardware components used to assemble a typical UAV-borne radar imaging system, which results composed by three main parts: 1) the mini UAV platform; 2) the UAV Guidance, Navigation and Control (GNC) unit; 3) the radar payload.

As regard the mini UAV platform, preferred characteristics are high payload capability (1-6 Kg), good endurance (20 minutes at full load), high wind resistance, quick disassembly and easy transportation.

As regard the UAV GNC unit, redundancy is the sine qua non feature. The GNC unit requires the use of multiple inertial measurement units (i.e. gyroscopes and accelerometers), magnetometers, and at least a GNSS module (i.e. antenna and receiver).

About the radar payload, it consists of the radar unit, a GNSS module and a small CPU. The CPU guarantees for the storage and synchronization of radar and GNSS data. Synchronization is managed by assigning a CPU timestamp to each received radar and GNSS data package. It is worth pointing out that the GNSS module used for radar data georeferencing is not the one used for navigation. Indeed, it is a common choice to keep separate the radar payload from the GNC unit to facilitate the integration of the GNSS module with the other radar payload components and to ensure greater flight safety in case of anomalies.

Always about the radar payload, when the standalone GNSS receiver performance is not enough to guarantee the required positioning accuracy (which is typically at least smaller than half the radar signal wavelength), various solutions may be implemented. A first possibility consists in mounting on board the UAV a LIDAR altimeter, providing height information at a centimetre scale. LIDAR can be also integrated with the GNC units, thus allowing the accurate following of the terrain topography through the estimate of the distance between the sensor and the air-soil interface. In addition, accurate vertical and horizontal positioning information can be achieved through the exploitation of the CDGPS technique using two close GNSS receivers, one placed on-board the UAV, the other one placed in a ground station. The two GNSS receivers do not necessarily have to be in radio link with each other. Indeed, if the two GNSS receivers are left to acquire independently (but simultaneously), the

data can be processed offline; in this case, the CDPS technique is called Post Processing Kinematic (PPK). Instead, when the ground station is able to provide in real time the differential corrections to the on-board GNSS receiver, the CDGPS technique is called Real Time Kinematic (RTK). RTK information can be also integrated with the GNC units, thus allowing flying the drone more accurately.

Finally, according to the kind of scenario in which the UAV-based radar system is designed to fly, the kind of on-board sensors can change. In the case of areas with partially denied or degraded GNSS signal, multi-sensor strategies are worth of consideration for radar data georeferencing. These strategies allow combining the positioning information coming from the GNSS (when available, and with non-nominal level of accuracy), with the one coming from other kind of sensors, such as inertial navigation sensors. Kalman filtering [27] is one of the most known strategy for this kind of application. It is an estimation algorithm, rather than a filter, which uses knowledge of the deterministic and statistical properties of the system parameters and the measurements to obtain optimal estimates given the available information. For areas with fully denied GNSS signal many different positioning solutions have been proposed in literature, mostly in the world of indoor positioning [30,31]. In addition, other promising solutions are worth of investigation, such as ground-based vision systems [29] and wireless systems [28]. However, at the moment and at the best of my knowledge, there are not scientific papers addressing UAV radar imaging under degraded or absent GNSS signal conditions.

## **2.3 APPLICATIONS**

This Section provides an overview of the main applicative contexts wherein formerly described UAV GPR prototypes have been tested. The advantages and the practical issues connected to the use of UAV-based GPR technology in these contexts are discussed and a review about the main experimental results reported in the literature is presented.

### **2.3.1 Surface Object Detection**

Detection of small objects placed on the surface of the surveyed scenario is possible by means of UAV-based radar imaging systems. Systems [7] and [8] were both designed with this aim, but only [8] has been tested in a real scenario.

The system in [8] was flown over three different targets: a row of six trees, four vehicles in a parking lot, and two humans standing in a parking lot. During the first test, the system surveyed a row of six trees with different heights. The canopy of the tree was clearly visible in the collected radargram and the signal penetration throughout the canopy was observed. As for the second test, backscattering signals by four different parked vehicles were examined. Differently from the tree canopy, the soil scattering signals were masked by the reflections from the vehicles. The last test regarded two people standing in different postures. In this case, the ground returns were more visible compared to the previous test and the signal backscattered by the human subjects were clearly observable in the collected range profiles. All three tests demonstrated the capabilities of the radar prototype to detect the considered targets.

The system in [10] was also tested with surface targets by performing various experiments in down-looking, forward-looking, and circular configurations [32]. The first experiment was carried out by surveying an area containing two corner reflectors and several filled plastic cans. These simple experiments demonstrated the imaging capability of the system. Then, it was tested by flying over a meadow and a stone, and by performing the imaging of two targets into a vertical domain ( $x$ - $z$  plane). Recently, the system was upgraded with two additional antennas and some interesting experiments in interferometric configuration were conducted. The interferometric experiments aim to demonstrate the capabilities of the system to filter out the ambiguities induced by the topographic variations of the terrain and to accurately detect small metallic objects buried into the soil [33].

Experimental trials regarding the imaging of surface targets were also performed with System in [14]. A proof-of-concept measurement campaign was carried out by performing two flights over five surface targets. Since the radar frequency band was 3.1–5.1 GHz, targets were placed above the air–soil interface. The tomographic image referred to the first survey allowed the detection of only four targets, while the second survey showed all five targets, allowing a satisfactory estimation of the distances among them and their quota above the ground. More recently, the same UAV GPR system was exploited in [34] to perform two surveys at different altitudes over two corner reflectors placed at a relative distance of 10 m between each other. One corner reflector was covered with a cardboard box. The imaging problem was formulated by considering a horizontal investigation domain and the focused images of the surveyed scenario showed that no ambiguities occurred in the images when the targets were

illuminated at nadir. Conversely, false targets due to the left–right ambiguity appeared when the target was not illuminated at nadir. Further investigations were conducted with the same system by performing the imaging in the vertical plane [15]. The latter study aimed at comparing the imaging performance when using UAV positioning information provided by standalone GPS and CDGPS, respectively. As expected, CDGPS position data allowed for better imaging compared to standalone GPS data, an estimation of the relative distance between targets, as well as target elevation above the ground with higher accuracy.

### **2.3.2 Landmine Detection**

GPR deserves interest for landmine detection since it is able to detect both metal and plastic landmines [35]. Moreover, it can also work in contactless mode by exploiting ground vehicles and UAV technology. Different UAV-based GPR prototypes were deployed for landmine detection.

The system in [9] was the first prototype used for landmine detection purposes. In order to assess the detection performance of the SDR-based GPR technology, many experiments were carried out with different types of landmines. Specifically, three landmine prototypes were buried: (i) a bottle-made artefact (with 20% of metal component), (ii) a fully metallic artefact, and (iii) a tube-made artefact (with 30% of non-uniform metal component). The landmines were buried up to depths around 20 cm. In addition, two other types of metallic elements, acting as false landmines, were buried in the area. Fifteen surveys were performed in the presence of wet terrain (70% of humidity), which consequently made the full penetration of GPR signal difficult. The detection performances were assessed by calculating the Receiver-Operating Characteristic (ROC) curves. The results demonstrated that the UAV GPR system based on SDR technology could detect landmines made up of at least of 30% metal with a detection accuracy rate of 80%.

The system in [11] was tested for landmine detection applications. Early experimentations were conducted using a small and compact radar module, operating in the band 3.1–5.1 GHz [11]. Four experiments were carried out in different scenarios with different targets (metallic and dielectric). The main goal of the experimentation was to demonstrate the capability of the system to provide high-resolution underground images by exploiting high-accuracy trajectory information provided by

the on-board UAV positioning systems. Recently, the same system was upgraded with a different radar sensor operating in the frequency range of 100 MHz– 6 GHz in order to enhance the penetration capability [12]. Two flights in autonomous mode were also performed for testing innovative signal processing procedures. The tests showed improvements in terms of penetration as the system provided high-resolution 3D SAR images for a metallic disk with a 9 cm radius firstly placed in a small hole with an 8 cm depth without soil covering (first measurement), and then covered with soil (second measurement). Therefore, the achieved results demonstrated that the system can be very useful for landmine detection purposes.

The system in [16] was also developed for landmine detection but its first experimentations were carried out in non-operational scenarios. Indeed, the system was initially set up in an Inverse SAR (ISAR) measurement configuration. The targets were placed on a turntable and the radar module was placed at different distances ranging from 2.5 m to 4.5 m. The scope of this measurement setup was to emulate circular UAV flights at different heights. In a first experiment, a Bakelite anti-tank mine with a 30 cm diameter and a fragmentation anti-personnel mine with an 11 cm length were placed on the turntable, while the ground-based radar system was at a fixed position, making the motion compensation much easier. The radar images demonstrated that the identification of a mine type should be possible even in the low frequency band of 0.5–3 GHz.

The system in [18] was specially designed for landmine detection purposes. The first experiment was performed in labor-like scenario by mounting the sensor module on a motorized rail and burying an anti-personnel (AP) landmine of cylindrical shape, with a size of 8 cm × 14 cm into a polygon box with a depth of 20 cm. The scene was probed by moving the sensor with a constant velocity of about 0.6 m/s at a distance of 20 and 50 cm from the landmine. Then, a field measurement campaign was conducted in Skopje, North Macedonia. Two landmines were buried—the first one was the same AP landmine used in the laboratory test and was placed 20 cm deep into the soil, and the second one was a plastic anti-tank (AT) landmine of cylindrical shape with a size of 27 cm × 13 cm which had its top aligned to the ground surface. The UAV survey was carried out by moving the sensor backwards and forwards with a velocity of about 0.6 m/s at a height variable between 10 to 50 cm above the ground. The imaging results showed that both landmines were visible into the radargram, thus demonstrating the detection capabilities of the system.

### **2.3.3 Soil Moisture Mapping**

Monitoring soil moisture content is crucial for understanding hydrological processes, climate change, pollution assessment, and so on. GPR was proven a useful technology for soil moisture measurements due to its high-resolution and non-destructive properties [36]. UAV-borne GPR is a cost-effective solution that can cover wide and not easily accessible regions, significantly reducing measurement efforts. In addition, thanks to its contactless working mode, it would not impact with plants and ground during the growing phases. For this reason, the UAV GPR system is becoming a very attractive technological solution for this applicative context.

The system in [17] was the first UAV-based GPR prototype demonstrating the concept of soil moisture mapping. Specifically, a full waveform inversion method was proposed to link the soil moisture content with the soil permittivity through the surface reflections. In order to show this, three surveys were performed in different agricultural fields, placed in the loess belt region of Belgium and characterized with different soil moisture distributions. These fields were chosen since their soil moisture content was mainly controlled by local topography. The radar operative bandwidth was set in the range of 500–700 MHz to avoid the effects of surface roughness. The flights were carried out by manually driving the UAV at an altitude between 1 m and 5 m. The achieved results showed that the soil moisture maps were in agreement with the topographical maps of the fields and aerial photogrammetry observations, thus demonstrating the potential use of a UAV-based GPR system used for precision agriculture and environmental monitoring purposes.

### **2.3.4 Snowpack Stratigraphy and Search Rescue**

Stratigraphic information of the snowpack, such as depth, density, and layering, is crucial in snow resource management, which can affect public safety, hydropower production, and agriculture. Snowpack stratigraphy measurements are conducted by performing human surveys, and the density of measurements is typically obtained via samples collected through manually dug snow pits. These measurement methodologies are time-consuming and not always feasible, especially when large areas are mapped. GPR surveys are used in snowpack analysis to provide information on the density and depth of the snow. However, GPRs are conventionally deployed on the ground by moving the radar antenna in direct contact with the ground. GPR can be

mounted onto a snowmobile or manually moved for surveys over an undisturbed and flat snowpack. However, thanks to UAV platform flexibility, GPR prospecting also become possible in more challenging scenarios (e.g., rough avalanche debris).

The system in [3] was the first UAV-based GPR prototype developed for surveys of a layered snowpack over ground or sea ice. The system design was conceived with the aim of constructing a light and portable device with high resolution, which can detect prominent snow layers. Two measurement campaigns were performed: the first test was carried out by surveying a transect in wet snow along a road; the second was a slow overflight over a buried person and a metal plate placed at different depths. The goal of these two trials was to assess the system's capabilities in resolving snowpack stratigraphy and detecting a person and a target. In the first experiment, the system surveyed a road transect covered with snow by flying at an altitude of 50 cm. The recorded radargram clearly showed a high reflection about 40–50 cm below the radar antenna coming from the snow surface, while a significantly weaker reflection from the ground surface was visible at a depth of 160 cm. This last reflection was associated with a snowpack depth of 120 cm. Moreover, four clear reflections within the snowpack indicated the transition between different snow layers, thus mapping the snowpack stratigraphy as well as ice layers. In the second trial, the system was used with search and rescue purposes. Indeed, the test involved monitoring a snowy area, as well as hiding a buried person and metal plate at different depths. During the test, four surveys were performed over a human and a metal targets. The metal plate was present in all four passages, while the person was detected only in one flight. This last experiment demonstrated the penetration and imaging capabilities of the system and its potential for search and rescue missions.

The system in [24] was specifically designed for snow cover mapping. Two experimental tests were performed during the winter of 2020–2021 in Valle d'Aosta, Italy. The first experiment was conducted at the remote basin of Cheneil—an area of great importance for the valley since it hosts the main sources of water, while the second experiment was performed at Gressoney in a fenced zone close to a ski-resort area. During the first test, two ground-based GPR surveys were performed for assessing the imaging capabilities of the UAV-based GPR system. In particular, firstly, the ground-based data were calibrated by measuring the snow depth and exploiting a graduated rod. This allowed estimation of the average wave velocity by comparing the travel times of the GPR signals and the punctual snow depth measurements. Then, in

order to compare the ground-based data versus the air-based data, the range delay due to distance between the drone and air–snow interface was compensated from the UAV GPR radargram. Nevertheless, during the second test, the ground-based GPR data were not available. Therefore, to assess the drone-base dataset, the radar signals coming from the air–snow interface were compared with the range finder data. The good agreement between the ground-based and air-based radargram demonstrates the snow mapping capabilities of the UAV-based GPR prototype.



# Chapter 3: Radar Imaging from UAV

---

This Chapter deals with the main issues characterizing the UAV-based radar imaging. Section 3.1 deals with radar clutter and time domain strategies to overcome it. Section 3.2 deals with the need for accurate UAV positioning information and describes different possible techniques for the estimation of the UAV flight positions during the radar data acquisition. Section 3.3 proposes two different processing chains to obtain accurate and high resolution images of the scenario under test, while keeping acceptable the computing times and the computer resources in terms of memory space and processor velocity.

## 3.1 RADAR CLUTTER AND FILTERING OPERATIONS

Clutter is a relevant issue in UAV-based radar imaging applications. The term clutter is associated with all signal reflections occurring in the measurement time interval and interfering with targets echoes. One of the main clutter source is the direct coupling between the transmitting (TX) and receiving (RX) antennas, which is more significant when the antennas are very close to each other and a perfect isolation between them is not guaranteed. Indeed, part of the transmitted signal couples directly into the receiver without interacting with the targets. The direct coupling can be erased or at least reduced from the raw data by means of filtering procedures, such as background removal and/or time gating [36, 43, 42].

Background removal replaces each radar trace (A-scan) with the difference between it and the average value of all A-scans (or a subset of A-scans close to the trace of interest) in the radargram (B-scan). However, background removal also acts on the signal scattered by the target; thus, further ground compensation procedures are required to restore the point spread function (PSF) of the system [44].

Time gating selects the time interval containing the signals scattered from targets of interest and sets the signal outside such interval to zero.

The scattering from the air–soil interface is another challenging source of clutter for both superficial and sub-superficial UAV-based radar imaging applications. Indeed, the signal reflection coming from the air–soil interface might completely obscure the backscattering signal associated with small superficial or shallowly buried

targets, thus limiting the detection performance. Time gating is the simplest strategy used to mitigate the reflection from the air-soil interface. However, the selection of the optimal time window containing the signals from useful targets represents a critical issue. Indeed, when the targets are close to the air-soil interface, the time gating may also erase part of the useful signals. Background removal is another popular filtering approach used to remove the effect of the air-soil interface. Note that this procedure works under the assumption that the clutter is spatially constant along the measurement direction, i.e., the air-soil interface is flat. The gating and background removal strategies are the most popular signal processing strategies used for mitigating the surface clutter and have been exploited by the systems in [11, 12, 14, 18].

Another method for filtering surface clutter is based on the subspace projection [45, 46]. This procedure assumes that the clutter energy is stronger than the energy backscattered by the target and, accordingly, its contribution is associated with a larger singular value of the raw data matrix. Therefore, once the singular value decomposition (SVD) of the data matrix is computed, the gathered data are projected on the subspace defined by the singular vectors and associated with the singular values different from the largest ones. A key point of this method is the estimation of the clutter subspace dimension, which is often based on the visual inspection of the curve of the singular values. The subspace SVD de-noising procedure has been recently implemented in [14, 13].

Two further surface clutter mitigation strategies work with multi-antenna radar configurations. The first one was implemented in [7] by combining hardware and software solutions. Indeed, the system in [7] is characterized by a phased array antenna, which is able to narrow the antenna beam in the across-track direction, thus limiting the lateral surface returns. Then, in order to mitigate the residual clutter, a software solution based on a Doppler filtering procedure is also exploited. Indeed, all signal contributions coming from off-nadir directions and collected over multiple radar scans produce a Doppler shift in the signals. Upon exploiting a zero-Doppler filtering procedure, [7] is able to filter out the Doppler signals associated with off-nadir echoes, thus reducing the clutter disturbances. A second clutter mitigation procedure based on the multi-antenna concept was adopted by the system in [16]. This last is characterized by multi-static antennas mounted on a flexible boom. The antennas were distributed along  $z$  and  $x$  directions to allow three-dimensional imaging and a large variety of bi-static combinations, thus enabling clutter mitigation capabilities. Indeed, by

considering only one single radar image, due to the left–right ambiguity, it is not possible to estimate the depth of a target (see also [34]); however, by combining multiple radar images, i.e., those acquired at different look angles, the clutter contribution can be mitigated.

### 3.2 UAV POSITIONING

An accurate estimate of the UAV positions is needed in order to obtain well focused and well localized targets representations. The needed level of accuracy is typically set to be smaller than the half of radar working wavelength. Therefore, a first possibility for the estimation of the UAV position during the flight is given by the adoption of a standalone GNSS configuration. This is the simplest available solution and it consists into arranging a GNSS receiver (also equipped with its specific antenna) in addition to the one used by the drone for its navigation. Representative values of horizontal and vertical positioning errors, in case of satisfactory GPS visibility conditions, are, respectively, 3.5 m and 6.6 m [47]. Besides, when reasonably short time flights are considered, several error sources (i.e., broadcast clock, broadcast ephemeris, group delay, ionospheric delay and tropospheric delay) are strongly correlated both in space and time and may introduce positioning error, which results in a slow varying bias. In addition, the use of a proper processing strategy, such as carrier-smoothing [48], allows a reduction of the measurement noise [49], thus improving the GPS performance. Therefore, the first contribution of this PhD thesis has been demonstrating that satisfactory radar imaging performance is also possible by using standalone GPS when the meter-level positioning error exhibits small variations during the radar integration time [15]. This is possible because imaging degradation is associated with the drift of positioning errors during the radar integration time, while biases play a less significant role. This result can be of paramount importance when more sophisticated techniques cannot be used or cannot provide nominal performance levels. Results are presented in Chapter 6.

When the accuracy levels provided by standalone GNSS are not enough to guarantee satisfactory performance, other solutions occur. A first possibility consists in the use of a LIDAR altimeter [7, 9], which being put on-board the UAV allows retrieving drone height information at a centimetre scale. Typically, the altimeter is integrated with the navigation control units, which makes also possible to fly the UAV

at a constant distance from the air-soil interface, i.e. accurately following the terrain topography. When altimeter is not available, a backup solution consists into the adoption of Edge Detection algorithms [8, 14], which consist into estimating the UAV altitude variation directly from the radar data. Specifically, Edge detection is a post-processing procedure that allows evaluating the UAV height variations with accuracy proportional to the wavelength of the radar signal and in the assumption of flat topography.

Unfortunately, the adoption of both LIDAR altimeter and Edge Detection algorithms does not provide any information about the horizontal UAV displacements. Therefore, they are useful only for the UAV height estimate.

An enhanced technique allowing for the estimate of 3D UAV positions is the Carrier-phase Differential GPS (CDGPS) [48]. CDGPS implements the differences between the measurements collected by two relatively close GNSS receivers to filter out the common errors affecting them (i.e., satellite clock errors, tropospheric and ionospheric errors). In this regard, a typical configuration foresees at least one GNSS receiver placed on-board the UAV, and a second ground-based GNSS receiver. CDGPS data can be obtained both in real-time (Real-Time Kinematic - RTK) and in post-processing (Post-Processing Kinematic - PPK). Possibly, RTK technology can be integrated with the navigation control units in order to fly the UAV with centimetre accuracy along the desired trajectory (with CDGPS uncertainty of course) rather than estimating deviations from the ideal trajectory. Not requiring any communication link between the GNSS receivers, PPK results simpler and less expensive with respect to RTK, also allowing for longer distances between the two GNSS receivers. The RTK solution has been implemented in [10, 3, 11, 16, 18] whereas the PPK solution has been applied in [15, 50, 34]. Depending on the working environment, platform dynamics and receiver quality, two different types of CDGPS solutions can be obtained, i.e., fixed or float solutions [81]. The former is the most accurate one, being able to guarantee up to sub-cm accuracy in the determination of the relative position between the receivers, exploiting the property of carrier-phase ambiguities to become, under suitable measurement combinations and for properly designed receivers, integer numbers. The fixed solution can be robustly generated by processing multi-frequency GPS data and can be obtained, although with reduced time availability, by using single-frequency receivers, which typically rely on the float solution, i.e., they consider carrier-phase ambiguities as real numbers. Hence, single-frequency receivers can

robustly generate a realistic estimate of the carrier-phase ambiguities and the achieved accuracy degrades to the order of 10 cm. The error is reduced to a very few cm when fixed solutions are available. Within the framework of this thesis work, the PPK processing is carried out by using the open-source software RTKlib [72]. In particular, the post-processing analysis tool RTKPOST is used, which inputs RINEX observation data and navigation message files (from GPS, GLONASS, Galileo, QZSS, BeiDou and SBAS), and can compute the positioning solutions by various processing modes (such as Single-Point, DGPS/DGNSS, Kinematic, Static, PPP-Kinematic and PPP-Static). In this regard, the “Kinematic” positioning mode is chosen, which corresponds to PPK, with integer ambiguity resolution set to “Fix and hold”. RTKPOST outputs the E/N/U coordinates of the flying receiver with respect to the base-station, together with a flag relevant to the solution type (float/fixed). This flag, and the processing residuals, can be used as an estimate of the achieved positioning accuracy.

With the techniques seen so far it is possible to obtain an estimate of the trajectory followed by the drone during the measurements. However, another possibility is to fly the drone with high accuracy along predetermined trajectories, for examples straight lines at constant height. At this regard, it is worth mentioning the sophisticated algorithm developed in [9] to accurately control the platform trajectory during the data acquisition stage. Indeed, the system in [9] uses a very accurate UAV positioning control approach based on the backstepping method [51] and the desired angular acceleration function (DAF). The combined use of backstepping and DAF estimation methods allows exploitation of multiple sensor data (e.g., from IMU, GPS, and altimeter) to estimate the UAV flight dynamics in real time with high accuracy. As a result, the trajectory deviations can be limited to a few centimetres, thus allowing the collection of high-quality radar data.

A final observation concerns the UAV attitude, which must be kept constant during the flight in order to guarantee that TX and RX antennas are pointed at nadir (down-looking mode), i.e. at a zero incidence angle with respect to the normal to the air-soil interface.

### **3.3 RADAR DATA PROCESSING CHAINS**

This Section proposes two different radar data processing chains. While both the proposed strategies exploit time domain filtering procedures to reduce radar clutter and they process via a MWT approach the transformed into the frequency domain

radar data, they use UAV positioning information in different ways. Subsection 3.3.1 describes Strategy ‘A’, which is based on the Motion Compensation strategy and the Shift & Zoom Approach. Subsection 3.3.2 deals with Strategy ‘B’, which is based on the direct use of the CDGPS information into the implementation of the MWT approach. Strategy ‘A’ and Strategy ‘B’ can be regarded as general tools that can be applied to face different kind of radar imaging problems. Indeed, it is sufficient to change the adopted MWT approach according to the specific imaging problem to be solved.

**3.3.1 Motion Compensation with Shift and Zoom: Strategy ‘A’**

The radar data processing described in this subsection is shown in Figure 6 and will be referred to as strategy ‘A’. The strategy takes as input the raw radargram, which represents the radar signals collected at each measurement position (during the slow time and along the flight path) versus the fast time. The final output is a focused and easy interpretable image, referred to as tomographic image, which accounts for the reconstruction of the targets in the imaging plane, be it vertical or horizontal.

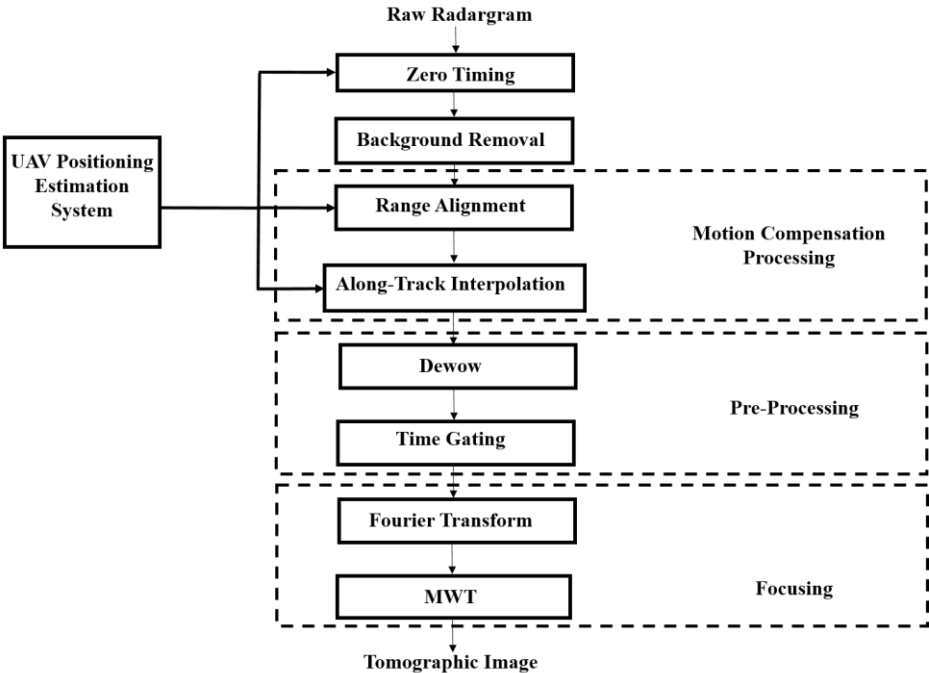


**Figure 6.** Radar data processing chain: strategy ‘A’.

Specifically, the first step of the proposed strategy consists into the zero-timing step. Zero-timing consists of setting the starting instant of the fast-time axis in such a way that the range of the signal reflected by the air–soil interface at the first

measurement point of the flight trajectory is coincident with the UAV flight height estimated by the positioning estimation system.

Then the Background Removal follows, which mitigates the undesired signal due to the electromagnetic coupling between transmitting and receiving radar antennas.

After, the Motion Compensation stage is performed and its main steps are depicted in Figure 6. Motion Compensation (MoCo) was first introduced in the framework of airborne SAR focusing [50], and the concept was later exploited for UAV-borne radar imaging in [3, 15]. The MoCo takes as input the UAV positions estimated by GPS or CDGPS (defined as “estimated” trajectory), it generates a straight flight trajectory (i.e., the along-track direction) and it modifies the radar signals by means of the range alignment and the along-track interpolation procedures. The range alignment compensates the altitude variations, occurred during the flight, by realigning each radar signal, along the nadir direction, with respect to a constant flight altitude. This latter is obtained from the UAV altitudes, as estimated by GPS or CDGPS and by performing an averaging operation; it is assumed as the altitude of the radar system in the following processing steps. The along-track interpolation accounts for the deviations occurring in the north–east plane between the estimated flight trajectory and a straight one. In details, a straight trajectory approximating the GPS or CDGPS estimated UAV flight trajectory in the north–east plane is computed by means of a fitting procedure. The straight trajectory in the north–east plane is taken as along-track direction, and is considered as the measurement line in the following processing steps. After the along-track direction is computed, the range aligned radar signals are interpolated and resampled in order to obtain evenly spaced radar data along the along track direction. Attitude variations are not considered in the MoCo. Indeed, the limited distance between the radar antennas and the UAV center of mass and the wide antenna radiation pattern imply that UAV attitude variation has a negligible effect on the data accuracy in terms of two travel time. Figure 7a shows a schematic representation of the MoCo. As indicated in Figure 7a,b, originally, the flight trajectory  $\Gamma$  has an arbitrary shape and each measurement points can be indicated by the following unevenly spaced vector:  $r_m = x_m\hat{x} + y_m\hat{y} + z_m\hat{z}$ . By applying the MoCo, the actual flight trajectory (and accordingly the collected data) is first modified by the range alignment operation as in Figure 7c and, then, by performing the along-track interpolation, the measurements points are evenly spaced, as shown in Figure 7d. Note

that for simplicity the imaging plane, i.e., the plane wherein the targets are supposed to be located, is here represented as a vertical plane defined by the along-track and the nadir directions, i.e.  $(x, z)$  coordinates, but nothing forbids to choose as imaging plane the horizontal one defined by  $(x, y)$  coordinates by adopting a horizontal imaging model.

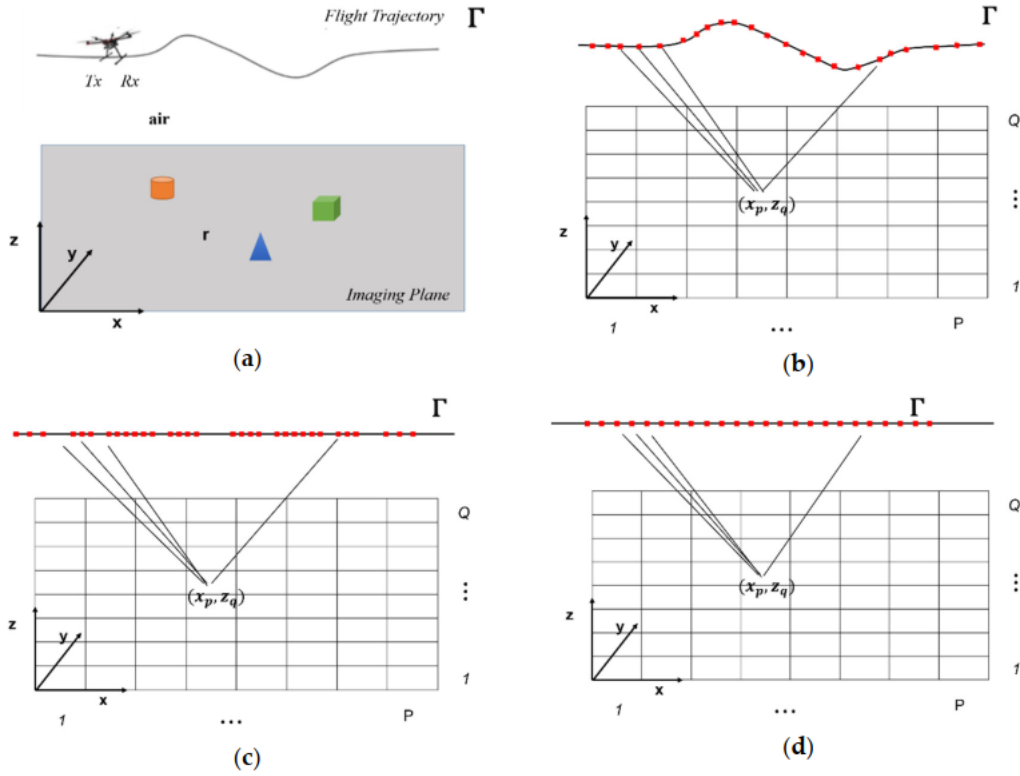


**Figure 7.** The Unmanned Aerial Vehicle (UAV)-borne radar imaging system, (a) actual imaging scenario; (b) starting schematic configuration; (c) schematic configuration after range alignment; (d) schematic configuration after along-track interpolation.

After MoCo, the radar data pre-processing step is performed (see Figure 6). At this step, time-domain radar preprocessing procedures as dewow and time gating are carried out.

The dewow step aims at mitigating the bias effect induced by internal electronic radar components by removing the average value of each radar trace [42].

The time gating procedure selects the interval (along the fast time) of the radargram, where signals scattered from targets of interest occur. This allows a reduction of environmental clutter and noise effects [36]. Herein, we define a suitable time window around the time where reflection of the air-soil interface occurs.

The last processing stage is the focusing. In this stage a focused image of the

scene under test, as appearing into the imaging domain, is obtained by solving an inverse scattering problem formulated into the frequency domain. Each trace of the radargram is transformed into the frequency domain by means of the Discrete Fourier Transform (DFT) so to provide the input data to the inversion approach. This latter faces the imaging as an inverse scattering problem by adopting one of the imaging models described in Chapter 5 and implementing an inversion scheme as the Truncated Singular Value Decomposition (TSVD) (Chapter 4, subsection 4.3.1) or the Adjoint of the Operator (Chapter 4, subsection 4.3.2).

Finally, the Shift and Zoom concept [52] has been implemented in order to speed up the computational time. Shift and Zoom is very useful when the TSVD is adopted since the TSVD inversion algorithm results in a computational intensive procedure when large (in terms of the probing wavelength) domains are investigated. Therefore, in the following the Shift and Zoom approach is described assuming that a TSVD has been adopted as inversion scheme.

The Shift and Zoom approach consists in processing data on partially overlapping intervals and combining the images in such a way to get an overall focused image. Shift and Zoom is only possible after the MoCo procedure has been applied, i.e. once radar data results as collected at a constant altitude and evenly spaced along a straight line.

Shift and Zoom is schematically represented in Figure 8 for the case of vertical imaging. The main steps may be explained as follows:

- The measurement acquisition line  $\Gamma$  and the survey area  $D$  are divided into  $V$  partially overlapping subdomains  $\Gamma_i$  and  $D_i$  with  $i = 1, 2, \dots, V$ ;
- For each subdomain  $D_i$ , the tomographic reconstruction  $\tilde{\chi}_i$  is obtained;
- The tomographic image of the overall surveyed area  $D$  can be obtained by combining the  $V$  reconstructions  $\tilde{\chi}_i$  achieved for each subdomain  $D_i$ .

A detailed description of the Shift and Zoom implementation is in [52].

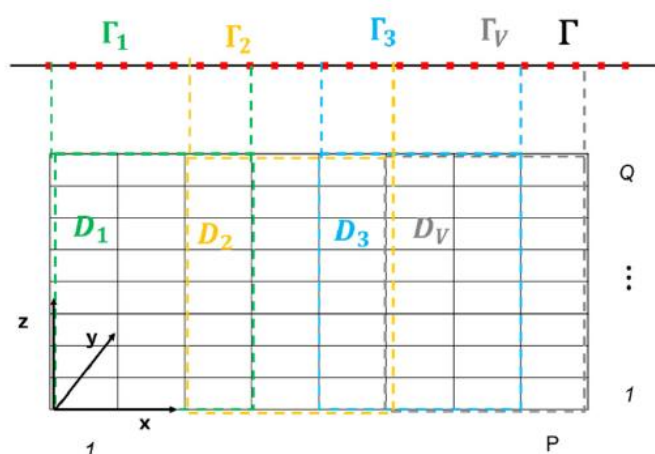


**Figure 8.** Shift and Zoom Algorithm Description for Vertical Imaging.

The use of the Shift & Zoom approach results as a not trivial improvement of the computational effectiveness because it avoids the computation of the scattering operator, and of its SVD, for each portion of dataset to be processed. Indeed, if MoCo is firstly applied, then the relative distance between the radar acquisition measurements and the pixel belonging to each subdomain are equivalent for all subdomain. In this way, the SVD calculation of the matrix  $\mathbf{L}$  that will be described in Chapter 4, have to be evaluated just in a single shot for the first subdomain, while the inversion for each subdomain mainly involves matrix times data vector multiplications.

By doing so, the computational time for the overall reconstruction process decreases drastically. In fact, the computational cost of the SVD operation for matrix  $\mathbf{L}$  having size  $K \times H$  is:

$$\sim O(K^{2H}) \quad (4.19)$$

Conversely, the adoption of the Shift and Zoom approach and the MoCo procedure reduces this cost to:

$$\sim O\left(\frac{K^\beta}{\alpha}\right) \quad (4.20)$$

where  $\alpha$  and  $\beta$  are the scaling factors related to reduced size of measurement line  $\Gamma_i$  and subdomain  $D_i$ , respectively. Therefore, an exponential reduction of the computational cost of the TSVD inversion scheme is obtained.

### 3.3.2 Direct use of CDGPS information into the focusing step: Strategy 'B'

Another possibility of processing radar data consists into the direct use of the 3D UAV positioning informations into the focusing step [34, 11, 53]. Figure 9 shows the developed processing chain that will be referred to as Strategy 'B'. After zero timing, background removal and time gating steps, radar data are transformed into the Frequency Domain through DFT. Then Microwave Tomography (MWT) accounting for relative distances between the UAV radar payload and the investigated scene is carried out. The exploitation of the positioning information directly in the MWT approach does not imply any treatment of the collected data and thus prevents from possible unaccuracy due to the alignment and resampling operations seen in MoCo. Therefore, it allows accurate images, as already pointed out in the airborne radar imaging context [61, 53]. In addition, Strategy 'B' is suitable for arbitrary flight geometries, i.e. not only for straight trajectories.

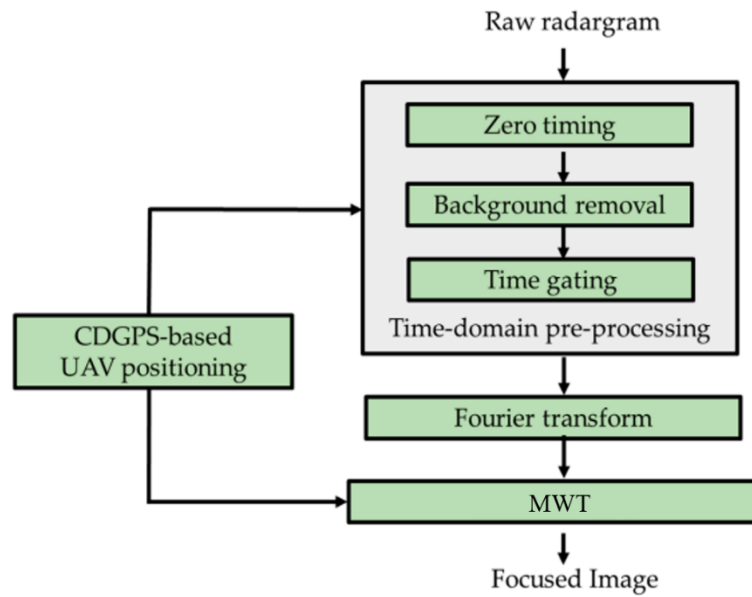


**Figure 9.** Direct use of GNSS positioning information into the MWT imaging step: Strategy 'B'.

# Chapter 4: Microwave Tomography: Fundamentals

---

This chapter deals with the basics of radar imaging, the integral formulation of the inverse scattering equations, the linear microwave tomographic approaches and the figures of merit for the resolution analysis. Therefore, this chapter defines the mathematical tools needed in the MWT approaches that have been designed in the context of this thesis and which are based on the scattering models that will be described in Chapter 5. Specifically, all the developed approaches are formally formulated as the solution of the linear integral equation (4.6) given in section 4.3. The solution of this equation is faced by using the inversion scheme described in sub-section 4.3.1 or, alternatively, that presented in sub-section 4.3.2. On the other hand, the actual expression of the integral equation (4.6) depend on the scattering model describing the signal propagation and, as said, those accounted for in this thesis are presented in Chapter 5.

Chapter 4 is structured as follows. Section 4.1 introduces the basics of radar imaging. Section 4.2 describes the integral formulation of the scattering equations. Section 4.3 deals with the linear MWT, which is based on Born approximation. Section 4.4 introduces the figures of merit for resolution analysis, i.e. the Spectral Content (SPEC) and the Point Spread Function (PSF).

## 4.1 BASICS OF RADAR IMAGING

A Radar (Radio Detection and Ranging) is an active sensor that uses beamed and reflected radio waves to determine the distance (ranging) of the target objects in the beam path, and sometimes their relative angle and radial velocity. The range measure,  $R$ , of a specific object in the beam path is possible by measuring the time of flight  $T_{of}$  of the transmitted signal, i.e. the time difference between the instant of transmission of the energy  $t_{TX}$  and the instant of reception of the backscattered energy  $t_{RX}$ :

$$T_{of} = t_{RX} - t_{TX} \quad (4.1)$$

$$R = \frac{T_{of} c_0}{2\sqrt{\epsilon_r}} \quad (4.2)$$

where  $c_0$  is the speed of the light in vacuum and  $\epsilon_r$  is the relative permittivity, which is a dimensionless parameter varying in the range 1-80 for common materials [42].

In order to use a radar to perform imaging, it is necessary to observe the scene under different angles of view, i.e. by moving the radar along a desired trajectory and by collecting the backscattered electromagnetic signals in different measurement points.

Let us consider a time-domain radar, i.e. the radar transmits a pulse signal and, for each pulse, it measures the amplitude of the backscattered electromagnetic field as a real function of the time (Figure 10a). This time is often referred to as “fast time”, meaning the time of propagation of the signal. Conversely, the term “slow time” is used to refer to the time that the radar employs to cover a certain measurement line and collect the data. With these specifications, we refer as A-scan the single received waveform (Figure 10a), and as B-scan or radargram (Figure 10b) the ensemble of all the received A-scans. Of course, as a real function, each A-scan has positive and negative values (Figure 10a). In the light of this, the pixels intensity values displayed in a radargram correspond to the amplitude of the component of the backscattered electromagnetic field as measured by the radar sensor, while the vertical and horizontal axes correspond to the fast time and slow time respectively.

If the radar works in the frequency domain, modulus and phase of the backscattered field are measured into a certain frequency range. Theoretically, by means of the Inverse Fourier Transform (IFT), frequency domain data can be transformed in the time domain. However, in the passage from frequency to time domain, the obtained time-domain data result as complex functions of the fast time, therefore only the real part of the data must be considered to build the A-scan and the B-scan.

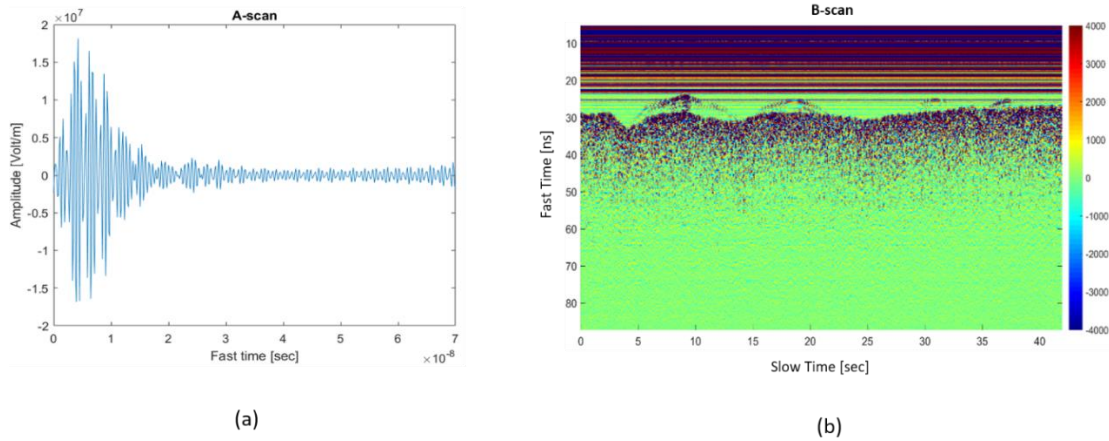


**Figure 10.** (a) A-scan. (b) B-scan (i.e. radargram).

The peculiarity of a radargram is that point-like target appears as a diffraction hyperbola rather than as a point (see Figure 10b). Therefore, the term radar imaging refers to those signal processing techniques that starting from the raw radargram aim at simplifying its interpretation by obtaining a so called focused radar image, which is an image where the scattering objects appear as bright blobs over a darker background, rather than a diffraction hyperbola (see Figure 11). Commonly, the imaging process (also known as focusing stage) is performed after the application of time or frequency-domain operations aiming at reducing noise and clutter and more in general at improving the signal components referred to the backscattered field given by the targets of interest. These time and frequency domain operations have been already described in Chapter 3.

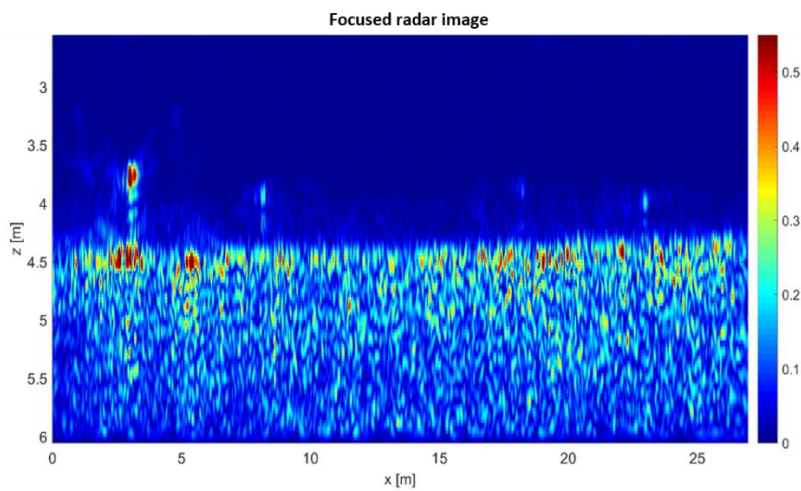


**Figure 11.** Focused radar image.

There are many types of radar imaging techniques, as migration, beamforming, matched filtering, back projection, microwaves tomography. All these techniques have as common goal the reconstruction of morphology features (location, shape, and size) of the targets in the observed scene, starting from the knowledge of the electromagnetic field backscattered by the targets when illuminated by a known incident field. Unfortunately, these techniques do not allow a quantitative reconstruction, i.e. retrieving the electromagnetic properties (dielectric permittivity and electrical conductivity) of the targets, because they assume model approximations in the formulation of the scattering, which is the physical phenomenon underlying the radar imaging.

This thesis exploits microwave tomography (MWT) to address the focusing stage, therefore radar imaging is faced as an inverse scattering problem whose unknown is the contrast function defined as:

$$\chi = \frac{\epsilon_t}{\epsilon_s} - 1 \quad (4.3)$$

with  $\epsilon_t$  being the dielectric permittivity of the target and  $\epsilon_s$  the dielectric permittivity of the soil. If the use of Born approximation allows to express the data-unknown relation through a linear expression, on the other hand, this approximation provides an inaccurate model of the scattering phenomenon, which prevents obtaining quantitative reconstructions.

## 4.2 INTEGRAL FORMULATION OF THE SCATTERING EQUATIONS

Let us start by considering the 3D scenario of Figure 12 where an elementary source placed in  $\mathbf{r}_m$  radiates an electromagnetic field in the domain containing two objects, in the following referred to as targets. These latter have  $\mathbf{r}$  and  $\mathbf{r}'$  positions respectively. Also,  $\mathbf{r}_m$  represents the measurement point in which the electromagnetic field backscattered by the target want to be measured. In this thesis the scattering problem is treat as a 2D problem, hence the vertical imaging plane and the horizontal imaging plane are also represented in blue and grey, respectively, as the two imaging domains in which the targets want to be focused.

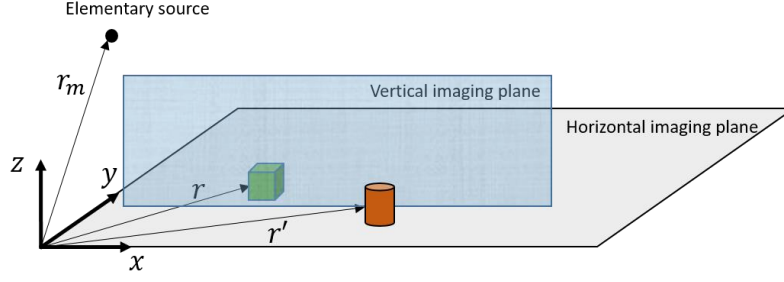


**Figure 12.** Radar imaging scenario.

The radar imaging approach is based on the following assumptions:

- i) non-magnetic, dielectric isotropic materials;
- ii) elementary source with a broad radiation pattern;
- iii) 2D model.

With these assumptions, the following coupled integral equations govern the remote sensing process:

$$E_s(\mathbf{r}_m, \omega) = k_0^2 \iint_D g_e(\mathbf{r}_m, \mathbf{r}, \omega) E_t(\mathbf{r}, \omega) \chi(\mathbf{r}) d\mathbf{r} \quad (4.4)$$

$$E_t(\mathbf{r}, \omega) = E_i(\mathbf{r}, \omega) + k_0^2 \iint_D g_i(\mathbf{r}, \mathbf{r}', \omega) E_t(\mathbf{r}', \omega) \chi(\mathbf{r}') d\mathbf{r}' \quad (4.5)$$

where  $k_0$  is the wavenumber in free space and  $\omega$  is the angular frequency taking value in the frequency range  $\Omega$ . In the former equations,  $E_s$  is the field scattered by the targets, and  $E_t$  is the total electric field in the domain  $D$ , which is equal to the sum of the incident field  $E_i$  and an integral accounting for the mutual interactions among targets in  $D$ . Moreover,  $g_e$  and  $g_i$  are the external and internal Green's functions, respectively, which are defined according to the reference scenario at hand, i.e. homogeneous medium, half space, layered medium and so on [37]. The external Green's function  $g_e$  expresses the field radiated at  $\mathbf{r}_m$  by an elementary source placed at  $\mathbf{r}$ . The internal Green's function  $g_i$  accounts for the field produced at  $\mathbf{r}$  by an elementary source placed at  $\mathbf{r}'$ .

It is worth noting that equations (4.4) and (4.5) provide a unified frame suitable to account for different scenarios and measurement configurations provided that the proper expressions for the incident field and the Green's functions are inserted in them. These quantities, indeed, depend on the measurement configuration as well as on the characteristic features of the considered reference scenario [37].

The inversion of (4.4) and (4.5), i.e., the determination of the contrast function  $\chi$  from  $E_s$ , implies notable mathematical difficulties. Indeed, the problem is nonlinear [38] because  $E_s$  is linearly related to the product of  $E_t$  and  $\chi$  [see (4.4)], but  $E_t$  depends on  $\chi$  through (4.5). The most important consequence of the nonlinearity is the occurrence of false solutions (local minima) while applying local optimization procedures to minimize a cost function [39], [40]. On the other hand, global optimization procedures, which are known to avoid the local minima problem, imply a notable computational effort, which makes it not suitable to contactless radar surveys where large investigation domains are considered, and thus a large number of unknown parameters must be reconstructed.

Furthermore, currently there is a huge attention towards the use of Artificial Intelligence (AI) but its use in radar imaging is still an open issue and it is neglected in this thesis.

### 4.3 LINEAR MWT

A notable simplification in the inverse problem is attained by linearizing the scattering equations thanks to the adoption of the Born approximation [37], which neglects the mutual interactions in  $D$  [integral in (4.5)] or equivalently approximate the total field  $E_t$  as the incident field  $E_i$ . From a physical point of view, this approximation assumes that the presence of the targets does not introduce a significant perturbation on the field radiated by the primary sources. As a result, the data-unknown relationship is given by the linear integral equation:

$$E_s(\mathbf{r}_m, \omega) = k_0^2 \iint_D g_e(\mathbf{r}_m, \mathbf{r}, \omega) E_i(\mathbf{r}, \omega) \chi(\mathbf{r}) d\mathbf{r} = L[\chi] \quad (4.6)$$

where  $L: \mathcal{L}^2(D) \rightarrow \mathcal{L}^2(\Gamma \times \Omega)$  is a linear projection operator mapping the unknown space into data space, which is a square-integrable function space.

By exploiting the Method of Moments, we get the discretized formulation of (4.6):

$$\mathbf{E}_s = \mathbf{L}\chi \quad (4.7)$$

In (4.7)  $\mathbf{E}_s$  is the  $K = M \times N$  dimensional data vector, with  $M$  being the total number of radar scans and  $N$  the number of operative pulsations  $\omega_n$ ,  $n = 1, 2, \dots, N$ .  $\mathbf{L}$  is the  $K \times H$  scattering matrix related to the linear operator that maps the space of the unknown vector  $\boldsymbol{\chi}$  into the space of data (measured scattered field)  $\mathbf{E}_s$ . Note that  $H = P \times Q$  denotes the number of pixels  $(x_p, z_q)$  discretizing the domain  $D$ , where  $p = 1, 2, \dots$ , and  $q = 1, 2, \dots, Q$ .  $\boldsymbol{\chi}$  is the  $H$  dimensional unknown vector.

The linear inverse problem stated by (4.6) and (4.7) is ill-posed. An inverse scattering problem is defined ill-posed when at least one of the three Hadamard's conditions [41] is violated: existence of the solution; uniqueness of the solution; continuity of the solution as the initial conditions vary. Since the  $L$  operator in (4.6) is compact, it does not have a continuous inverse, therefore the third Hadamard's condition is not verified. As a result, the presence of noise on the data makes the inversion process unstable, and it is necessary to apply regularization schemes to obtain a solution with a physical meaning. Different regularization strategies can be applied, as the truncated singular value decomposition (TSVD) or the Adjoint of the operator  $L$  (also known as back-projection). In both the strategies, the solution can be expressed as a function of the singular values obtained from the Singular Values Decomposition (SVD) of the matrix  $\mathbf{L}$ .

The SVD is a factorization of a real or complex matrix. It generalizes the eigendecomposition of a square normal matrix with an orthonormal eigenbasis to any  $m \times n$  matrix. It is related to the polar decomposition. Specifically, the singular value decomposition of an  $m \times n$  complex matrix  $\mathbf{M}$  is a factorization of the form  $\mathbf{M} = \mathbf{U}\boldsymbol{\Sigma}\mathbf{V}^*$  where  $\mathbf{U}$  is an  $m \times m$  complex unitary matrix,  $\boldsymbol{\Sigma}$  is an  $m \times n$  rectangular diagonal matrix with non-negative real numbers on the diagonal,  $\mathbf{V}$  is an  $n \times n$  complex unitary matrix, and  $\mathbf{V}^*$  is the conjugate transpose of  $\mathbf{V}$ . If  $\mathbf{M}$  is real, then  $\mathbf{U}$  and  $\mathbf{V}$  can be guaranteed to be real orthogonal matrices; in such contexts, the SVD is often denoted  $\mathbf{U}\boldsymbol{\Sigma}\mathbf{V}^T$ . The diagonal entries  $\sigma_i = \Sigma_{ii}$  of  $\boldsymbol{\Sigma}$  are uniquely determined by  $\mathbf{M}$  and are known as the singular values of  $\mathbf{M}$ . The number of non-zero singular values is equal to the rank of  $\mathbf{M}$ . The columns of  $\mathbf{U}$  and the columns of  $\mathbf{V}$  are called left-singular vectors and right-singular vectors of  $\mathbf{M}$ , respectively. They form two sets of orthonormal bases  $\mathbf{u}_1, \dots, \mathbf{u}_m$  and  $\mathbf{v}_1, \dots, \mathbf{v}_n$ , and if they are sorted so that the singular values  $\sigma_i$  with value zero are all in the highest-numbered columns (or rows), the

singular value decomposition can be written as  $M = \sum_{i=1}^r \sigma_i \mathbf{u}_i \mathbf{v}_i^*$  where  $r \leq \min\{m, n\}$  is the rank of  $M$ .

The SVD is not unique. It is always possible to choose the decomposition so that the singular values  $\Sigma_{ii}$  are in descending order. In this case,  $\Sigma$  (but not  $U$  and  $V$ ) is uniquely determined by  $M$ . The term sometimes refers to the compact SVD, a similar decomposition  $M = U\Sigma V^*$  in which  $\Sigma$  is square diagonal of size  $r \times r$ , where  $r \leq \min\{m, n\}$  is the rank of  $M$ , and has only the non-zero singular values. In this variant,  $U$  is an  $m \times r$  semi-unitary matrix and  $V$  is an  $n \times r$  semi-unitary matrix, such that  $U^*U = V^*V = I_r$ . Mathematical applications of the SVD include computing the pseudoinverse, matrix approximation, and determining the rank, range, and null space of a matrix. The SVD is also extremely useful in all areas of science, engineering, and statistics, such as signal processing, least squares fitting of data, and process control.

#### 4.3.1 Inversion based on the TSVD

It is a regularization scheme allowing a stable and robust solution with respect to noise on data [41], which provides the following expression for the contrast function:

$$\tilde{\chi} = \sum_{n=1}^T \frac{\langle E_s, u_n \rangle v_n}{\sigma_n} \quad (4.8)$$

where  $T$  is the truncation threshold,  $\sigma_n$  is the set of singular values of matrix  $L$  ordered in a decreasing way,  $u_n$  is the set of the left singular vector,  $v_n$  is the set of the right singular vector and  $\langle E_s, u_n \rangle$  is the scalar product in data space. The threshold  $T \leq K$  defines the “degree of regularization” of the solution and is chosen as a trade-off between accuracy and resolution requirements from one side, and solution stability from the other side. Indeed, if from one hand the accuracy and resolutions requirements would need the highest value of the threshold  $T$ , on the other hand the solution stability would need the smallest  $T$  value.

The modulus of the regularized contrast function  $\tilde{\chi}$  in (4.8) normalized to its maximum value in the scene defines a spatial map, referred to as a tomographic image (Figure 11). Hence, the regions of  $D$  where the modulus of  $\tilde{\chi}$  are significantly different from zero indicate the position and approximate geometry of the targets.

### 4.3.2 Inversion based on the Adjoint of the Operator

The radar imaging can be faced as the inversion of the linear integral Equation (4.7). This is done by computing the adjoint of the forward scattering operator  $L$ :

$$\tilde{\chi} = L^+ E_s \quad (4.9)$$

where  $L^+$  denotes the Adjoint of  $L$ .

Then SVD can be used to write the expression of the scattered field and the estimate of the contrast function:

$$E_s = \sum_{n=1}^K \langle E_s, u_n \rangle u_n \quad (4.10)$$

$$\tilde{\chi} = L^+[E_s] = \sum_{n=1}^K \sigma_n \langle E_s, u_n \rangle v_n \quad (4.11)$$

Thanks to the two assumptions of targets in far field region with respect to the elementary source and time dependence of kind  $e^{j\omega t}$ , which is dropped for notation simplicity, (4.6) can be rewritten as:

$$E_s(\mathbf{r}_m, \omega) = I(\omega) \iint_D \frac{e^{-j2k_0|\mathbf{r}_m-\mathbf{r}|}}{|\mathbf{r}_m-\mathbf{r}|^2} \chi(\mathbf{r}) d\mathbf{r} \quad (4.12)$$

where  $k_0 = \frac{\omega}{c}$  is the propagation constant in free space,  $I(\omega)$  is the spectrum of the transmitted pulse (we assume  $I(\omega) = 1$  within the system bandwidth),  $\chi$  is the reflectivity function (unknown) at  $\mathbf{r}$  in  $D$ , and  $E_s$  is the electric scattered signal at  $\mathbf{r}_m$ .

In this way, (4.9) becomes:

$$\tilde{\chi} = L^+ E_s = \int_{\Gamma} \int_{\Omega} E_s(\mathbf{r}_m, \omega) \frac{e^{j2k_0|\mathbf{r}_m-\mathbf{r}|}}{|\mathbf{r}_m-\mathbf{r}|^2} d\mathbf{r}_m d\omega \quad (4.13)$$

The adjoint inversion scheme given by this equation is also referred as frequency-domain back-projection, since the measured signal is back projected to the point where it is generated and the image is formed as the coherent summation of these contributions.

#### 4.4 FIGURES OF MERIT FOR RESOLUTION ANALYSIS

The term resolution analysis refers to the investigation of how the reconstruction capabilities of the adopted radar imaging approach are affected by the parameters of the implemented measurement configuration. It is typically carried out through the study of two different functions, i.e. the Spectral Content (SPEC) of the object space and the Point Spread Function (PSF).

SPEC [41] is defined as the sum of the modulus of the Fourier transform of the singular functions  $v_n$  corresponding to the singular values that are above the (fixed) TSVD threshold  $T$ :

$$SPEC(\eta, \zeta) = \sum_{n=1}^T |\widehat{v}_n(\eta, \zeta)| \quad (4.14)$$

$\eta$  and  $\zeta$  being the spectral variables and

$$\widehat{v}_n(\eta, \zeta) = \iint_{\mathcal{D}} v_n(x, z) e^{-j(\eta x + \zeta z)} dx dz \quad (4.15)$$

In (4.15)  $v_n$  denote the left singular vectors and form an orthonormal basis for the object space, i.e., the set of visible objects that could be retrieved from a subset of noiseless data. SPEC provides a global indication on the spatial frequencies that can hopefully be retrieved by using the TSVD and immediately gives a picture of the filtering effects introduced by the regularized inversion of the matrix  $L$ . Therefore, the spectral content is a general tool to appreciate the reconstruction capabilities of a linear inverse scattering algorithm. According to the kind of scenario in which the system is left to acquire, there will be different ways to model the operator, and therefore the SPEC will assume different shapes.

PSF is defined as the reconstruction of a point-like target [41] and it can assume different expressions according to the inversion strategy. In [54] the regularized PSF referred to the TSVD scheme and the one attained by adjoint inversion are considered and compared. Specifically, for an impulsive target with unitary contrast located at point  $\mathbf{r}_0 \in \mathcal{D}$ , the regularized PSF referred to the TSVD scheme is given by

$$PSF^{TSVD}(\mathbf{r}, \mathbf{r}_0) = \sum_{n=1}^{N_t} v_n^*(\mathbf{r}_0) v_n(\mathbf{r}) \quad (4.16)$$

while the one attained by adjoint inversion reads as

$$PSF^{adj}(\mathbf{r}, \mathbf{r}_0) = \sum_{n=1}^{\infty} \sigma_n^2 v_n^*(\mathbf{r}_0) v_n(\mathbf{r}) \quad (4.17)$$

where \* stands for the conjugation operation.

By comparing (4.16) and (4.17), one can observe that both PSFs are expressed as a weighted sum of basis functions  $v_n$  involving diverse coefficients. Specifically, the coefficients are  $v_n^*(\mathbf{r}_0)$  in the TSVD scheme, while they are  $\sigma_n^2 v_n^*(\mathbf{r}_0)$  in adjoint inversion. Therefore, in this latter scheme, the amplitude of the coefficients progressively decays according to the square of singular values  $\sigma_n$ .

Chapter 6 proposes the resolution analysis based on equation (4.17) for a high frequency radar system by UAV. Since the imaging plane is supposed horizontal, the formulas of the resolutions limits holding for an imaging in the horizontal plane from an ideal rectilinear flight path are considered for a qualitative comparison. The left-right ambiguity and the inability to provide high-resolution 3D target reconstructions are also faced.

# Chapter 5: UAV-based Radar Imaging via MWT

---

UAV-based radar imaging refers to all those processing techniques aiming at improving the interpretability of radar data acquired by using an UAV as moving platform and it can be carried out with different purposes, as investigating superficial areas or sub-superficial regions. This chapter describes the scattering models adopted to define the MWT approaches developed during the PhD research activities. These models account for the specific radar imaging problem (vertical or horizontal) to be solved as well as the particular scenario of interest (superficial or sub-superficial). Moreover, all the models describe the scattering under the 2D scalar assumption, i.e. they regard the contrast  $\chi$  as a function of  $(x, z)$  and  $(x, y)$  spatial coordinates, respectively. In addition, the chapter proposes a strategy to obtain a pseudo-3D reconstruction of the scenario under test from data gathered along multiple lines, i.e. by planning a flight grid.

The chapter is organized as follow. Sections 5.1 and 5.2 describe the scattering models adopted to formulate the superficial and the sub-superficial radar imaging in the vertical plane defined by the measurement line and the radar antennas pointing direction, respectively. Section 5.3 tackles the case of data collected along multiple measurement lines and describes the Multiline Imaging Approach (MIA) for obtaining a pseudo-3D reconstruction of the investigated scene. Section 5.4 describes the scattering model adopted to design the MWT approach facing the horizontal imaging in a free-space scenario.

## 5.1 VERTICAL IMAGING MODEL FOR FREE-SPACE PROPAGATION

Let us refer to the 3D scenario sketched in Figure 13. The ultra-wideband radar transceiver on board the UAV illuminates the scene with transmitting and receiving antennas pointed at nadir (down-looking mode), i.e. at a zero incidence angle with respect to the normal to the air-soil interface. The radar can be considered operating in monostatic mode since the transmitting and receiving antennas have negligible offset in terms of the probing wavelength. At each measurement point along the flight

trajectory  $\Gamma$ , the transceiver records the signals scattered from the targets over the angular frequency range  $\Omega = [\omega_{min}, \omega_{max}]$ . Therefore, multimonostatic and multifrequency data are collected. The radar imaging approach is based on the following assumptions:

- i) 2D vertical investigation domain  $D$ ;
- ii) non-magnetic, dielectric objects;
- iii) objects with infinite extension along the cross track direction (i.e.  $y$  direction);
- iv) antennas with a broad radiation pattern which are modelled as elementary source, i.e. infinite line current;
- v) targets in far field region with respect to radar antennas;
- vi) linear model of the scattering phenomenon (Born approximation);
- vii) time dependence  $e^{j\omega t}$ , where  $\omega = 2\pi f$  and  $f$  is the frequency, is dropped for notation simplicity.

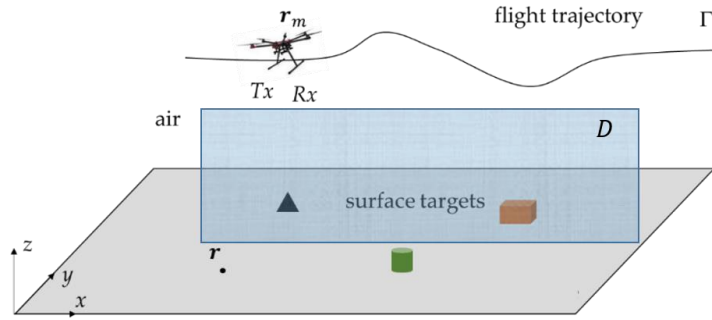


**Figure 13.** UAV-based radar imaging. Vertical imaging for superficial scenario.

Under these assumptions, the imaging is faced as the solution of the inverse scattering problem described by the following equations:

$$E_s(x_m, h, \omega) = \frac{-k_0^2 \eta_0 I}{2\pi} \iint_D \frac{e^{-j2k_0 R}}{R} \chi(x, z) dx dz. \quad (5.1)$$

Note that equation (5.1) is obtained by taking into account the asymptotic expression of the Green's function. Specifically, in the case of 2D Transverse magnetic model the external Green's function is expressed as [55]:

$$g_e(x_m, h, x, z, \omega) = \frac{j}{4} H_0^{(2)}(k_0 R) \quad (5.2)$$

where  $H_0^{(2)}$  is the Hankel's function of the second kind and zero order,  $R = \sqrt{(x - x_m)^2 + (z + h)^2}$  is the distance between the measurement point  $\mathbf{r}_m(x_m, h)$  and the generic point  $\mathbf{r}(x, z)$  in  $D$ , and  $k_0 = \omega/c_0$  (where  $c_0 = 3 \times 10^8$  m/s is the speed of light in free space). By exploiting the asymptotic approximation of Hankel's function, (5.2) is rewritten as

$$g_e(x_m, h, x, z, \omega) \approx \frac{1}{2\sqrt{2\pi k_0}} e^{\frac{j3\pi}{4}} \frac{e^{-jk_0 R}}{\sqrt{R}} \quad (5.3)$$

Moreover, we take into account that the primary source is modelled as infinite line current with unitary amplitude and that the incident field is given as

$$E_i(x, z, x_m, h, \omega) = -j\omega\mu_0 I g_e(x_m, h, x, z, \omega) \quad (5.4)$$

where  $I$  is the electric current amplitude and  $\mu_0 = 4\pi \times 10^{-7}$  H/m is the free-space magnetic permeability. In this way, equation (5.1) is obtained.

The discretized formulation of the imaging problem described in Equation (5.1) is obtained by exploiting the Method of Moments and the TSVD approach as described in Chapter 4.

Note that the free-space propagation (FP) model herein described is often used to face the sub-surface imaging when the antenna height is much greater than the depth of the targets, i.e.  $h \gg d$ , the propagation in the soil can be considered negligible. This approximation has been adopted in various papers regarding the airborne GPR imaging problem, where shallow targets had to be identified by a radar flying at high altitude [53].

## 5.2 VERTICAL IMAGING MODELS FOR SUB-SUPERFICIAL PROPAGATION

Let us refer to the 2D reference scenario in Figure 14. The scenario features a two-layered medium where the upper half space ( $z < 0$ ) is air while the lower half space ( $z > 0$ ) is soil. The soil medium is assumed homogeneous, lossless, nonmagnetic, and characterized by the dielectric permittivity  $\epsilon_s$ . The domain  $D$  is the vertical spatial region where the targets are located, and  $\epsilon_t$  is the unknown target dielectric permittivity. As in the previous section, the scene is investigated by a couple of TX and RX antennas operating in monostatic mode. The antennas are located at a constant

height  $h$  above a flat air-soil interface and move along the rectilinear trajectory  $\Gamma$ . The antennas are modeled as electric line sources polarized along the  $y$ -axis (transverse magnetic polarization) and work in the angular frequency interval  $\Omega = [\omega_{min}, \omega_{max}]$ . The  $\exp(j\omega t)$  time dependence is assumed and dropped. The measurement position is denoted by  $\mathbf{r}_m(x_m, -h)$  and  $\mathbf{r}(x, z)$  is a point in the investigation domain  $D$ . The presence of the targets is described by the contrast function  $\chi = \varepsilon_t/\varepsilon_s - 1$ . In the following, three different models that calculate  $g_e$  and  $E_i$  by taking into account wave reflection/transmission at the air-soil interface are analysed. These models have been also described in the review article [56] that represents another significant contribution of this PhD thesis.

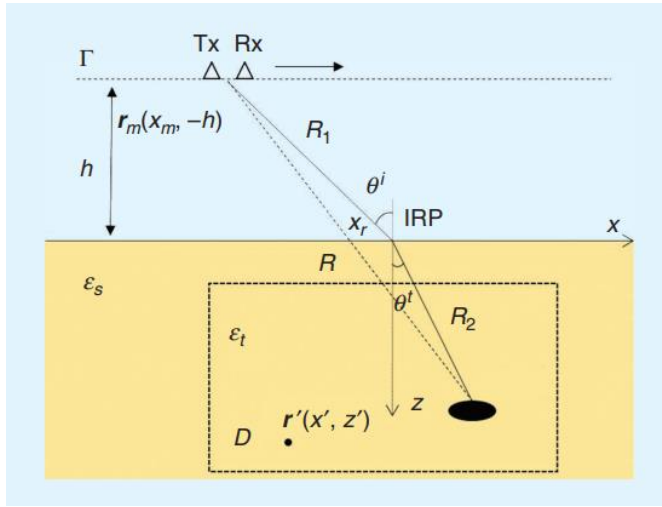


**Figure 14.** GPR imaging scenario characterized by a two-layered medium: the upper half space ( $z < 0$ ) is air, while the lower half space ( $z > 0$ ) is soil, which is assumed to be homogeneous. The antennas move along a rectilinear path  $\Gamma$  at a constant height  $h$ . IRP stands for Interface Reflection Point.

### 5.2.1 Spectral Domain (SD) Model

The first model for the computation of  $g_e$  and  $E_i$  is the so called Spectral Domain (SD) Model. It accounts for an exact expression of  $g_e$  and  $E_i$  for the half-space scenario of Figure 14 by resorting to the plane-wave expansion of the field radiated by an electric line source [37]. If the source is located at  $(x, z)$ , and the measurement point is  $(x_m, -h)$ , then  $g_e$  is written as [43]:

$$g_e(x_m, h, x, z, \omega) = -\frac{j}{2\pi} \int_{-\infty}^{\infty} \frac{e^{-jk_{zs}(u)z - jk_{z0}(u)h}}{k_{zs}(u) + k_{z0}(u)} e^{ju(x_m - x)} du \quad (5.2)$$

where  $u$  is the spectral variable corresponding to the spatial variable  $x$ ,

$$k_{z0,s}(u) = \sqrt{k_{0,s}^2 - u^2} \quad (5.3)$$

and  $k_{o,s}$  denote the wavenumber in free space and in the soil, respectively.

Finally, plugging (5.2) and (5.4) into (4.6) leads to the expression [57]

$$E_s(x_m, h, \omega) = \frac{j\omega\mu_0 I k_s^2}{4\pi^2} \int_{-\infty}^{\infty} \int_{-\infty}^{\infty} \int_{-\infty}^{\infty} \int_{-\infty}^{\infty} e^{j(u+v)x_m} e^{-j(u+v)x} \\ \times \frac{e^{-j(k_{zs}(u)+k_{zs}(v))z} e^{-j(k_{z0}(u)+k_{z0}(v))h}}{(k_{zs}(u) + k_{z0}(u))(k_{zs}(v) + k_{z0}(v))} \chi(x, z) du dv dx dz \quad (5.5)$$

where  $v$  is the spectral variable similar to  $u$ .

Note that the model given in (5.5) does not involve any more approximations than the Born approximation. However, (5.5) involves a noteworthy computational burden because a double-spectral integral needs to be computed for each measurement position  $x_m$ , frequency  $\omega$ , and point  $(x, z)$  of the investigation domain to build the operator  $L$ . Therefore, the Spectral Domain (SD) Model is not fully suited to process large-scale GPR data and investigation domains.

### 5.2.2 Ray-Based (RB) Model

The second model for the computation of  $g_e$  and  $E_i$  is the Ray-Based (RB) Model of signal propagation [58], which is based on the far-field approximation, i.e. the GPR antennas are supposed to be far from the investigation domain. According to Figure 14, the signal emitted by the TX antenna at  $(x_m, -h)$  travels along a ray that is transmitted in the soil at the interface reflection point (IRP)  $x_r$  and finally reaches the target point  $(x, z)$ . The IRP can be determined by applying Snell's law of refraction

$$\sin(\theta^i) = \frac{x_r - x_m}{R_1} = n_s \sin(\theta^t) = n_s \frac{x - x_r}{R_2} \quad (5.6)$$

where  $\theta^i$  and  $\theta^t$  are the incidence and transmission angles, respectively, with respect to the normal (see Figure 14);  $n_s = \sqrt{\epsilon_{rs}}$  is the soil-refractive index ( $\epsilon_{rs}$  is relative permittivity); and  $R_1 = \sqrt{(x_r - x_m)^2 + h^2}$  and  $R_2 = \sqrt{(x - x_r)^2 + z^2}$  are the path lengths along the incident and transmitted rays, respectively. Equation (5.6) leads to a fourth-order polynomial equation with respect to the unknown  $x_r$ . The equation can

be solved using any nonlinear equation solver by taking into account only the root that fulfills the condition  $x_r \leq x$ , if  $x \geq x_m$  or  $x_r \geq x$ , if  $x \leq x_m$ . Once the IRP is known,  $g_e$  and  $E_i$  can be straightforwardly calculated by applying geometrical optics concepts, and then the linear integral equation (4.6) writes as

$$E_s(x_m, h, \omega) = \frac{-jk_s^2 \eta_s I}{8\pi} \iint_D T_{12} T_{21} \frac{e^{-j2k_0(R_1 + n_s R_2)}}{R_1 + R_2} \chi(x, z) dx dz \quad (5.7)$$

where  $\eta_s = \sqrt{\mu/\epsilon_s}$  is the soil-intrinsic impedance, and  $T_{12}$  and  $T_{21}$  are the Fresnel's transmission coefficients at the air-soil interface [55]. The RB model in (5.7) simplifies the evaluation of the linear operator  $L$  with respect to the spectral model in (5.5). The computation cost for evaluating  $L$  is mostly related to the IRP calculation, which involves the solution of a fourth-degree polynomial equation for each pair of measurement and target points.

### 5.2.3 Equivalent Permittivity (EP) Model

The third model for the evaluation of  $g_e$  and  $E_i$  is the Equivalent Permittivity (EP) Model that allows avoiding the computational burden of the SD and RB models. The EP model is an approximated model of the RB model. This model introduces the equivalent permittivity (EP), i.e., an equivalent wavenumber, which allows regarding the propagation in the two-layered scenario as occurring in a medium with an equivalent and spatially varying dielectric permittivity. In other words, an equivalent ray from the source to the target (the dashed line in Figure 14) replaces the actual ray path from the source to the target undergoing refraction at the IRP. The equivalent wavenumber  $k_{seq}$  can be evaluated by matching the phase variation along the ray path in the two-layered medium to the phase in the equivalent medium

$$k_{seq} R = k_0 (R_1 + n_s R_2) \quad (5.8)$$

where  $R$  is the length of the equivalent-ray path. In principle, the calculation of  $k_{seq}$  in (5.8) requires computing the IRP for every source and target point as for the RB model. However, the computation can be simplified by assuming a negligible distance between  $x$  and  $x_m$ , i.e.  $x \approx x_m$ . Then, (5.8) writes as

$$k_{seq}(h + z) = k_0(h + n_s z) \quad (5.9)$$

which leads to the relative EP formula

$$\varepsilon_{seq}(z) = \left( \frac{\sqrt{\varepsilon_{rs}} z + h}{z + h} \right)^2. \quad (5.10)$$

The permittivity defined by (5.10) is equal to the one at the air-soil interface ( $z = 0$ ) and approaches the relative soil permittivity  $\varepsilon_{rs}$  for large  $z$ . According to the EP model, the linear integral equation to be inverted writes as

$$E_s(x_m, h, \omega) = \frac{-jk_s^2 \eta_s I}{8\pi} \iint_D T_{12} T_{21} \frac{e^{-j2k_{seq}R}}{R} \chi(x, z) dx dz \quad (5.11)$$

where the local transmission coefficients  $T_{12}$  and  $T_{21}$  are evaluated for the ray normal to the air-soil interface.

### 5.3 MULTILINES IMAGING APPROACH (MIA)

In order to get a 3D reconstruction of the investigated scene, which means be able to reconstruct the unknown contrast function  $\tilde{\chi}$  as a function of the three spatial coordinates  $(x, y, z)$ , it is necessary to fly the UAV-based radar imaging system along multiple measurement lines. The full 3D imaging issues can be listed as the necessity of a dense measurement grid made up of parallel measurement lines and the high computational cost. The needed spacing between parallel measurement lines entails operative constraints in terms of UAV flight control, which become more and more stringent as long as the radar working frequency increases, while the solution of the full 3-D problem entails an intensive computational cost, especially when the size of the investigated domain is large in terms of probing wavelength [55]. As contribution to this second issue, this thesis proposes a specific imaging strategy named Multiline Imaging Approach (MIA) [6]. It allows an effective 3D pseudo-representation of the investigated volume by exploiting data collected by down-looking antennas moved along multiple lines spaced into a plane (ideally) parallel to the air-soil surface. MIA exploits the following steps: 1) a partition of the whole 3-D investigated domain into several 2-D vertical domains, also referred to as slices; 2) the solution of imaging problems for each slice; and 3) the interpolation of 2-D images for obtaining a 3-D visualization. Each 2-D vertical domain is reconstructed by solving a linear inverse

scattering problem, where the 3-D platform positioning information, provided by the Carrier-phase Differential Global Positioning System (CDGPS) technique, is directly used in the inversion, as reported in [53]. Different from the procedure in [59], MIA processes data collected on multiple lines “close” to the 2-D vertical domain to perform the imaging.

Let us consider the 3-D reference scenario depicted in Figure 15.

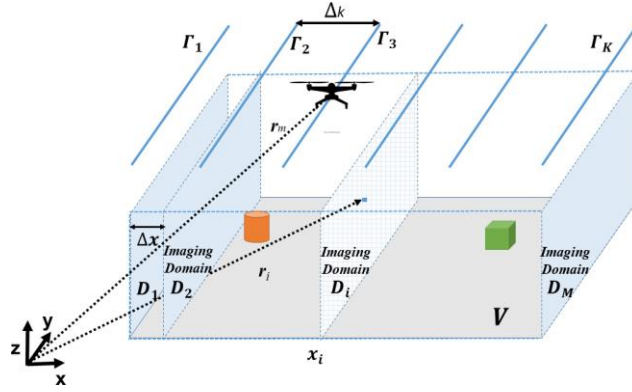


**Figure 15.** Multilines imaging scenario

The scene is investigated by means of a UAV mounted radar, operating in a monostatic mode and moving along  $K$  measurement lines. For the sake of simplicity and without losing generality, the measurement lines are supposed to be straight and parallel to the  $y$ -axis, evenly spaced along the  $x$ -axis and having the same length  $l$  and height  $h$ . Therefore, the generic measurement point  $r_m$  belonging to the generic measurement line  $\Gamma_k$  is described by the coordinates  $(x_m, y_m, z_m)$  such that  $y_m$  ranges from 0 to  $l$ ;  $x_m$  is equal to the  $x$  coordinate of  $\Gamma_k$ , i.e.,  $x_m = x_k = (k - 1)\Delta k$ , with  $k = 1, \dots, K$  and  $\Delta k$  being the spacing between two next measurement lines;  $z_m$  is equal to  $h$ . It is worth pointing out that in practice, the measurement lines are never straight, parallel, evenly spaced and having same and constant height, being the UAV stability poor. Therefore, the generic measurement point  $r_m$  is defined by accounting for the UAV positioning data as estimated by the CDGPS technique [48]. The origin of the reference coordinate system in Figure 15 corresponds to the position of the ground-based GPS station; the generic point  $r_i$  in the imaging domain  $D_i$  is defined accordingly and the generic measurement point  $r_m$  is estimated by means of the CDGPS. In this way, the UAV positioning data are directly exploited in the imaging strategy; in other words, no motion compensation and/or autofocusing procedure are applied. The investigated volume  $V$  is sliced in multiple 2-D vertical imaging domains,

i.e.,  $V = \bigcup_{i=1}^M D_i$ , such that: 1) each vertical imaging domain  $D_i$  is at a fixed  $x_i$  and belongs to the  $(y, z)$  plane and 2) the spacing between the domains  $D_i$  is uniform:  $\Delta x = x_i - x_{i-1}$ . A practical criterion for setting the spacing is  $\Delta x \leq \delta x/2$ , where  $\delta x$  is the cross-track resolution limit for UAV radar imaging system as defined in [34]:

$$\Delta x \leq \frac{c}{4B} \sqrt{1 + \frac{2h}{c/2B}} \quad (5.12)$$

where  $c$  is the speed of light and  $B$  is the radar bandwidth.

According to this criterion and taking into account that it is hard to have a dense grid of measurement lines, we assume that the number of the imaging slices  $M$  is larger compared with the number of measurement lines  $K$ , i.e.,  $M \geq K$ .

MIA is different from the approach presented in [59], because this latter accounts for the same number of measurement lines and 2-D imaging domains and faces the imaging by exploiting data collected along a single line (i.e., that overlapping the imaging domain). In MIA, more than one measurement line may concur to perform the imaging of a 2-D domain (slice). Specifically, to face the imaging problem referred to the generic vertical domain  $D_i$ , MIA selects the subset of measurement lines ( $\hat{\Gamma}_k = \bigcup_{k=1}^K \Gamma_k$ ) by computing the distance between the coordinate  $x_i$ , defining the location of  $D_i$  along the x-axis, and the coordinate  $x_k$  of the measurement lines and compares such a distance with a couple of fixed distance thresholds ( $T_1, T_2$ ), as follows:

$$\begin{cases} H_1: |x_i - x_k| \leq T_1 \\ H_2: T_1 \leq |x_i - x_k| \leq T_2 \end{cases} \quad (5.13)$$

being  $T_1 \leq T_2$ . When the  $H_1$  hypothesis is satisfied, only the data referred to the  $k$  measurement line are taken into account to perform the imaging of  $D_i$ . Conversely, when the hypothesis  $H_2$  is satisfied, all the measurement lines such that the distance between  $x_i$  and  $x_k$  is not larger than  $T_2$  are exploited. The threshold  $T_1$  is fixed as  $\Delta x$  (i.e., the spacing between the vertical imaging domains). Hence, when  $H_1$  is satisfied, only information provided by the closest radargram is exploited. The threshold  $T_2$  is chosen as tradeoff between the possibility of exploiting data collected along multiple measurement lines and the necessity of avoiding the effect of clutter, which is the contribute given by targets not belonging to the reconstructed imaging domain  $D_i$ . In the following,  $T_2$  is fixed equal to  $\Delta k$ , i.e., the spacing between two next measurement lines. At this stage, the imaging problem is faced, for each 2-D vertical domain  $D_i$ , by exploiting a microwave tomographic-based strategy similar to that proposed in [53].

Once the  $M$  tomographic images have been obtained, the 3-D visualization of the investigated volume  $V$  is achieved by performing a linear interpolation, which allows the merge of 2-D images. A brief description of MIA is given by the flowchart in Figure 16.

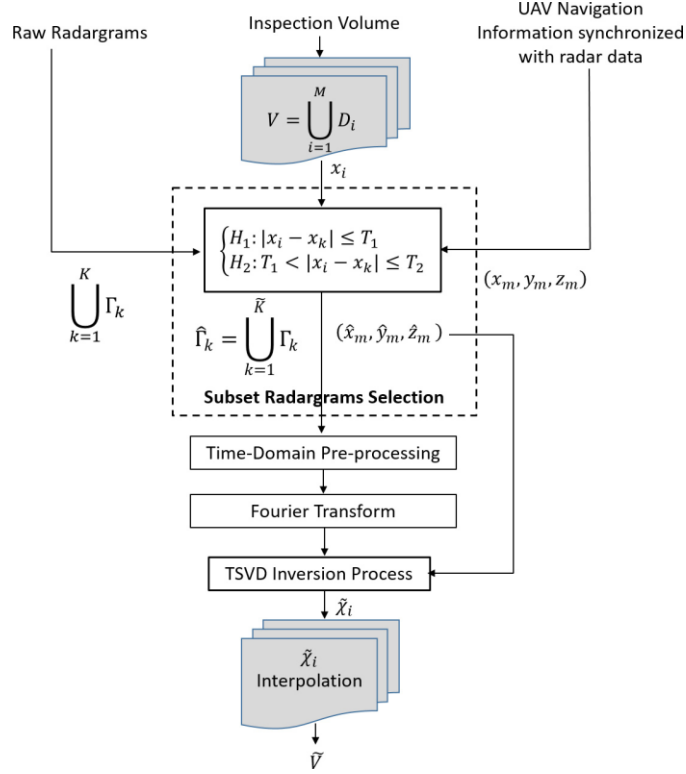


**Figure 16.** MIA strategy flowchart.

The computational complexity of MIA depends on the computation of the SVD of the discretized version of the scattering operator in (4.7), mainly. Hence, it is given by:

$$M \times (Q \times F)^2 \times n^2 \quad (5.14)$$

where  $M$  is number of vertical domain  $D_i$ ;  $Q$  is the overall number of measurement points, which is given by the product of the number of measurement points  $q$  along a single direction and the number  $l$  of selected measurement lines satisfying  $H_1$  or  $H_2$ , with  $l < K$ ;  $F$  is the number of angular frequencies;  $n$  is the number of pixels discretizing a single direction. The product  $(Q \times F)$  represents the amount of data considered to achieve the tomographic image of  $D_i$ . Therefore, the computational burden of MIA results much smaller than the computational burden of a full 3D approach:

$$M \times (Q \times F)^2 \times n^2 \ll (\bar{Q} \times F)^2 \times n^3 \quad (5.15)$$

being  $\bar{Q}$  the overall number of measurement points of a full-3D approach. The validity of the equation (5.15) stays in the definition of  $\bar{Q}$  that is given by the product  $q \times L$ , where  $L$  represent the number of measurement lines used for the full 3D, therefore  $L > K > l$ . A Point Spread Function (PSF) resolution analysis concerning the adoption of MIA has been proposed in [60].

In addition, MIA has been experimentally validated at Archaeological Park of Paestum and Velia (Paestum, Italy). The obtained results will be presented as contribution to the Chapter 6, which will deal with UAV-based radar imaging high frequency systems.

#### 5.4 HORIZONTAL IMAGING MODEL FOR FREE SPACE SCENARIO

The term horizontal imaging refers to the adoption of a 2D horizontal imaging domain, thus entailing a dependence of the reconstructed contrast function  $\tilde{\chi}$  by the  $(x, y)$  spatial coordinates. The scenario is the one in Figure 17 where the horizontal imaging plane  $D$  has been overlapped top the plane of the scene containing targets.

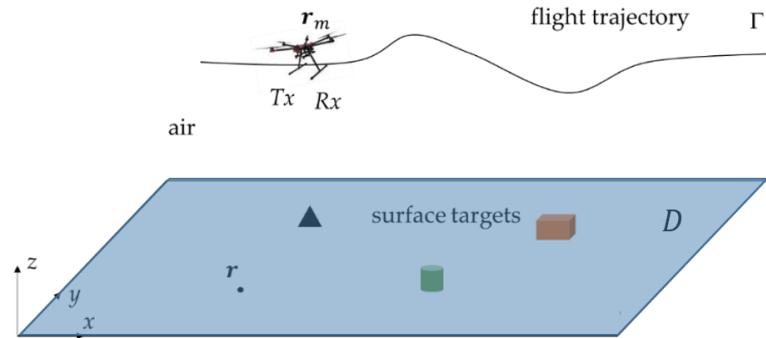


**Figure 17.** UAV-based radar imaging. Horizontal imaging scenario.

Starting from the equation (4.13) derived by computing the adjoint of the forward scattering operator, it is possible to obtain the following expression for the contrast function by applying the Method of Moments:

$$\tilde{\chi}(x_p, y_q) = \sum_{m=1}^M \sum_{n=1}^N E_S(x_m, y_m, z_m, \omega_m) \frac{e^{\frac{j2\omega_n}{c_0} (x_p - x_m)^2 + (y_q - y_m)^2 + z_m^2}}{(x_p - x_m)^2 + (y_q - y_m)^2 + z_m^2} \quad (5.16)$$

where  $p = 1 \dots P$  and  $q = 1 \dots Q$  are the indexes for the  $P \times Q$  pixels discretizing the image plane (Figure 18),  $M$  is the number of measurement points  $(x_m, y_m, z_m)$ ,  $m = 1, 2 \dots, M$  and  $N$  is the number of angular frequencies  $\omega_n$ ,  $n = 1, 2 \dots, N$  sampling the working frequency bandwidth  $\Omega$ . According to the assumption of antennas having a broad radiation pattern, equation (5.16) sums coherently the multi-frequency data collected along the whole trajectory  $\Gamma$  for each pixel in  $D$ . Therefore, the radar image is obtained by computing Equation (5.16) for all pixels in  $D$  and plotting the magnitude of the retrieved reflectivity values normalized with respect to their maximum value. In this process, the precise measurement positions of the UAV obtained with the CDGPS processing are considered. The exploitation of the positioning information allows accurate images, as already pointed out in the airborne radar imaging context [61, 53].

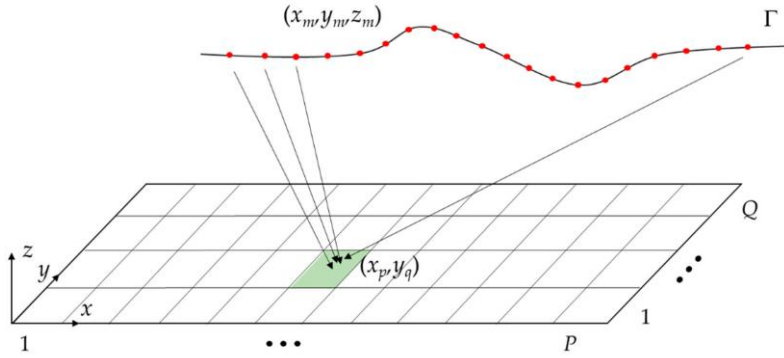


**Figure 18.** Discretization of the UAV-based radar horizontal imaging problem.

# Chapter 6: High Frequency Radar Imaging System by UAV

---

This chapter deals with high frequency UAV radar imaging, i.e. with the imaging of on-surface targets, and presents experimental results.

Specifically, the chapter deals with data collected by means of two high frequency UAV radar system prototypes, i.e. System HI assembled in the GNC lab of the University of Napoli ‘Federico II’, and System HII developed in the frame of the VESTA Project in collaboration with TopView s.r.l.. Section 6.1 describes the hardware components of the two systems. Section 6.2 deals with experimental results obtained by applying strategies ‘A’, ‘B’ and MIA on data acquired in different measurement campaigns via Systems HI and HII. Results about a theoretic analysis of horizontal imaging performances is also presented with the aim of investigating how the reconstruction capabilities of the adopted radar imaging approach are affected by the measurement configuration parameters.

## 6.1 DEVELOPED PROTOTYPES

The System HI [14] has been developed at the GNC Lab of the University of Napoli ‘Federico II’. The system is mainly composed by:

- The mini-UAV platform DJI F550 hexacopter able to fly at very low speeds (about 1 m/s), thus ensuring a small spatial sampling step and the ability to take-off and land from a very small area;
- The Pulson P440 Radar system: is a light and compact time-domain device transmitting ultra-wideband pulses (about 1.7 GHz bandwidth centred at the carrier frequency of 3.95 GHz) with a low power consumption [62]. The radar system is mounted rigidly on the UAV body (strapdown installation) and no gimbal is adopted. The limited altitude dynamics experienced during flights (very low ground speed and wind speed conditions resulting in small and almost constant roll/pitch angles), the relatively large radar antenna lobes and the limited baseline between the radar antenna and the drone centre of mass are such that altitude/pointing knowledge does not play a significant role;

- GPS receivers/antennas: two single-frequency Ublox LEA-6T devices are chosen, one mounted onboard the UAV and the other one used as a ground-based station. Both are connected to an active patch antenna. The antenna is directly placed on the ground (Figure 19b) in order to get from CDGPS a direct estimate of the height above ground for the antenna mounted on the drone;
- CPU controller: Linux-based Odroid XU4 is devoted to managing the data acquisition for both radar system and on-board GPS receiver, while assuring their time synchronization.

The possibility to estimate the trajectory of the UAV platform depends on the quality of the embarked navigation sensors. By using a standalone on-board GPS receiver, the achievable absolute positioning accuracy is given into a global reference frame, such as WGS84 (World Geodetic System 1984), and is defined according to the specifications provided by the US Department of Defense [63]. Absolute GPS localization errors are estimated as the product of the User Equivalent Range Error (UERE), which is the effective accuracy of the localization errors along the pseudo-range direction, the Horizontal Dilution of Precision (HDOP) and Vertical Dilution of Precision (VDOP). These latter are dimensionless quantities expressing the effect of satellites-receiver geometry. Representative values of UERE, HDOP and VDOP, for good GPS visibility conditions, are 3.5 m and 6.6 m, respectively [47].



**Figure 19.** M-UAV radar imaging system (System HI): (a) DJI F550 hexacopter with on-board equipment; (b) ground-based GPS station.

System HII [64] has been developed in the frame of the VESTA Project in collaboration with TopView s.r.l. The aims of the VESTA project were the design and

the experimental assessment of an ultra-light radar prototype suitable to be mounted on board a micro-UAV platform with cultural heritage purposes. System HII has been assembled using the frame of the DJI S900 hexacopter (Figure 20a), which has been chosen as the unmanned platform to carry on the overall payload. The radar sensing system is still the Pulson P440 equipped with two Ramsey LPY26 log periodic PCB antennas. The along-track aperture angle of the antennas is  $80^\circ$ , while the across track aperture angle is  $110^\circ$ . The U-blox EVK-M8T receiver provides the system positioning information. Since it is able to collect raw GNSS data (i.e. pseudo ranges with respect to in-view satellites), it can be used in conjunct with a ground GNSS station to provide differential GNSS estimates of the UAV positions flown during the measurement campaign. This is done through the implementation of a PPK technique. Data storage and synchronization is performed through the use of the Raspberry Pi 3 module, which works as on-board computer. It is a 1.2 GHz Quad Core with a 64bit CPU and 1 GB RAM and it allows wireless LAN and Bluetooth connectivity, being equipped with Ethernet and USB ports. A LiPO battery and a DC-DC converter are considered to power the payload. The overall components of the payload and all the needed connections are shown in Figure 20b. The above described components are accommodated in an ad hoc designed case (see Figure 20c), which was realized with a 3D printer and can be easily mounted on a UAV platform. The total payload weight is about of 0.8 Kg.

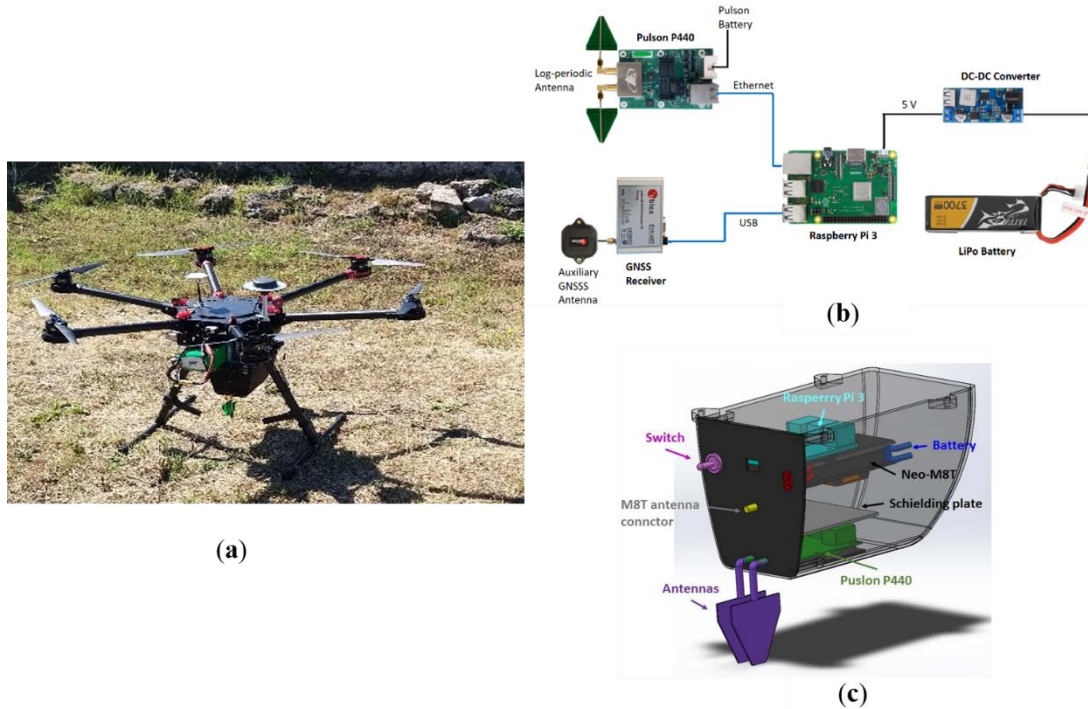


**Figure 20.** System HII. (a) DJI S900 hexacopter with on-board equipment. (b) Components of the payload. (c) Payload architecture.

## 6.2 EXPERIMENTAL RESULTS

This section proposes the experimental validation of the developed prototypes and the tests of the processing chains introduced in Chapter 3, Section 3.3 (i.e. Strategies ‘A’ and ‘B’) and Chapter 5, Section 5.3 (i.e. MIA). For this Chapter the Strategy ‘A’ adopts a free-space propagation vertical imaging model, while the strategy ‘B’ implements a free-space propagation horizontal imaging model.

### 6.2.1 Vertical imaging performance: the case of a single track

Strategy ‘A’ (subsection 3.3.1) has been used to process radar data acquired with System HI in two different measurement campaigns with the aim of verifying and comparing the radar imaging performance when UAV positioning data are provided by GPS or CDGPS. The first test was carried out in Acerra, a small town in suburban area of Naples, on a site for amateur UAV flights testing; the second test was carried out in San Nicola la Strada, a rural area closest to the famous Royal Palace of Caserta, on a site made available by TopView srl [65]. The imaging capabilities are evaluated in terms of ability to detect targets, to determine their elevation from the ground (i.e., the air-soil interface) and to estimate their relative distance. The experimental tests

were carried out during summer and winter seasons, with low or moderate wind conditions, and, by using targets with different geometrical and electromagnetic features.

### 6.2.1.1 Experimental test in Acerra

The first experimental test was performed on 5 July, 2019, during a hot sunny day with weak wind state [34]. Three targets were considered: one cylindrical wood trunk (here referred as target 1) placed at 0.5 m above the ground, whose size are: 0.6 m length and 0.14 m of diameter; two metallic trihedral corner reflectors, having size  $0.40\text{m} \times 0.40\text{m} \times 0.57\text{m}$  and referred as target 2 and target 3. These latter were used as on-ground targets and target 3 was covered with a cardboard box. The targets were positioned along a straight line, with a relative distance of 10 m (see Figure 21) [34]. The main radar system parameters adopted for data collection are reported in Table 2 [34].

**Table 2.** Operative Radar System Parameters: First Test Case.

Parameters	Specification
Carrier Frequency	3.95 [GHz]
Frequency Band	1.7 [GHz]
Pulse Repetition Frequency	14.28 [Hz]
Sampling Time	61.1 [ps]
Start Fast Time	5.1 [ns]
End Fast Time	122.3 [ns]
Integration Index	12

The UAV was manually piloted (in GPS mode) and two flights at different altitudes, herein indicated as Track 1 and Track 2, were carried out. Both tracks were performed on the same scenario by positioning the UAV more or less at the same starting point  $(x, y)$ . The first flight had a duration of 22.3 s and covered a 36.5 m long path at the mean flight altitude of about 4.5 m; along this track, data were gathered in 319 not evenly spaced measurement points. Track 2 had a duration of 28.6 s and covered a 33 m long path at an average flight altitude about 10 m; along this track data were gathered in 409 not evenly spaced measurement points.

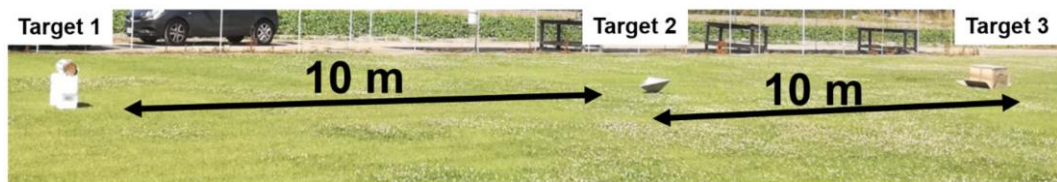


**Figure 21.** First test case: radar imaging scenario.

Figures 22 and 23 depict the raw radargrams (Figures 22a and 23a), the estimated east–north UAV trajectory and the corresponding along-track direction (Figures 22b and 23b), the estimated UAV altitudes and the corresponding average value (Figures 22c and 23c). Specifically, Figures 22b and 23b depict a zoom of the estimated east–north trajectories obtained by means of GPS (blue color) and CDGPS (red color) for both the tracks, respectively. Moreover, these Figures show the corresponding zoom of the along-track directions (dashed blue line—GPS, dashed red line—CDGPS). Similarly, Figures 22c and 23c show, as blue and red solid lines, the estimated altitudes and the corresponding averages (dashed blue and red lines). The dashed lines in Figures 22 and 23 depict the straight line obtained by means of the MoCo. In Figure 22a, three diffraction hyperbolas corresponding to targets 1, 2, and 3 are clearly visible and their apexes are placed at 5 s, 12.5 s, and 17.5 s along the slow time axis. In Figure 22a, the presence of horizontal constant signals accounts for the antennas coupling, while the signal appearing at fast time values higher than 60 ns are clutter due to lateral objects.

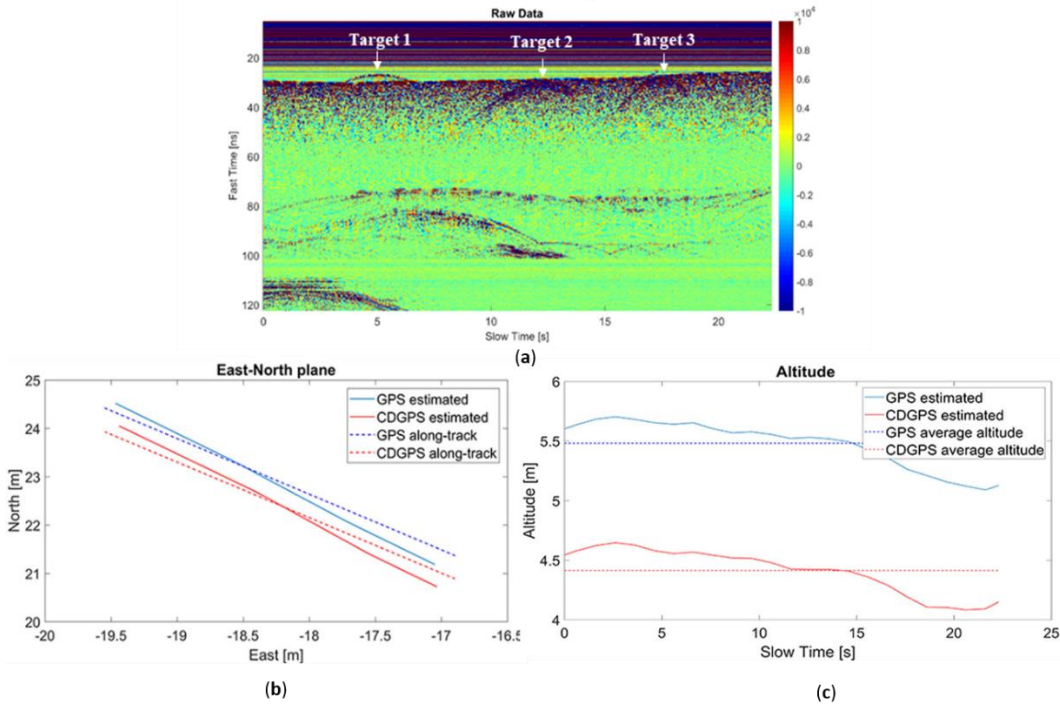


**Figure 22.** Test 1-Track 1: (a) raw data; (b) east–north UAV positions estimated by GPS (solid blue line) and CDGPS (solid red line), along-track direction defined by GPS (dashed blue line) and CDGPS (dashed red line); (c) UAV Altitude estimated by GPS (solid blue line) and CDGPS (solid red line), average altitude defined by GPS (dashed blue line) and CDGPS (dashed red line).

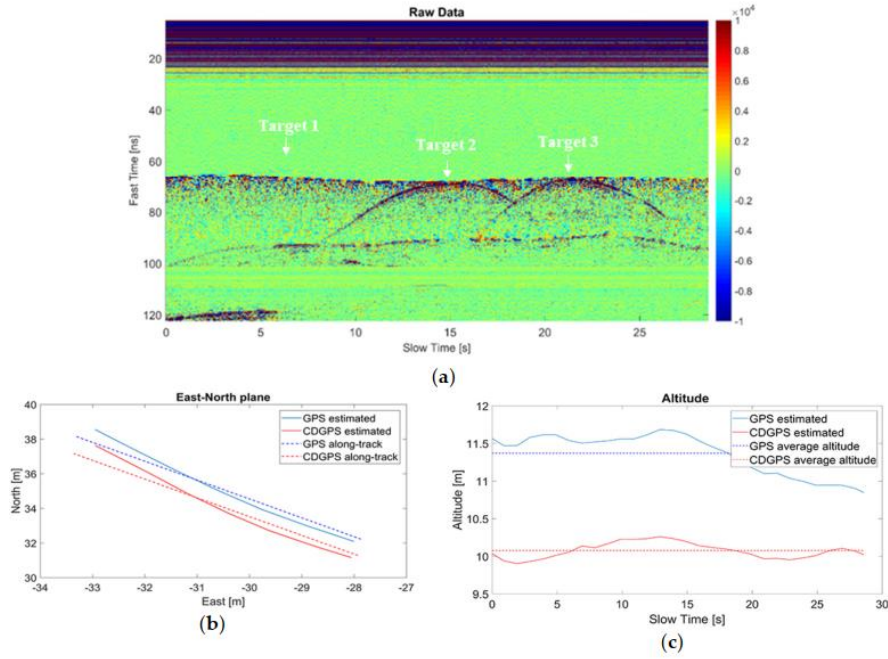


**Figure 23.** Test 1-Track 2: (a) raw data; (b) east–north UAV positions estimated by GPS (solid blue line) and CDGPS (solid red line), along-track direction defined by GPS (dashed blue line) and CDGPS (dashed red line); (c) UAV Altitude estimated by GPS (solid blue line) and CDGPS (solid red line), average altitude defined by GPS (dashed blue line) and CDGPS (dashed red line).

Despite these undesired signals, the UAV radar system is capable of detecting the three targets as well as to recognize that the last encountered corner reflector (target 3) is hidden by a weakly scattering object, as testified by the presence of a small apex above the last hyperbola. For what concerns Track 2, unfortunately, the hyperbolas related to the target 1 (the wood trunk) is not clearly visible in the raw radargram (see Figure 23a). This effect is due to the smaller intensity of the field backscattered by the trunk being higher flight altitude (the radar transmits the same power whatever the flight altitude is). In Figure 23a, the three hyperbolas related to the three targets have apexes placed at 6 s, 15 s and 21 s along the slow time axis.

In this first test case, GPS and CDGPS provide similar trajectories along the east–north plane, with a slowly varying offset of the order of 1 m (Track 1) or 2 m (Track 2), whereas GPS altitudes are higher than those estimated by CDGPS. Moreover, for Track 1, the GPS and CDGPS UAV altitude profiles differ of a quasi-constant bias; whereas for Track 2 the GPS altitude are affected by a drift (see Figures 22c and 23c, respectively). Given the statistics about the estimated CDGPS uncertainty (based on residuals), reported in subsection 6.2.1.3 (Table 8), CDGPS measurements can be assumed as a benchmark for standalone GPS. Thus, the drift of the altitude

differences can be interpreted as a vertical error drift for the standalone GPS solution. Figures 24 and 25 depict the aligned and interpolated radargram after the MoCo and standard time-domain radar pre-processing for Tracks 1 and 2, respectively.

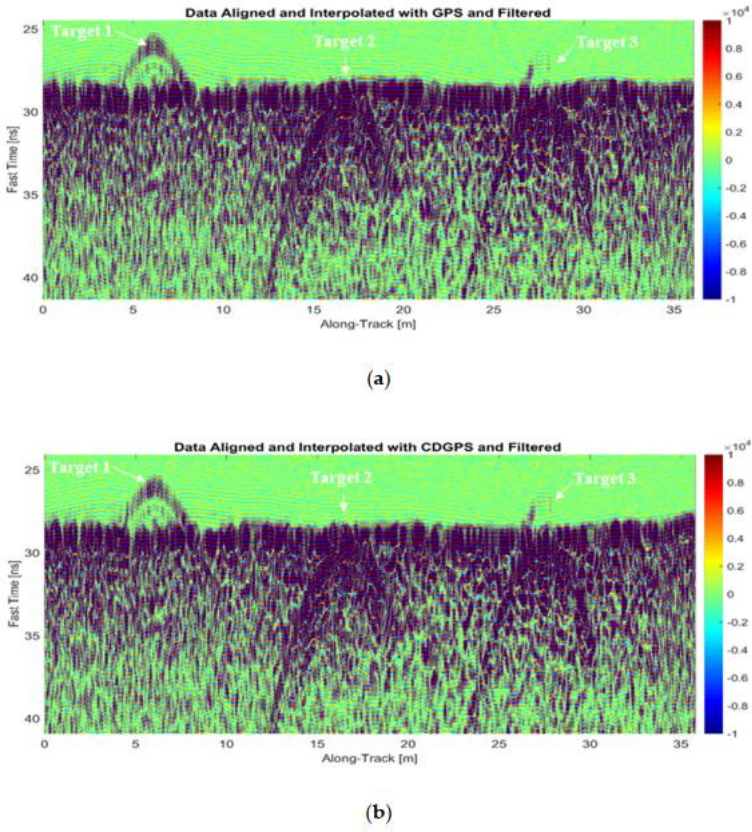


**Figure 24.** Processed radargram Test 1-Track 1: (a) aligned ad interpolated radargram by exploiting GPS information and after filtering operations; (b) aligned ad interpolated radargram by exploiting CDGPS information and after filtering operations

Figure 24 corroborates that in Test 1-Track 1, by using both GPS and CDGPS information, MoCo allows at compensating the altitude variations and, indeed, the air-soil interface appears as an almost flat profile, as it is actually. Conversely, Figure 25 shows that in Test 1-Track 2, while MoCo driven by CDGPS achieves a result similar to Test 1-Track 1, the result based on GPS is worse because the air-soil interface does not have an almost flat profile. This uncompensated effect is due to the drift affecting the estimated GPS altitude (see Figure 23c).

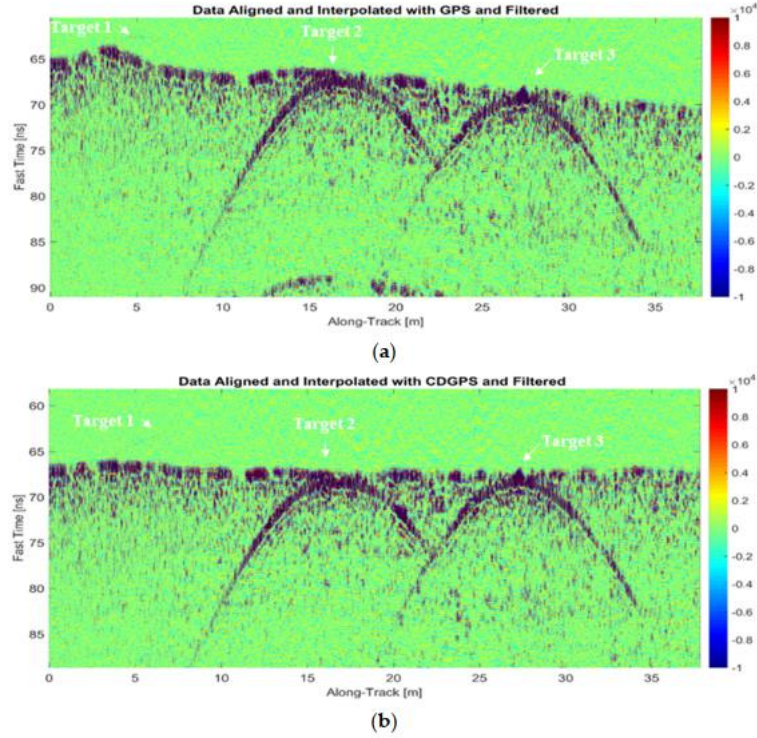


**Figure 25.** Processed radargram Test 1-Track 2: (a) aligned ad interpolated radargram by exploiting GPS information and after filtering operations; (b) aligned ad interpolated radargram by exploiting CDGPS information and after filtering operations.

Tables 3 and 4 list the signal processing parameters adopted to process the radargrams for Track 1 and Track 2 (after MoCo), respectively. The frequency step represents the step used to sample the frequency spectrum of the collected data (ranging from  $f_{\min}$  and  $f_{\max}$ ) and is calculated according to the Nyquist criterion for avoiding aliasing problems [66] in the reconstruction process. The horizontal (i.e., x-axis) size of the overall investigated domain is equal to the extent of the along-track measurement line as defined by the MoCo. Conversely, the vertical (i.e., z-axis) size is such to consider about 1 m up and 2 m below the air-soil interface, whose position is set according to the average altitude value as computed from standalone GPS and CDGPS data. In other words, the zero of the z-axis is in correspondence to the average vertical position of the radar antenna system. Moreover, Tables 3 and 4 give the subdomain apertures used to apply the Shift and Zoom procedure, which correspond to 5 m and 7 m for Track 1 and Track 2, respectively. These parameters have been chosen by measuring the target hyperbola extent in the processed radargram and take into account that the hyperbola extent is dictated by the antenna footprint and thus by

the flight altitude. This justified why the subdomain aperture considered for the Track 2 is larger than the one used for Track 1.

**Table 3.** Signal Processing Parameters: Track 1.

Parameters	Specification
Time Gating	Start Time 22 (ns) End Time 39 (ns)
Frequency range	$f_{min} = 3.1$ (GHz) $f_{max} = 4.8$ (GHz)
Frequency step	30 (MHz)
Imaging Domain	x-axis size: 36.50 (m) dx: 0.025 (m) z-axis size: 3.45 (m) dz: 0.025 (m)
TSVD threshold (T)	-20 (dB)
Subdomain Aperture (L)	5 (m)

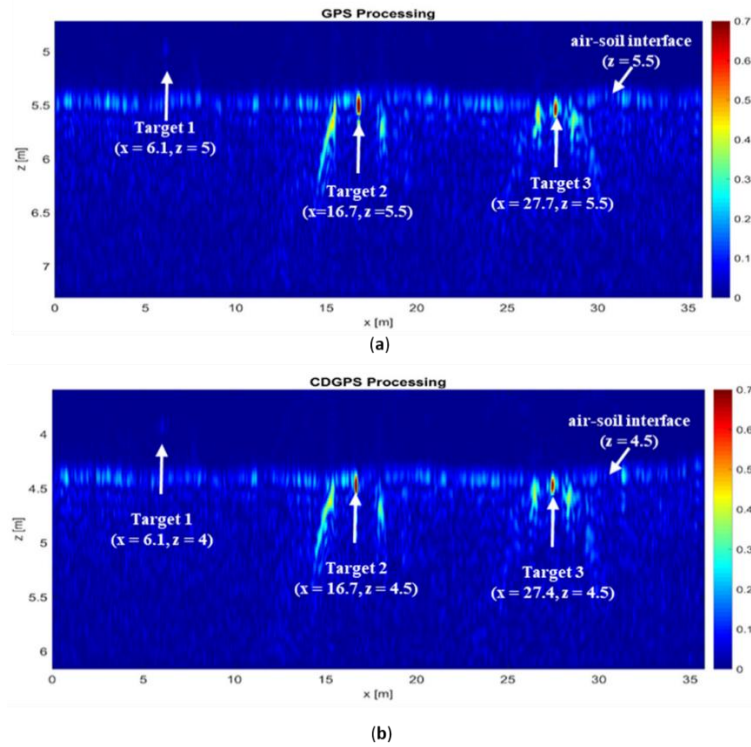
**Table 4.** Signal Processing Parameters: Track 2.

Parameters	Specification
Time Gating	Start Time 57 (ns) End Time 87 (ns)
Frequency range	$f_{min} = 3.1$ (GHz) $f_{max} = 4.8$ (GHz)
Frequency step	20 (MHz)
Imaging Domain	x-axis size: 37.30 (m) dx: 0.025 (m) z-axis size: 5.65 (m) dz: 0.025 (m)
TSVD threshold (T)	-15 (dB)
Subdomain Aperture (L)	7 (m)

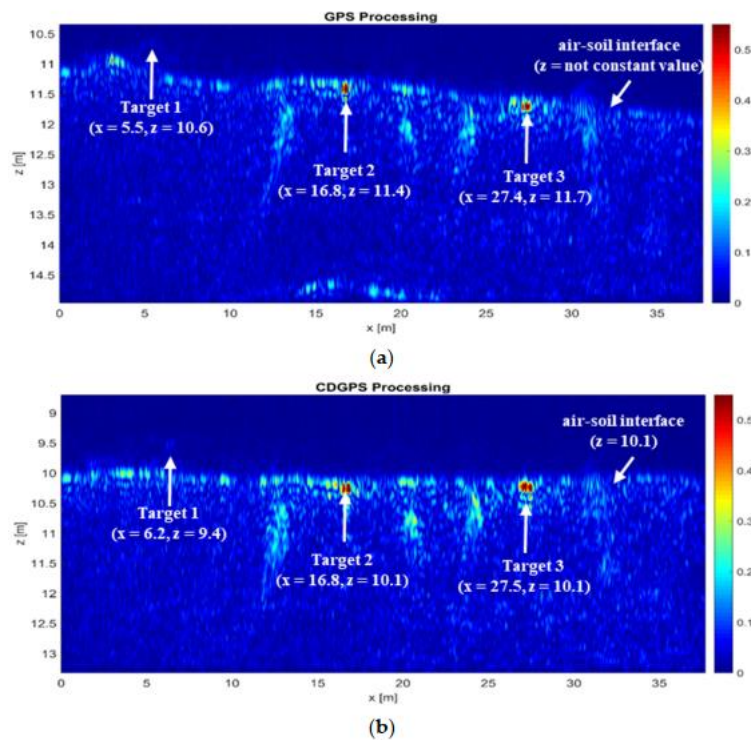
The tomographic images referred to Test 1-Track 1 and Test 1-Track 2, are depicted in Figures 26 and 27, respectively. These Figures show focused images wherein the metallic corner reflectors are clearly distinguishable, whereas the response of wooden trunk is low due to its lowest reflectivity. Moreover, these figures allow an approximate positioning of the targets.

Figure 26a,b provide an accurate estimation of the altitude of the targets with respect to the air- soil interface; while they give an overestimation of the relative distance among the targets, which is of 1 m in the worst case (i.e., distance between target 2 and target 3 by using GPS data). The air-soil interface appears at  $z = 5.5$  m in Figure 26a and at  $z = 4.5$  m in Figure 26b and this positioning difference is associated to the altitude estimation bias between GPS and CDGPS.

Tomographic reconstructions, depicted in Figure 27a,b, provide an approximate localization of the targets by using both GPS and CDGPS, but standalone GPS data do not allow to correctly reconstruct the air-soil interface profile (it is not flat in Figure 27a).



**Figure 26.** Tomographic images Test 1-Track 1 obtained by Shift and Zoom TSVD algorithm: (a) GPS based motion compensation (MoCo); (b) CDGPS based MoCo.



**Figure 27.** Tomographic images Test 1-Track 2 obtained by Shift and Zoom TSVD algorithm: (a) GPS based MoCo; (b) CDGPS based MoCo.

### 6.2.1.2 Experimental test in San Nicola la Strada

The second measurement campaign was carried out on the 21 February, 2020, at San Nicola La Strada (CE) during a cold day with a moderate wind state. The investigated scene is illustrated in Figure 28, where four targets were placed on the grass along a straight line. Target 1 was a couple of chipboard shelves, having size  $0.38 \times 0.60 \text{ m}$ , placed at  $0.70 \text{ m}$  above the ground and with a relative distance of  $5 \text{ m}$  from the target 2. The target 2 was a wood trunk placed at  $0.5 \text{ m}$  above the ground and with a distance of  $10 \text{ m}$  far from target 3. Target 3 was a void inside small box of plasterboard, having size of  $0.53 \times 0.53 \times 0.1 \text{ m}$ . Finally, as target 4 was used a tuff brick of dimensions  $0.27 \text{ m} \times 0.41 \text{ m} \times 0.14 \text{ m}$ , placed on ground and far  $5 \text{ m}$  from target 3. The upper side of target 3 and target 4 are  $0.53 \text{ m}$  and  $0.27 \text{ m}$  from the ground, respectively.

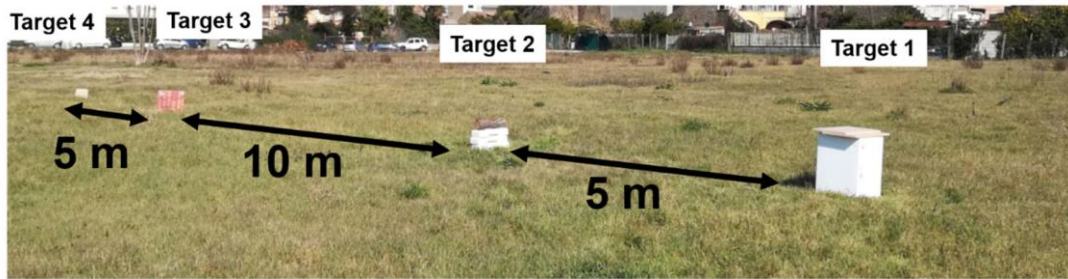


Figure 28. Measurement scenario.

Two flights were performed, both manually piloting the UAV in GPS mode. It is worth pointing out that due to the wind effect, Target 3 was repositioned before carrying out the second flight and, in order to assure its stability, which was compromised by foliage presence on the ground, it was located  $9 \text{ m}$  far from Target 2

and 6 *m* far from Target 4. The radar operative parameters adopted for this second test case are reported in Table 5.

**Table 5.** Operative radar system parameters

<b>Parameters</b>	<b>Specification</b>
Carrier Frequency	3.95 (GHz)
Frequency Band	1.7 (GHz)
Pulse Repetition Frequency	10 (Hz)
Sampling Time	61.8 (ps)
Start Fast Time	5.1 (ns)
End Fast Time	87.2 (ns)
Integration Index	12

The first flight covered 27 *m* in 41.9 *s* with an average flight altitude of about 4.2 *m*; along this track, 420 not evenly points were collected. Track 2 had a duration of 37.9 *s* and covered 32.20 *m* with an average altitude of 5.6 *m*; along this track, 380 unevenly radar scans were collected. Figures 29 and 30 show the raw radargrams acquired along the two flights and the UAV positions estimated by GPS and CDGPS. Within the east–north plane, positioning differences appear as smoothly varying offsets of several meters (Track 1) or a few meters (Track 2). As concerns the altitude difference, it shows some significant variations during the time interval corresponding

to Track 1, while it assumes smaller values in Track 2. As stated above, CDGPS can be assumed as a reference for standalone GPS performance.

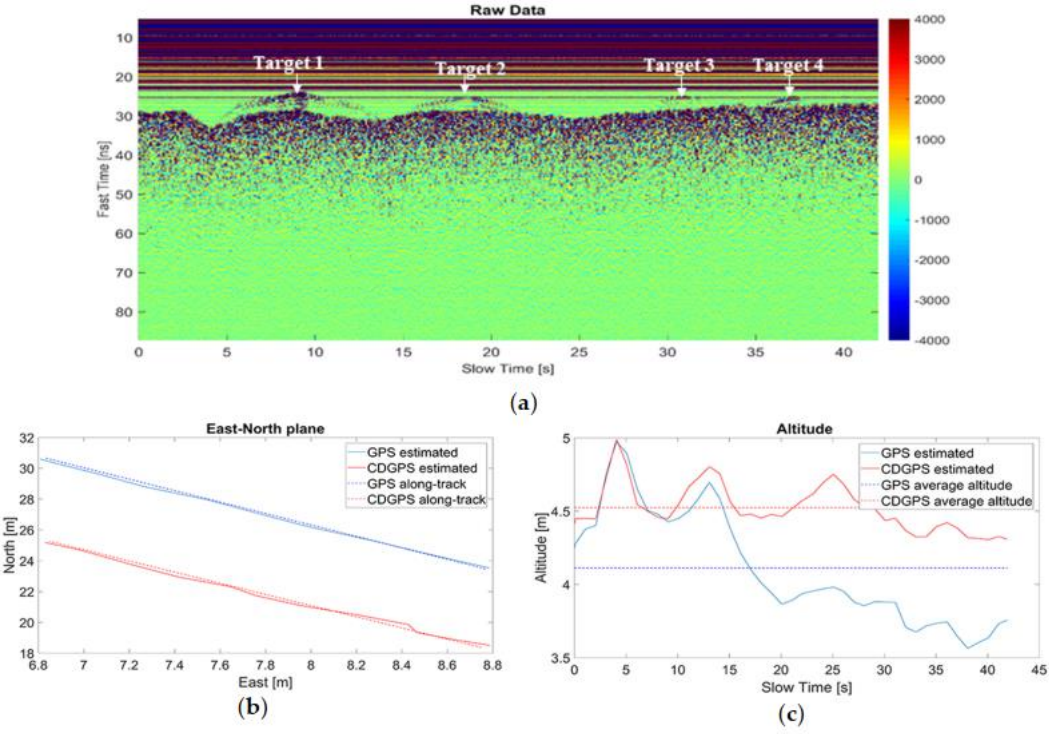


**Figure 29.** Track 1. (a) Raw data.(b) East–north UAV positions estimated by GPS (solid blue line) and CDGPS (solid red line), along-track direction defined by GPS (dashed blue line) and CDGPS (dashed red line). (c) UAV Altitude estimated by GPS (solid blue line) and CDGPS (solid red line), average altitude defined by GPS (dashed blue line) and CDGPS (dashed red line).

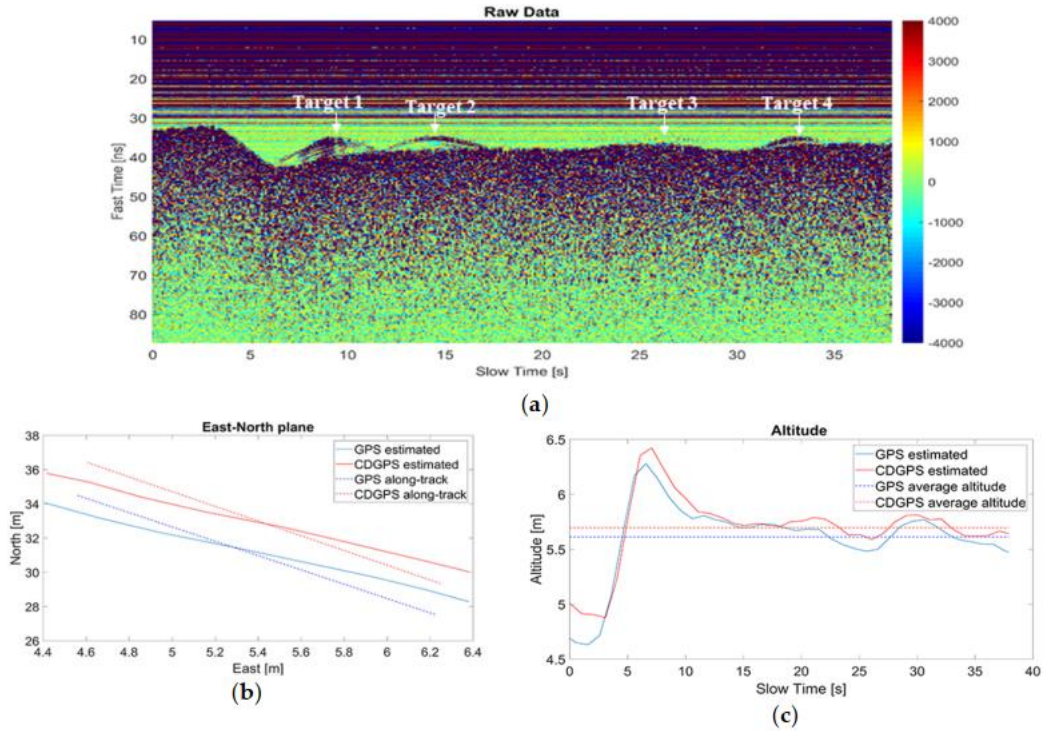


**Figure 30.** Track 2. (a) Raw data; (b) East–north UAV positions estimated by GPS (solid blue line) and CDGPS (solid red line), along-track direction defined by GPS (dashed blue line) and CDGPS (dashed red line). (c) UAV Altitude estimated by GPS (solid blue line) and CDGPS (solid red line), average altitude defined by GPS (dashed blue line) and CDGPS (dashed red line).

The diffraction hyperbolas corresponding to the four targets are clearly visible in Figure 29a and their apexes along the slow time axis are at 9 s, 19 s, 31 s and 37 s. In Figure 30a, the hyperbolas corresponding to Target 1, 2, and 4 can be easily identified at 9 s, 15 s, and 33 s; while the response of Target 3 is less visible. This may be due to less intensity of the backscattered signal caused by the flight altitude, which is higher with respect to the Track 1. In this second test case, the flight trajectory estimated by GPS and CDGPS have a similar path into the North-East plane, even if there is a bias that is more significant for Track 1 than for Track 2 (see Figures 29b and 30b); while the altitudes exhibit different profiles, even if their average values are quite similar. The tomographic images referred to Track 1 and Track 2 are depicted in Figures 31 and 32, respectively. These images have been obtained by adopting the ‘A’ signal processing strategy with the signal processing parameters indicated in Tables 6 and 7, respectively. The Subdomain Apertures have the same size, i.e., 4 m. This parameter has been chosen again by considering the target hyperbola extent in the processed radargrams. Figures 31b and 32b corroborate that the tomographic images

obtained by exploiting CDGPS data are focused images in which the air–soil interface appears flat, as it is actually, and the relative distance among all targets as well as their elevation from the ground are estimated properly. The maximum error is of 0.7 m and regards the estimation of the distance between Target 1 and Targets 2 provided by the tomographic image referred to Track 2. Focused images allowing an approximated localization of the targets are achieved also by using GPS data even if the imaging capabilities are degraded respect to those obtained by using CDGPS (compare Figure 31a,b as well as Figure 32a,b). Indeed, in Figures 31a and 32a the air–soil interface does not appear flat and the errors on the localization of the targets are larger. These degradations are more visible in Figure 31a than in Figure 32a, i.e., for Track 1.

**Table 6.** Signal Processing Parameters: Track 1

Parameters	Specification
Time Gating	Start Time: 16 (ns) End Time: 39 (ns)
Frequency range	$f_{min} = 3.1$ (GHz) $f_{max} = 4.8$ (GHz)
Frequency step	25 (MHz)
Imaging Domain	x-axis size: 27.32 (m) dx: 0.025 (m) z-axis size: 4.37 (m) dz: 0.025 (m)
TSVD threshold (T)	-15 (dB)
Subdomain Aperture (L)	4 (m)

**Table 7.** Signal Processing Parameters: Track 2

Parameters	Specification
Time Gating	Start Time: 25 (ns) End Time 47 (ns)
Frequency range	$f_{min} = 3.1$ (GHz) $f_{max} = 4.8$ (GHz)
Frequency step	35 (MHz)
Imaging Domain	x-axis size: 33.76 (m) dx: 0.025 (m) z-axis size: 3.10 (m) dz: 0.025 (m)
TSVD threshold (T)	-12 (dB)
Subdomain Aperture (L)	4 (m)

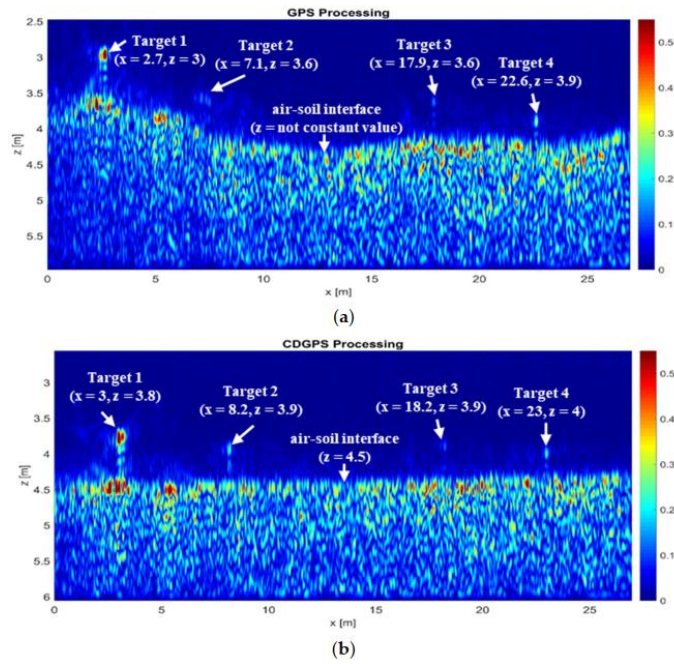


**Figure 31.** Tomographic images for the Track 1 obtained by Shift and Zoom TSVD algorithm: (a) GPS based MoCo; (b) CDGPS based MoCo.

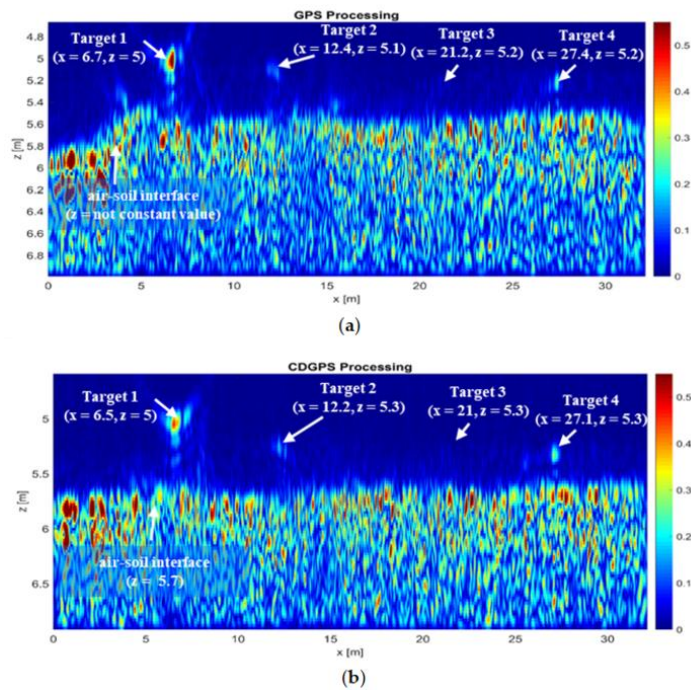


**Figure 32.** Tomographic images of Track 2 obtained by Shift and Zoom TSVD algorithm: (a) GPS based MoCo; (b) CDGPS based MoCo.

### 6.2.1.3 Discussion

The presented results represent a limited number of cases that allow at corroborating some general observations about the reconstruction capabilities of the imaging strategy performed in sounder modality. A first obvious remark is that targets are detectable if their backscattered signals collected by the radar are distinguishable from clutter and noise. Hence, whatever UAV positioning technology is adopted, the correct number of targets is expected to be identified in the tomographic image even if, depending on their radar cross section, some targets are more clearly visible than other ones. The second observation is that, as expected, in general the CDGPS positioning data allow better imaging capabilities than standalone GPS data and they made possible to estimate the horizontal distance occurring between targets as well as the target elevation from the ground with a reduced amount of error. This happens even if the achieved CDGPS accuracy was not the same for all the considered examples as it is confirmed by Table 8. This latter reports the percentage of fix/float solution, the number of visible satellites, the average values of Geometric Dilution Of Precision (GDOP), Positional DOP (PDOP), Horizontal DOP (HDOP) Vertical DOP (VDOP), and the mean East, North, and Up Standard Deviations. In other words, even in float mode (estimated positioning uncertainty of several centimeters), CDGPS is shown to effectively support radar imaging.

**Table 8.** CDGPS operative conditions.

	Test 1-Track 1	Test 1-Track 2	Test 2-Track 1	Test 2-Track 2
<b>Percentage of fix/float solution</b>	36% fix, 64% float	70%fix, 30%float	100% fix	51.3%fix, 48.7% float
<b>Number of visible satellites</b>	9	9	10	11
<b>Average values of GDOP; PDOP; HDOP; VDOP</b>	1.6; 1.5; 0.9; 1.2	1.6;1.5; 0.9; 1.2	1.9; 1.7; 0.9; 1.4	1.4; 1.3; 0.7; 1.1
<b>Mean of East Standard Deviation (m)</b>	0.0429	0.0155	0.0056	0.0101
<b>Mean of North Standard Deviation (m)</b>	0.0446	0.0176	0.0072	0.0141
<b>Mean of Up Standard Deviation (m)</b>	0.0927	0.0351	0.0212	0.0228

On the other hand, it is sometime possible that GPS-based motion compensation provides acceptable radar imaging performance and this happens when space-time correlation of positioning errors is significant. Specifically, the imaging degradation experienced by using GPS occurs when positioning data are affected by drifts, while biases play a less significant role. These results are explained by taking into account the relationship between data and unknowns of the imaging problem, see Equation

(4.12). The kernel of this relationship depends on the knowledge of the relative distance between the UAV radar system and the imaging domain; hence, as more precise is the knowledge of this relative distance as more accurate the imaging results are. In addition, it is worth pointing out that the imaging domain is defined according to the available positioning information. As a consequence, while a constant and unknown bias is detrimental for the absolute localization of the targets, it does not affect the imaging capabilities of the imaging strategy. The bias affecting the generic measurement point  $\mathbf{r}_m$  occurs also in definition of the generic point  $\mathbf{r}$  of the investigated domain and thus it is erased by computing their distance. This consideration may be important in view of imaging scenarios where CDGPS cannot be used or cannot provide nominal performance levels.

The final remark is about the computational time. As said in the Chapter 3, the MoCo allows the use of the same scattering operator for the Zoom and Shift implementation of the TSVD based inversion strategy. Therefore, the SVD computation is performed in one single shot and it is used for all the subdomains. The computational time required to obtain the tomographic images are given in Table 9 and are referred to the use of a modern laptop whose main hardware and software characteristics are:

- Processor: Intel® Core™ i7- 4510U CPU @ 2.00 (GHz)–2.60 (GHz);
- RAM: 8.00 (GB);
- Operative System: Windows 10 Pro.

**Table 9.** Computational time

Flight Test Case	TRACK	Computational Time [s]
Test 1	Track 1	5.16
	Track 2	14.15
Test 2	Track 1	4.65
	Track 2	3.27

The computational time is in the order of few unit seconds for Test 1-Track 1 and for both tracks of Test 2, i.e., when the average altitudes are in the range of [4.5–5.6] m. Conversely, for Test 1-Track 2, the computational time is about 14 s. This is compliant with the average altitude, which increases up to 10 m. As highlighted before, the higher altitude implies that the Shift and Zoom synthetic aperture adopted for Test 1-Track 2 is larger than those used for the other tracks. This analysis corroborates that, thanks to the MoCo, the required computational time is compliant with that expected

for quasi real-time imaging. In addition, with respect to other classical data inversion strategies, exploiting the positioning information directly in the focusing stage (see [11, 12, 34]), the MoCo supports the creation of an off line library of scattering operator and their SVD. This feature is useful especially in view of a real-time automatic on board processing for long flight surveys.

**6.2.2 Vertical imaging performance: the case of multiple tracks**

System HII was tested in optimal weather conditions at Archaeological Park of Paestum and Velia. The measurement campaign was carried out on July 21, 2020, over the portion of the ruins of the ancient thermal baths in Paestum, over an area of hundred square meters. A photograph of the area under test is shown in Figure 33. Data were collected in autonomous flight mode with a nominal flight velocity of 0.5 m/s, by planning a flight grid of 11 parallel lines 1 m evenly spaced along the West–East direction and 15 m long along the South–North direction and with a nominal flight height of 9 m from the ground plane. The aim of the campaign was testing the MIA procedure described in Chapter 5, Section 5.3. Therefore, according to the scenario of Figure 15, the West–East direction is referred to as x-axis and the South–North direction as y-axis. The raw data collected by the radar during the whole flight are depicted in Figure 34, where horizontal and vertical axes are the number of scans (i.e., the number of radar waveforms collected during the all flight) and the range distances from the radar antennas, respectively. Figure 34 shows that radar data are affected by direct coupling between TX and RX antennas in the first 3 m along the range direction.



**Figure 33.** Map of the investigated area. Base layer: Google Earth and picture of the area.

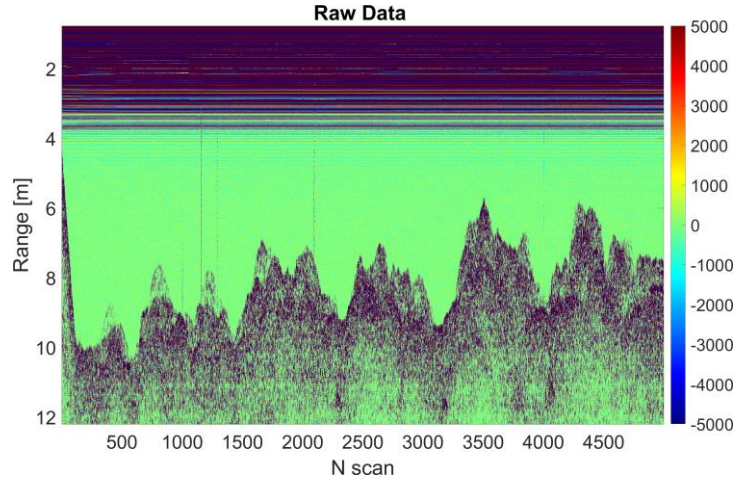


**Figure 34.** Raw radargram for the overall flight.

First of all, MIA selects the radar data associated with the 11 flight segments, depicted as red lines in Figure 35 and set the whole inspected volume  $V$  as the parallelepiped having size 17 m along the  $x$ -axis, 15 m along the  $y$ -axis, and 4 m along the  $z$ -axis. Hence,  $V$  has the extension of  $200\lambda_0 \times 226\lambda_0 \times 53\lambda_0$ , where  $\lambda_0$  is the free space wavelength at the radar carrier frequency ( $\lambda_0 = 0.075$  m). The volume  $V$  is partitioned into  $M = 35$  vertical domains  $D_i$ , with uniform spacing  $\Delta x = 0.5$  m along  $x$ -axis. The spacing  $\Delta x$  has been set according to the cross-track resolution limit, see (5.12), as  $\Delta x \leq (\delta x/2) = 0.58$  m, where the minimum estimated flight height  $h = 7.6$  m was considered. The MIA implementation parameters are summarized in Table 10. It is worth pointing out that the measurement lines are not exactly straight and their spacing is not constant. According to the subset selection process defined in (5.13), the reference coordinate  $x_k$  is taken as the average value of the  $x$ -coordinates of the measurement points belonging to the same line. The threshold  $T1$  is chosen equal to the spatial spacing  $\Delta x$  among the vertical domain  $D_i$ , while the threshold  $T2$  is fixed at 1.7 m that corresponds to the average spacing of the 11 flight segments along the  $x$ -axis. Based on Figure 34, the entire raw-radargram is filtered by means of a time gating procedure, which selects the data in the range window from 4 to 11 m; such a time window contains the radar signal associated with the structures in the investigated area. MIA exploits the positioning information provided by the CDGPS techniques and associated with the subset measurements lines  $\hat{\Gamma}_k = \sum_{k=1}^{\tilde{K}} \Gamma_k$  to define the coordinates of the measurement points  $\hat{\mathbf{r}}_m$ , which are used to compute the scattering operator  $\mathbf{L}$  as given by (4.7). Finally, the tomographic image  $\tilde{\chi}$  is performed

by means of the TSVD regularization procedure for each imaging domain  $D_i$ , which is discretized in square pixels with 0.05 m size.

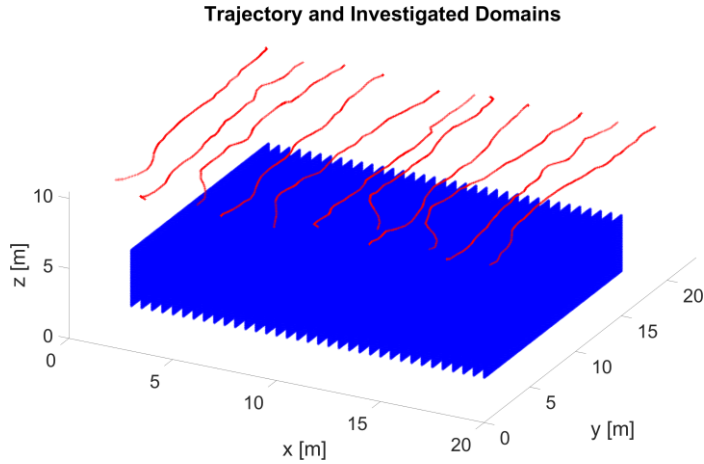


**Figure 35.** Multilines trajectories  $\Gamma_k$  (red) and investigated domains  $D_i$  (blue).

**Table 10.** MIA implementation parameters.

Parameters	Value
Number of Measurement Lines (K)	11
Number of 2 D imaging Domain (M)	35
Imaging Domain spacing ( $\Delta x$ )	0.5 m
Threshold $T_1$	0.5 m
Threshold $T_2$	1.7 m
Time gating range window	4 - 11 m
Imaging pixel size	0.05 m

The tomographic images referred to all the vertical domains  $D_i$  have been arranged in a 3-D matrix of  $35 \times 300 \times 80$  elements, representing the number of pixels along x-, y-, and z-directions, respectively. To provide a more accurate 3-D visualization of the inspected volume, the 3-D matrix has been interpolated in a denser 3-D matrix of  $700 \times 600 \times 160$  elements. Figure 20 shows 2-D slices at constant height values  $z = 3.29, 2.58,$  and  $1.37$  m, which are particularly relevant for our analysis. Based on Figure 36 and taking into account only those pixels where the amplitude of the reconstructed contrast function, as normalized to its maximum values into the volume, is higher than 0.1, one can appreciate where the structures are localized. In addition, one gains information about their geometrical shape and spatial size in the xy plane (or, equivalently, in the East–North plane) and even about their elevation. Specifically, left of Figure 36 shows two structures, the first one ranging in the intervals  $x = [1 - 9]$  m and  $y = [7 - 13]$  m, and the second one located at  $x = [12 - 17]$  m and  $y = [5 - 13]$  m. The centre of Figure 36 shows a unique structure having a complicated shape and ranging in the intervals:  $x = [1 - 17]$  m and  $y = [5 - 16]$  m. The right of Figure 36 shows the air–ground interface. In this latter case, low amplitude

pixels appear where the ruins are located. Moreover, one can infer that there are less extent ruins whose elevation is about 2 m and ruins a few higher than 1 m, whose spatial distribution is compliant with the perimeter walls. Slices in Figure 36 have been binarized and overlapped to the Google Earth image (see Figure 37). The binary images were achieved by forcing to 1 the pixels whose intensity is higher than 0.1 and to 0 the other ones. Figure 37 corroborates the quality of the radar imaging results. It shows, indeed, that both the higher parts and the perimeter structures of the ancient thermal bath of the forum are properly localized and their shape and size are consistent with the actual ones. Figure 38 shows the tomographic reconstruction of y-slice at  $y = 11$  m.

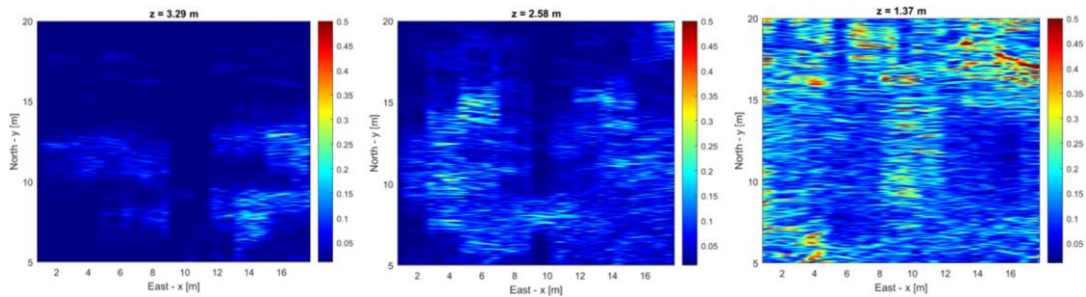


**Figure 36.** Tomographic reconstruction of the investigated volume  $V$  at constant  $z$ -slice: (Left)  $z = 3.29$  m, (Center)  $z = 2.58$  m, and (Right)  $z = 1.37$  m.

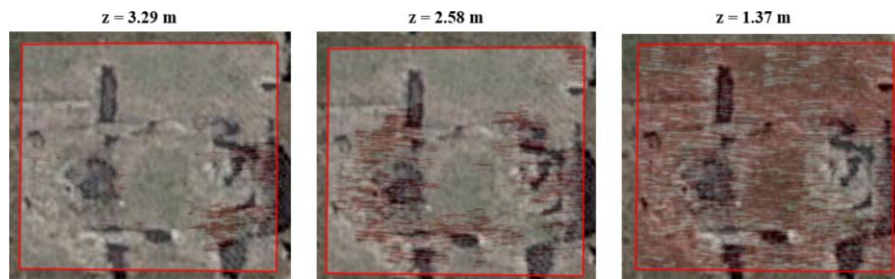


**Figure 37.** Binary tomographic reconstruction of the investigated volume  $V$  at constant  $z$ -slice overlapped with Google Earth image: (Left)  $z = 3.29$  m, (Center)  $z = 2.58$  m, and (Right)  $z = 1.37$  m.

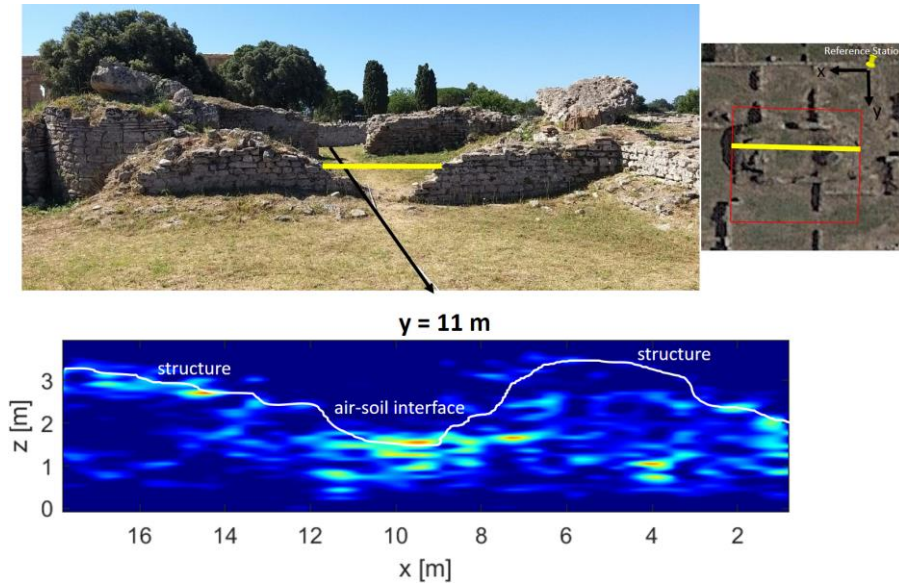


**Figure 38.** Tomographic reconstruction of the investigated volume  $V$  at constant  $y$ -slice:  $y=11\text{ m}$ .

The obtained results show that the B imaging strategy (i.e. MIA) allows to process data collected by a down-looking radar system mounted on a mini-UAV and moved along multiple lines approximately parallel to the air-ground interface and roughly located at the same height from it.

### 6.2.3 Horizontal imaging performance

#### 6.2.3.1 Analytical Study

The resolution analysis presented in this section aims at investigating the effect of the measurement parameters on the resolution limits in a horizontal image plane  $D$  (Figure 39). The PSF Equation (4.17) is here used to this aim.

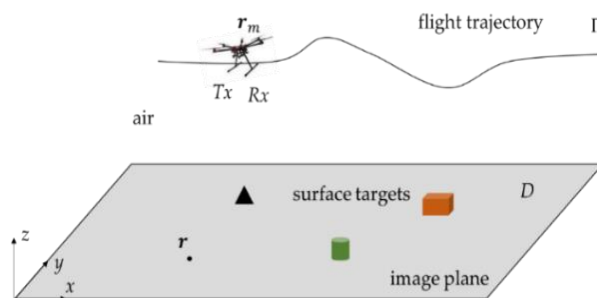


**Figure 39.** Single measurement line and horizontal imaging plane scenario.

The conclusions regarding the effect of flight parameters on the tomographic reconstruction of the PSF computed as in equation (4.17) find confirmation in the formulas of the resolutions limits holding for an imaging in the horizontal plane from

an ideal rectilinear flight path [43]. Therefore, before proceeding further, it is worth recalling these resolution formulas. Figure 40 shows the UAV moving at a fixed height  $h$  following a rectilinear trajectory directed along the x-axis. The along-track resolution  $\Delta x$  is determined by the central frequency  $f_c$  of the radar and the maximum view angle  $\theta$  fixed by half-length of the synthetic aperture:

$$\Delta x = \frac{c_0}{4f_c \sin\theta} \quad (6.1)$$

that in the small angle approximation rewrites as [67]:

$$\Delta x = \frac{c_0}{4f_c \theta} \quad (6.2)$$

The range resolution is related to the radar system bandwidth  $B$  by the classical formula [68]:

$$\Delta r = \frac{c_0}{2B} \quad (6.3)$$

The across-track resolution  $\Delta y$  is evaluated from the projection of the 3D target reconstruction over the image plane (see Figure 40b). If  $r$  denotes the target range with respect to the antenna, then the 3D target reconstruction is the cylindrical shell having its axis coincident with the measurement line and its inner and outer radius equal to  $r - \Delta r$  and  $r + \Delta r$ , respectively. Note that only a part of the shell is shown in Figure 40b, for sake of clarity. The across-track resolution  $\Delta y$  is calculated as the intersection of the cylindrical shell with the image plane  $z = 0$  and is given by:

$$\Delta y = \sqrt{d^2 + \Delta r^2 + 2\Delta r\sqrt{h^2 + d^2}} - d \quad (6.4)$$

where  $d$  is the across-track distance between the flight trajectory and the target (see Figure 40a,b).

According to Equation (6.4), the across-track resolution gets worse when the UAV flies at a higher altitude  $h$  and, when the target is illuminated at nadir ( $d = 0$ ), it turns out that:

$$\Delta y = \Delta r \sqrt{1 + \frac{2h}{\Delta r}} \quad (6.5)$$

i.e., the across-track resolution is finite and larger than the range resolution  $\Delta r$ .

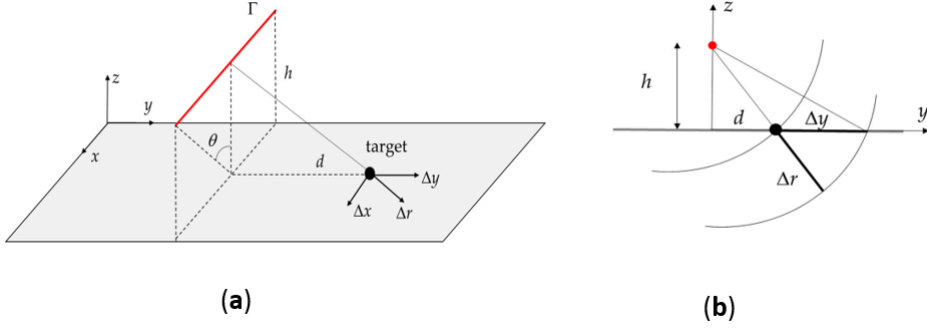


**Figure 40.** Radar imaging with an ideal rectilinear flight path: (a) 3D view; (b) view in the  $y$ - $z$  plane.

Equation (6.5) also reveals that, for a fixed value of  $h$  and  $\Delta r$ ,  $\Delta y$  improves as long as the target moves away from the measurement line. Most notably, the asymptotic value of the across-track resolution is found as  $d$  approaches to infinity:

$$\Delta y = \lim_{d \rightarrow \infty} \sqrt{d^2 + \Delta r^2 + 2\Delta r \sqrt{h^2 + d^2}} - d = \Delta r \quad (6.6)$$

Based on the results in the Equations (6.5) and (6.6), the following inequality hold:

$$\Delta r \leq \Delta y \leq \Delta r \sqrt{1 + \frac{2h}{\Delta r}} \quad (6.7)$$

Please note that if the system bandwidth  $B$  goes to zero, the range resolution  $\Delta r$  becomes infinite and it is no longer possible to resolve targets along the direction perpendicular to the track, as already stated in [61].

Figure 41 depicts the across-track resolution  $\Delta y$  as a function of the target offset  $d$  and the flight altitude  $h$ . The contour plot has been produced by applying equation (6.4) and considering a bandwidth value of  $B = 1.7 \text{ GHz}$ , which could be a typical value of UAV-based high frequency radar systems.

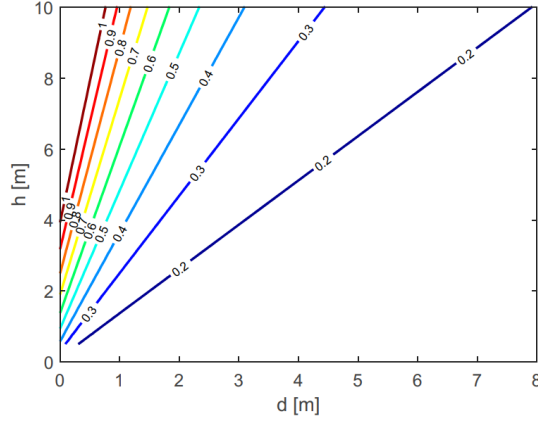


**Figure 41.** Contour plot of the across-track resolution  $\Delta y$  versus  $d$  and  $h$ , expressed in meters, in the case of a rectilinear flight trajectory

As previously pointed out, the resolution degrades when increasing the flight altitude  $h$  for a fixed value of  $d$  or when reducing  $d$  for a fixed value of  $h$ .

Figure 42 provides an example of the PSF computed according to Equation (4.17) by considering an investigation domain  $D = [-3, 3] \times [-3, 3]m^2$ , which is discretized by square image pixels with size 0.01 m, and two different values of the target offset  $d$  (i.e.,  $d = 0 m$  and  $d = 2 m$ ). The scattered field data are sampled evenly with 0.01 m step along the trajectory  $\Gamma$  at a flight altitude  $h = 5 m$ . Figure 42a,b reports the PSF reconstruction for the case of a rectilinear trajectory covering the interval  $[-3, 3]$  along  $x$ . Figure 42c,f considers the effect of a non-rectilinear UAV flight trajectory; specifically, the  $x$ -directed rectilinear trajectory of Figure 42a,b is perturbed in the  $x - y$  plane and modified in accordance with the co-sinusoidal function

$$y = \pm 0.15 \cos\left(\frac{\pi x}{12}\right) \quad (6.8)$$

Equation (6.8) defines a curved trajectory over the interval  $[-3, 3]$  m with a maximum deviation of 0.15 m along  $y$  with respect to the rectilinear trajectory.

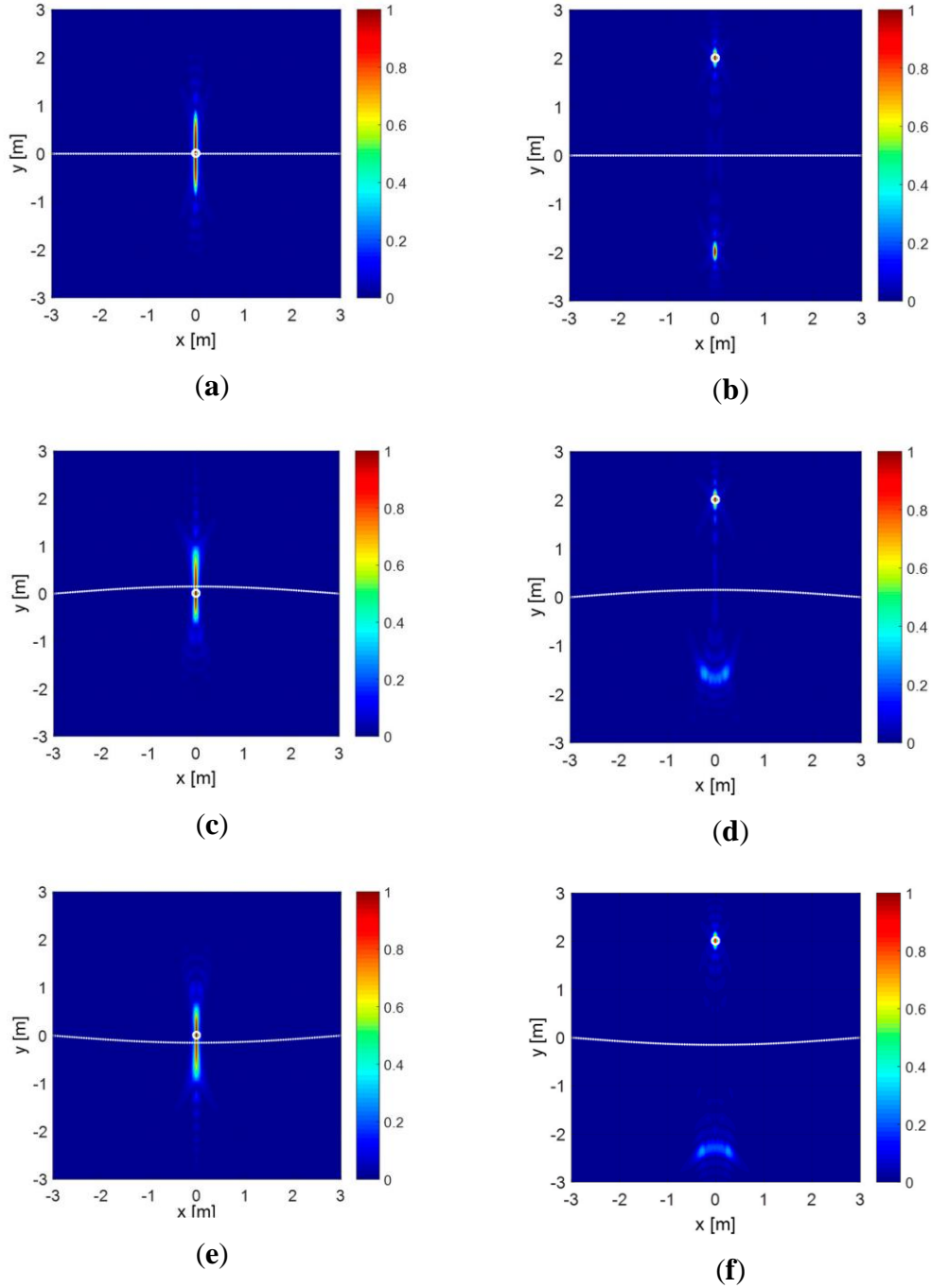


**Figure 42.** Point spread function (PSF) amplitude for a flight altitude  $h = 5$  m: ideal rectilinear trajectory and point like target with offset: **(a)**  $d = 0$  m, **(b)**  $d = 2$  m. Curved trajectory as described by Equation (4.10) and point-like target located with offset: **(c, e)**  $d = 0$  m, **(d, f)**  $d = 2$  m. The white dashed line represents the trajectory and the white circle denotes the target.

Figure 42a,b shows that a focused spot along and across the track is obtained in correspondence of the target position and the along-track resolution does not change when the target is located at the radar nadir ( $d = 0$  m) or at the point (0,2)m. Conversely, the across-track resolution improves when the target is far from the nadir,

as predicted by equation (6.4). However, in this latter case, a false target appears at the specular position with respect to the flight trajectory, i.e., at  $(0, -2)$  m. This phenomenon is the so-called left–right ambiguity [69] and is due to the radar’s inability to discriminate left ( $y > 0$ ) and right ( $y < 0$ ) targets located at the same distance with respect to the measurement line. In addition, Figure 42c,f shows that, as expected, even with a slight trajectory deviation with respect to the rectilinear path, the PSF is no longer symmetric with respect to the trajectory. Most notably, when the target is placed at  $(0, 2)$  m (see Figure 6d,f), the false target due to the left–right ambiguity appears distorted and with a lower intensity, with respect to Figure 42b. Indeed, when the trajectory is not rigorously rectilinear, the left and right targets are in some way discriminated by the radar because their echoes have different propagation delays at each measurement point. However, the beneficial effect provided by the trajectory curvature in mitigating the false target becomes less relevant when the flight altitude  $h$  increases, since left and right targets produce scattering signals with “more similar” propagation delays. This statement is corroborated by the images in Figure 43a,b, which are analogous to Figure 42c,d but for the altitude that is  $h = 10$  m. As expected, by increasing flight altitude, the resolution across-track degrades regardless of the position of the target and the left–right ambiguity problem turns out to be more evident. The amplitude of the false target seen in Figure 43b is, indeed, stronger compared to the one observed in Figure 42d,f.

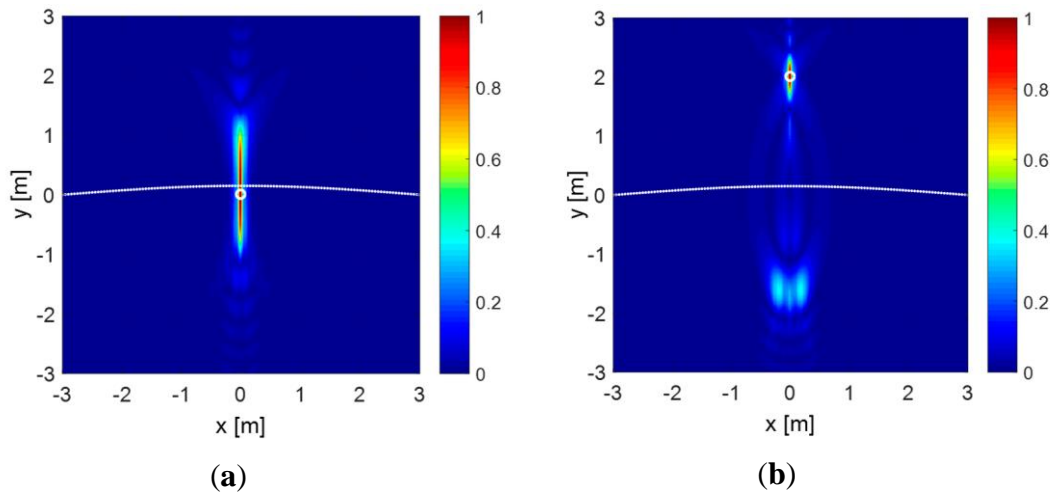


**Figure 43.** PSF amplitude for  $h = 10$  m and a curved trajectory: (a) point like target at  $d = 0$ ; (b) point like target at  $d = 2$ . The white dashed line shows the trajectory; the white circle denotes the target.

The along- and across-track resolution values referred to the considered numerical examples are summarized in Table 11.

**Table 11.** Along- and across-track resolution values.

	Along-Track Resolution (m)	Across-Track Resolution (m)
Rectilinear path, target offset $d = 0$ m, flight altitude $h = 5$ m	0.04	0.95
Rectilinear path, target offset $d = 2$ m, flight altitude $h = 5$ m	0.04	0.25
Path $y = 0.15 \cos\left(\frac{\pi x}{12}\right)$ , target offset $d = 0$ m, flight altitude $h = 5$ m	0.04	0.95
Path $y = 0.15 \cos\left(\frac{\pi x}{12}\right)$ , target offset $d = 2$ m, flight altitude $h = 5$ m	0.04	0.25
Path $y = -0.15 \cos\left(\frac{\pi x}{12}\right)$ , target offset $d = 0$ m, flight altitude $h = 5$ m	0.04	0.95
Path $y = -0.15 \cos\left(\frac{\pi x}{12}\right)$ , target offset $d = 2$ m, flight altitude $h = 5$ m	0.04	0.25
Path $y = 0.15 \cos\left(\frac{\pi x}{12}\right)$ , target offset $d = 0$ m, flight altitude $h = 10$ m	0.07	1.30
Path $y = 0.15 \cos\left(\frac{\pi x}{12}\right)$ , target offset $d = 2$ m, flight altitude $h = 10$ m	0.07	0.47

Summarizing, if the geometry is the simplest one with a single measurement line and the imaging domain is a plane at a fixed altitude, the along-track resolution is influenced by the maximum illumination angle, which in turn depends on the flight altitude and the length of the synthetic aperture. The flight height and the horizontal displacement between the target and the UAV, instead, influence the across-track resolution. Targets far from the radar nadir are generally better resolved across-track than those seen at nadir; however, an inherent limitation in the imaging arises due to the left–right ambiguity problem. This phenomenon is partially mitigated in the presence of horizontal deviations of the UAV with respect to the ideal rectilinear trajectory. Additionally, flying at a higher altitude can be convenient to enlarge the area of coverage but such choice generally produces a worsening of the spatial resolution both along- and across-track.

A further point worth to be discussed concerns the inability of the horizontal imaging configuration to provide unambiguous and high-resolution 3D target reconstructions. To clarify this point, it is useful to refer to Figure 44 showing how the reconstruction of the target changes when the image plane is not the correct one. In particular, in Figure 44, we show how a point target located on the plane  $D_0$  at  $z = 0$  is imaged on three planes  $D_0, D_1, D_2$  placed at different altitudes, i.e.,  $z = 0, z = z_1,$  and  $z = z_2$ .

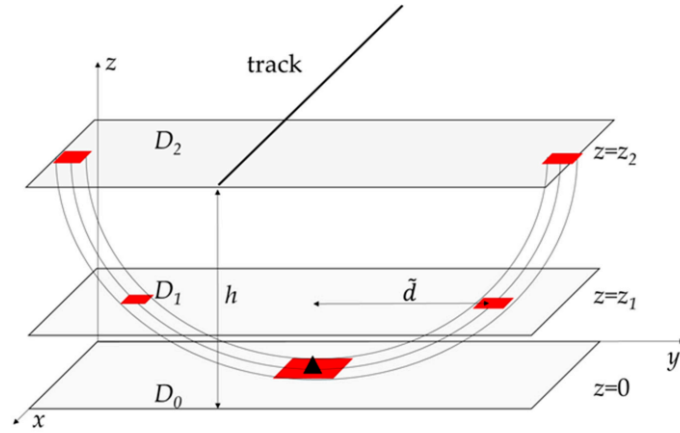


**Figure 44.** Reconstruction of a point target on image planes at different elevations. The true target (black triangle) is illuminated at the radar nadir and its reconstruction is represented by the red rectangles.

If the image plane coincides with the plane where the target is located, i.e.,  $D_0$ , then the target is reconstructed at the correct position. When the image plane is different from  $D_0$ , i.e.,  $D_1$  or  $D_2$ , due to the cylindrical symmetry of the 3D target reconstruction, the target is imaged at a position different from the true one in the considered plane. The position of the reconstructed target is equal to the intersection point between the 3D reconstruction and the plane where the imaging is carried out. Furthermore, due to the left–right ambiguity, two specular targets appear on both sides of the track (see red rectangles on planes  $D_1$  or  $D_2$ ). The spatial offset  $\tilde{d}$  in the x-y plane between the true target and the reconstructed one for an image plane at a height  $z$  can be derived after straightforward geometrical considerations and is given by:

$$\tilde{d} = \sqrt{d^2 + 2hz - z^2} - d \quad (6.9)$$

This last formula holds also in the more general case when the target is not illuminated at the radar nadir, as in Figure 44, and  $d$  is the horizontal distance between the target and the track.

The geometry in Figure 44 also reveals that the target can be detected (but not correctly localized) when the imaging plane is placed at a higher elevation with respect to the target. Indeed, in this case, it is still possible to find two intersection points between the 3D target reconstruction and the image plane. Conversely, the target cannot be identified at all when it is located above the image plane since this last no longer intersects the 3D target reconstruction.

A numerical example showing the effect of the elevation of the image plane is presented in the case of a multi-target scenario. Specifically, the example refers to the rectilinear trajectory and simulation parameters already considered before. The scene comprises three point targets T1, T2, T3 aligned along the flight track and located at coordinates:  $(-2, 0, 0) m$ ,  $(0, 0, 0.2) m$ ,  $(2, 0, 0.4) m$ . The reconstruction results achieved on three image planes at  $z = 0$ ,  $0.2$  and  $0.4 m$  are displayed in Figure 45a–c, respectively. As can be observed in Figure 45a, only the target T1 is imaged and correctly localized in the plane  $z = 0 m$  while the targets T2 and T3 are not detected because they are located above the image plane. When the image plane is fixed at  $z = 0.2 m$ , the target T2 is the only one to be correctly localized while T1 is imaged a different location with a spatial offset with respect to the true position. The target T3 is still not detectable because its elevation is greater than the height of the image plane. Finally, Figure 45c shows the reconstruction in the plane  $z = 0.4 m$ . In this case, all targets are detected but only T3 is correctly localized.

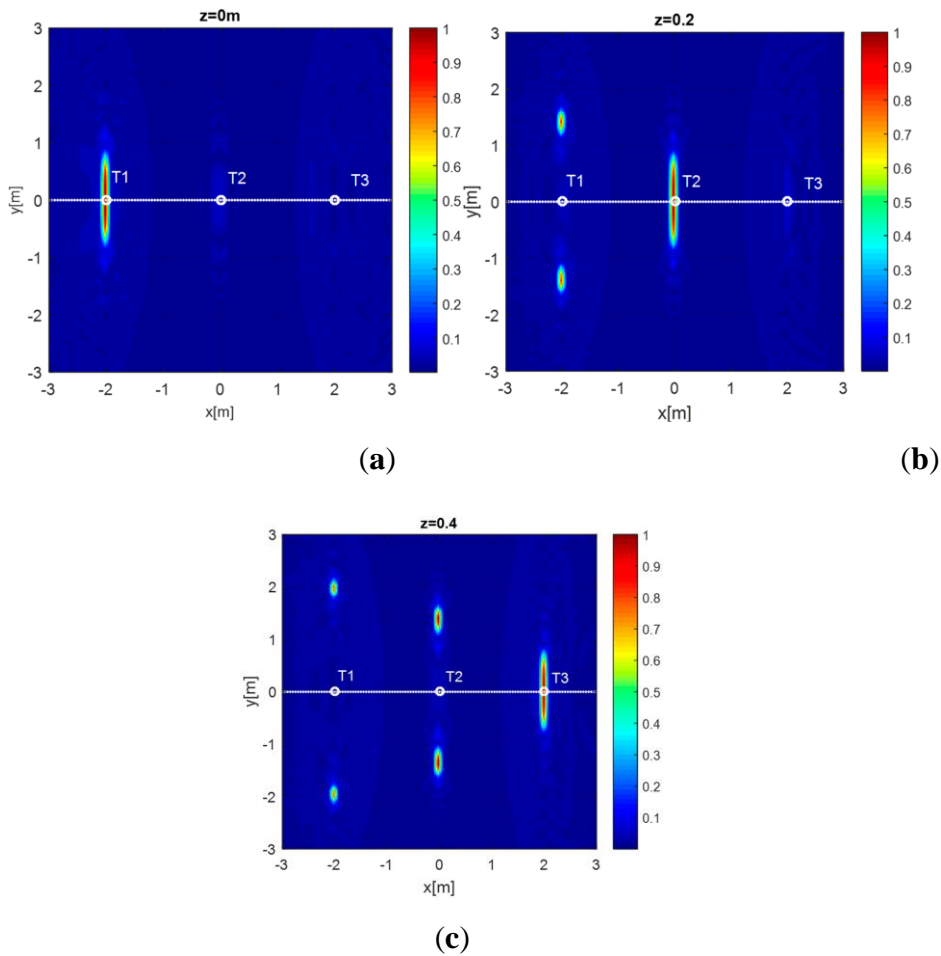


**Figure 45.** Reconstruction results in a three-target scenario (a) image plane at  $z = 0 m$ ; (b) image plane at  $z = 0.2 m$ ; (c) image plane at  $z = 0.4 m$

Table 12 reported below compares the true and reconstructed targets' positions achieved in each image plane. The maximum of each spot in the images of Figure 45a–c is considered as the estimate of the targets' positions. Note that the  $\pm$  sign appears in the presence of the left–right ambiguity problem.

**Table 12.** Estimated and true target positions for different imaging planes.

	True Target Position	Retrieved Target Positions Versus Height of Image Plane		
		z = 0 m	z = 0.2 m	z = 0.4 m
T1	(-2, 0, 0) m	(-2, 0, 0) m	(-2, $\pm 1.4$ , 0.2)	(-2, $\pm 1.99$ , 0.4) m
T2	(0, 0, 0.2) m	-	(0, 0, 0.2)	(0, $\pm 1.4$ , 0.4) m
T3	(2, 0, 0.4) m	-	-	(2, 0, 0.4) m

An improvement of the approach in terms of resolution and left-right ambiguity suppression toward high-resolution 3D imaging can be achieved by collecting wideband scattered field data along multiple (parallel) measurement tracks. A similar measurement configuration has been recently studied in the single-frequency case [61]. The theoretical and experimental assessment of such a configuration in the multi-frequency case will be subject of future research.

As a further upgrade of the radar imaging system, the possibility of using a gimbal, as suggested in [70, 71], should be considered to achieve major flexibility in the data acquisition.

### 6.2.3.2 *Experimental results*

The aim of this test was validating the processing chain introduced in Chapter 3, Section 3.3.2 (i.e. Strategy ‘B), by using as source of UAV positioning information the CDGPS technique. System HI was used to acquire data at an authorized site for amateur UAV testing flights in Acerra, Naples, Italy. The experiment was carried out during a sunny day with a weak wind state. Two metallic trihedral corner reflectors, having a size  $D = 0.40 \text{ m} \times 0.40 \text{ m} \times 0.57 \text{ m}$  and referred as Target 1 and Target 2, were used as on-ground targets placed at a relative distance of 10 m one from the other along the flight direction; one of them (i.e., Target 2) was covered with a cardboard box (see Figure 46).

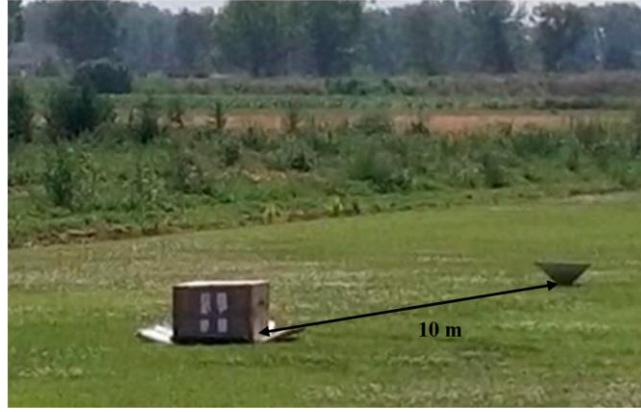


**Figure 46.** The UAV-borne radar imaging scenario.

The UAV was manually piloted and two surveys at different altitudes, in the following referred to as Track 1 and Track 2, were carried out. Both tracks were performed on the same scenario by positioning the UAV nearly at the same starting point  $(x, y)$ . Track 1 had a duration of 17.5 s and covered a path 31.4 m long at an average altitude  $h = 4$  m; along this track, data were gathered at 251 unevenly spaced measurement points. Track 2 had a duration of 21.7 s and covered a 33 m long path at an average altitude  $h = 10$  m; along this track, data were gathered at 331 unevenly spaced measurement points. The radar parameters set for the data acquisition are summarized in Table 13. Note that we considered flight altitude values in the range 5–10 m to operate with a suitable signal-to-noise ratio. Indeed, a major constraint in our system is the limited transmit power of the radar, whose maximum level is declared to be approximately  $-13$  dBm by the manufacturer.

**Table 13.** Radar system parameters.

Parameters	Specification
Carrier Frequency	3.95 GHz
Frequency Band	1.7 GHz
Maximum Emitted Power	$-13$ dBm
Maximum Dynamic Range	75 dB
Pulse Repetition Frequency	14.28 Hz
Received Signal Sampling Frequency	16 GHz

The raw radargrams, i.e., the data collected during the two surveys, are depicted in Figure 47a,b while the filtered radargrams (after the time domain pre-processing stage) are given in Figure 48a,b. It is worth pointing out that the horizontal axis shows the slow-time, i.e., the duration of the flight in seconds, while the vertical axis is the fast-time, i.e. the observation time window during which the data are gathered for each radar position, once that the time-zero correction has been

performed. The fast-time is expressed in nanoseconds. The white dotted line represents the air/soil interface achieved by converting the variable UAV flight altitude  $h$  estimated by the CDGPS into an equivalent travel time  $t_h$  by using the formula  $t_h = 2h/c_0$ . From Figures 47 and 48, one can observe that the CDGPS provides an accurate estimation of the flight altitudes and the targets' responses are visible as hyperbolas whose apex occurs at the fast-time where nadir surface reflection is observed. Moreover, Figure 47a,b shows that clutter signals, due to metallic awnings located on the entry side of the flight site, appear at fast-times greater than 70 ns in Figure 47a and 90 ns in Figure 47b. These undesired signals, as well as the mutual coupling between transmitting and receiving antennas, are removed by a time-domain pre-processing (see Figure 48a,b). The filtered radargrams have been obtained by performing the background removal and setting as fast-time gating window the portion occurring 6 ns before and 24 ns after the air–soil interface response seen at nadir. The filtered data have been transformed into the frequency domain by sampling the radar bandwidth [3.1, 4.8] GHz into 341 evenly spaced frequency samples and have been processed according to the inversion procedure described in Section 4.3.2. Before showing the focused radar images, we provide quantitative data about the positioning accuracy of the UAV. Specifically, Table 15 summarizes the maximum positioning errors achieved with the CDGPS technique along Tracks 1 and 2. These errors are the standard deviations provided by the RTKlib tool, which measure the positioning errors along the three coordinate axes based on a priori error models and error parameters [72]. The maximum errors in the horizontal plane are always smaller than the error along  $z$ , which is 9.4 cm in the worst case (Track 2).

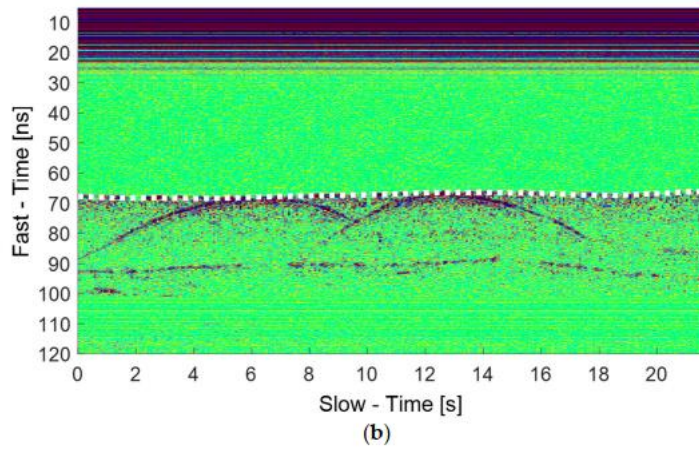
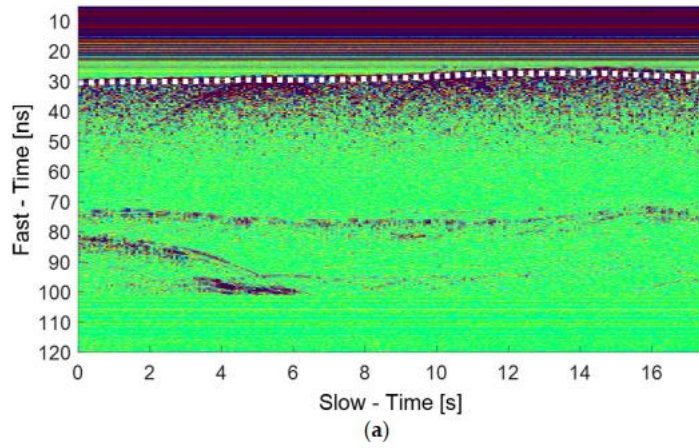


**Figure 47.** Raw radargrams. (a) Track 1; (b) Track 2. The white dotted line represents the variable UAV flight altitude  $h$  estimated by the CDGPS and transformed into the equivalent travel time by:

$$t_h = 2h/c_0.$$

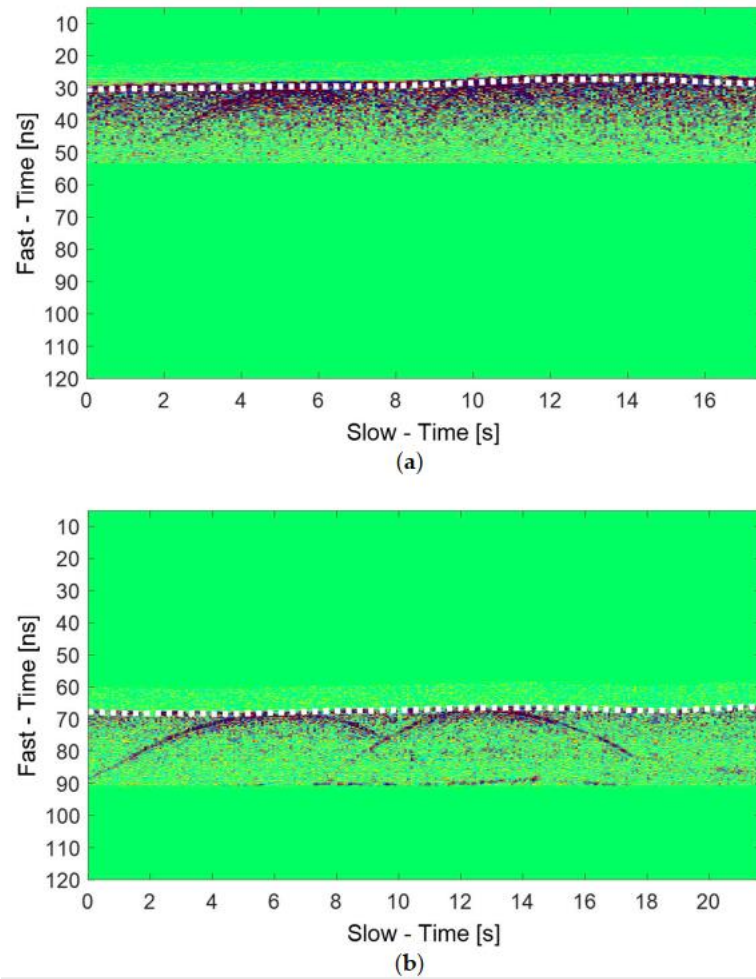
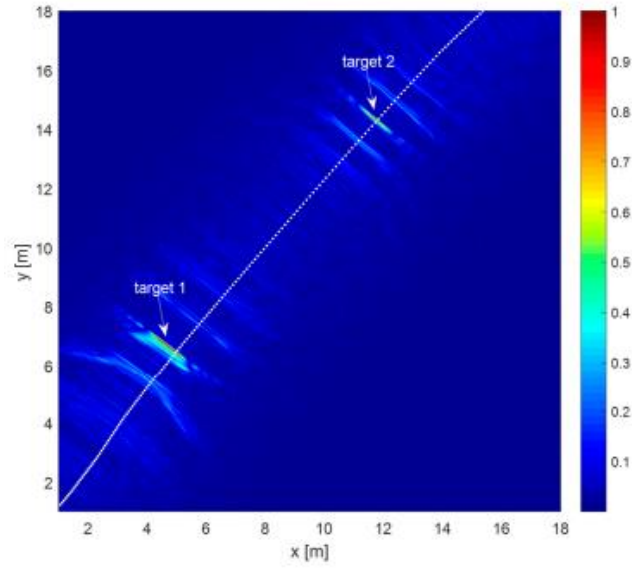


**Figure 48.** Filtered radargrams: (a) Track 1; (b) Track 2. The white dotted line represents the variable UAV flight altitude  $h$  estimated by the CDGPS and transformed in the equivalent travel time by:  $t_h = 2h/c_0$ .

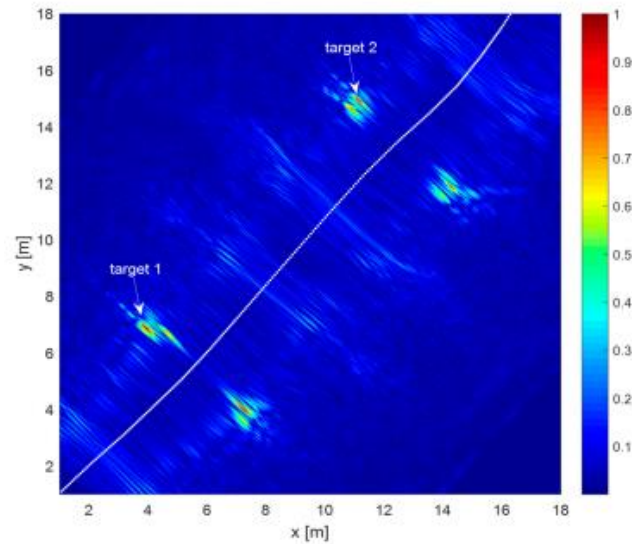
**Table 14.** Maximum errors of the CDGPS technique.

Errors (cm)	x	y	z
Track 1	4.3	4.6	9.4
Track 2	0.6	0.8	1.5

The focused images of the surveyed scenario are depicted in Figures 49a,b for Track 1 and Track2, respectively. These images have been obtained by considering a square planar investigation domain at  $z=0m$ , whose origin correspond to the starting point of the UAV tracks into the  $x$ - $y$  plane and whose side is 18cm. The domain  $D$  has been evenly discretized by pixels having size 0.01m.



(a)



(b)

**Figure 49.** Focused image of the scenario under test: (a) Track 1; (b) Track 2. The dotted white line represents the flight path as projected onto the investigated domain.

In Figure 49a,b, the dotted white line represents the M-UAV trajectory as estimated by the CDGPS and projected onto the investigated domain. According to the analysis presented in *Section 6.2.3.1*, Figure 49a shows that when the targets are illuminated at nadir, i.e., when the distance  $d$  approaches to zero, single spots appear and no ambiguities occur. Conversely, false targets due to the left–right ambiguity problem appear when the UAV flight path does not cover the targets (see Figure 49b). However, coherently with the PSFs shown in Figure 43b, the false targets appear slightly distorted and with lower intensity compared to the real target reconstructions

owing to the trajectory curvature. As a result, it is possible to discriminate the actual targets from the ambiguous ones. Table 15 reports the experimental along- and across-track resolution values as estimated by Figure 49a,b for both targets. For comparison, the table reports the theoretical resolution values referred to a rectilinear flight path at the average altitudes  $h = 4$  m and  $h = 10$  m. The experimental and theoretical resolution values are quite consistent. Notably, the experimental along-track resolution decreases slightly when the flight altitude increases and the target offset  $d$  is not null, while the across-track one improves when  $d$  increases. It is worth pointing out that the corner reflectors emphasize the radar echoes but they are not actually ideal point targets. Consequently, some discrepancies on resolution values are expected and this outcome is confirmed by the comparison between the experimental and theoretical data reported in Table 15.

**Table 15.** Along- and across-track resolution values

		<b>Experimental Along-Track Resolution (m)</b>	<b>Theoretical Along-Track Resolution (m)</b>	<b>Experimental Across-Track Resolution (m)</b>	<b>Theoretical Across-Track Resolution (m)</b>
<b>Track 1<sup>1</sup></b>	<b>Target 1</b>	0.05	0.02	1.15	0.85
	<b>Target 2</b>	0.04	0.02	0.99	0.85
<b>Track 2<sup>2</sup></b>	<b>Target 1</b>	0.07	0.03	0.51	0.41
	<b>Target 2</b>	0.09	0.03	0.50	0.41

<sup>1</sup>  $h = 4m, d = 0m$ ; <sup>2</sup>  $h = 10m, d = 2m$

# Chapter 7: Low Frequency Radar Imaging Systems by UAV

---

This chapter deals with low frequency UAV radar imaging, i.e. with the imaging of sub-surface targets, and presents experimental results. Specifically, the chapter describes two prototypes and assess their imaging capabilities. The former system, referred to as System LI, is a commercial UAV-based GPR system available at CNR-IREA and commercialized by Novatest S.r.l, Falconara Marittima, Italy (<https://www.novatest.it/>, accessed on 9 June 2022). The latter, named System LII, has been developed in the frame of the project “Discovering Bridges with Drones” financed by the Discovery Partners Institute (DPI) and lead by the University of Illinois at Chicago (UIC). The chapter is organized as follows. Section 7.1 describes the hardware components of the two systems. Section 7.2 deals with an experimental proof assessing the performance of System LI in the frame of subsurface imaging. Specifically, data acquired with System LI are processed with Strategy ‘A’ by implementing the Equivalent Permittivity (EP) Model. Section 7.3 presents calibration tests and preliminary experimental results obtained with System LII. Experimental results are compared with numerical results.

## 7.1 UAV-BASED GPR SYSTEMS

The first UAV-based GPR system (System LI) (Figure 50) is based on the commercial Cobra CBD radar module [22] and the DJI Matrice 600 Pro platform. The radar module works at the carrier frequency of 500 MHz with a bandwidth variable in the range of 50-1400 MHz. The UAV autopilot is composed of an IMU and a GNSS receiver used to manage and control the UAV flight trajectory. The drone is also equipped with a laser range finder, to enable the functionality of the terrain follow, and an additional GNSS receiver, which is connected over a wireless link to a ground base station by implementing the CDGPS technique. GPR and UAV telemetry data are integrated and synchronized via a sky-hub PC data logger. A picture of the system is shown in Figure 50. Table 16 summarizes System LI components and specifications.



**Figure 50.** System LI.

**Table 16.** System LI components and specifications.

UAV platform	DJI M600 Pro
UAV Maximum takeoff weight	15.5Kg
UAV Batteries	6 × DJI TB47S Intelligent Flight Batteries lipo 4700 mah 6s 25c-50c
UAV Max Flight time	30 minutes with 0.9 Kg payload
On-board Mini laptop	Datalogger SkyHub
Radar module	Radarteam Cobra Plug-In GPR
Radar central frequency	500 MHz
Frequency range	50-1400 MHz
Antennas	Multifrequency CBD GPR Cobra
Laser Altimeter	Lightware SF-11 with terrain following
On-board GNSS module	Emlid Reach M2
On-the-ground GNSS module	Emlid Reach RS2

The second UAV-based GPR system (System LII) is the system developed at the University of Illinois Chicago. This system is based on the commercial S5085 Vector Network Analyzer (VNA) of Copper Mountain [73] and the Aurelia X6 Standard platform [74]. Two LPDA antennas [75] are connected to the VNA, which work at 1.35-9 GHz. Positioning information are retrieved through the onboard Ublox EVK-M8T GPS module [76], while GNSS and radar data are stored and synchronized through the Beelink T4 Pro Mini PC [77]. Two equal power banks [78] are in charge of powering the mini laptop and the VNA respectively. Figure 51 shows the connections between the components, while Figure 52 shows the assembled system where the two power banks, the mini PC, the GNSS receiver and the VNA have been all put inside an ad hoc built plastic case. This system was designed with the purpose to detect rebars in concrete structures. Table 17 summarizes components and specifications of System LII.

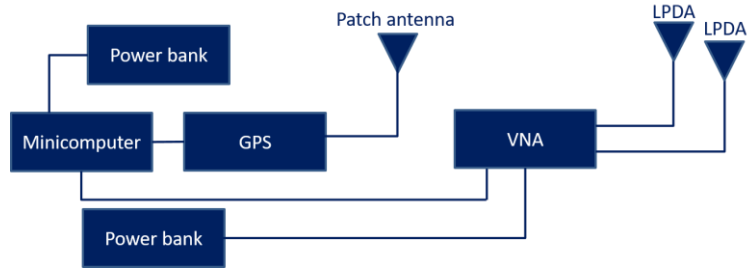


**Figure 51.** System LII. Components connection.

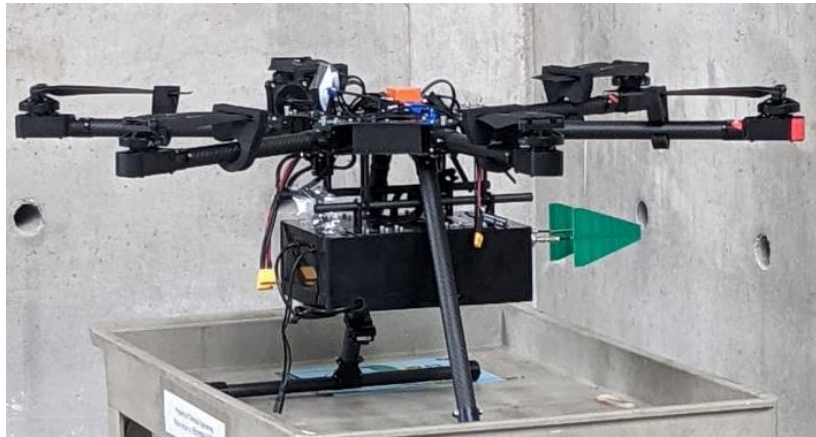


**Figure 52.** System LII.

**Table 17.** System LII components and specifications.

UAV platform	Aurelia X6 Standard
UAV Maximum take-off weight	12,170Kg
UAV Max Flight time	30 mins
Maximum payload weight	5 Kg
Battery Type	6 x Lithium Polymer (LiPo)
Battery Capacity	2x 10,000 mAh
Battery voltage	22.2V
Vector Network Analyzer (VNA)	S5085 of Copper Mountain
Frequency Band	1.35-9 GHz
Working frequency band	1.5-2 GHz
Working central frequency	1.75 GHz
Antennas	Two Log-periodic Directional-Antennas (LPDA)
On-board Mini PC	Beelink T4 Pro
On-board GNSS module	Ublox EVK-M8T GPS
On-the-ground GNSS module	Emlid Reach RS2
Rangefinder LIDAR Accuracy	+/- 4 cm

Rangefinder LIDAR Range	0 - 12 Meters
-------------------------	---------------

## 7.2 SUBSURFACE IMAGING WITH SYSTEM LI

An experimental test assessing the penetration capabilities of the System LI was carried out on the 12 May 2022 over an open area outside the Hydrogeosite laboratory of IMAA-CNR, located in Marsico Nuovo (Pz), a small town in Basilicata, Italy. The test deals with the detection of a metal plate having size of  $0.25 \times 0.35$  m, which was buried into the ground at a depth of 0.3 m. Figure 53a shows the aerial view of the site provided by the Zoom Earth web application [79] with the UAV flight trajectory (red line) and the superimposed target (black rectangle). Figure 53b shows a photo of the metal plate taken during the burial operation. The main radar system parameters adopted for the data acquisition are described in Table 18.



**Figure 53.** Experimental test site: (a) aerial view of the area with UAV flight trajectory (red line) and target (black rectangle) superimposed; (b) photo of the buried metal plate.

**Table 18.** Radar system parameters.

Parameters	Specification
Carrier frequency	500 MHz
Frequency band	600 MHz
Pulse repetition frequency	33 Hz

The UAV was manually piloted and a single passage was carried out over the area at a nearly constant altitude of 0.5 m. The flight lasted around 21.5 s and 450 radar traces were recorded over a 15.9 m-long track at an average speed nearly equal to 0.7 m/s. The radar data were processed by means of Strategy ‘B’ implementing the Equivalent Permittivity (EP) model as vertical imaging scheme for half-space scenario (Figure 54).

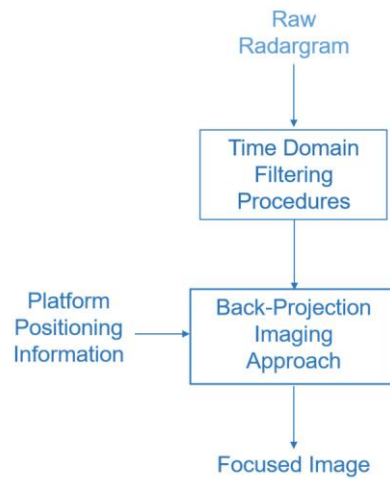


**Figure 54.** Signal processing scheme for data acquired with System LI.

The raw radargram collected by the system is depicted in Figure 55 where the horizontal axis is the trace index, while the vertical axis is the fast time. The raw radargram shows strong horizontal constant signals linked to the TX-RX antenna coupling and the reflection due to the air-soil interface. Despite this large clutter contribution, the radar also reveals the presence of some subsurface layers in the fast time window ranging from 10 ns to 25 ns. Moreover, a weakly scattering anomaly, associated with the buried metal plate, appears around the trace 140 at the fast time of 14 ns. Figure 56 shows the filtered radargram achieved after the application of the time-gating operation, which sets the signals outside the time interval 8–30 ns to zero. Now, the air–soil interface and the target anomaly are better emphasized compared to their counterparts in the raw radargram (compare Figures 55 and 56).

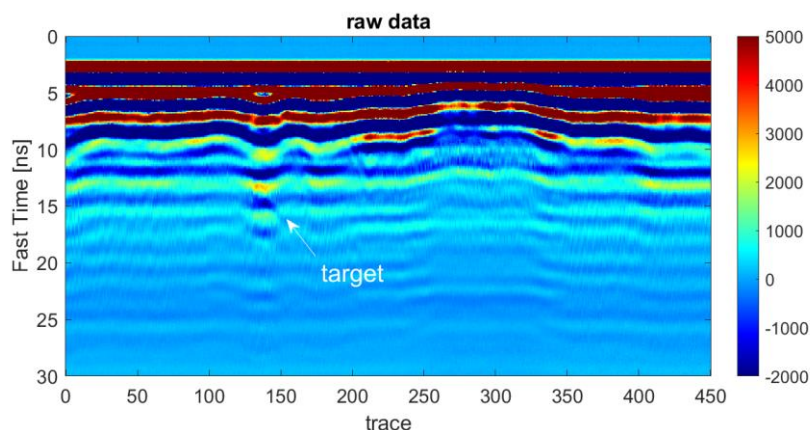


**Figure 55.** UAV GPR raw radargram.

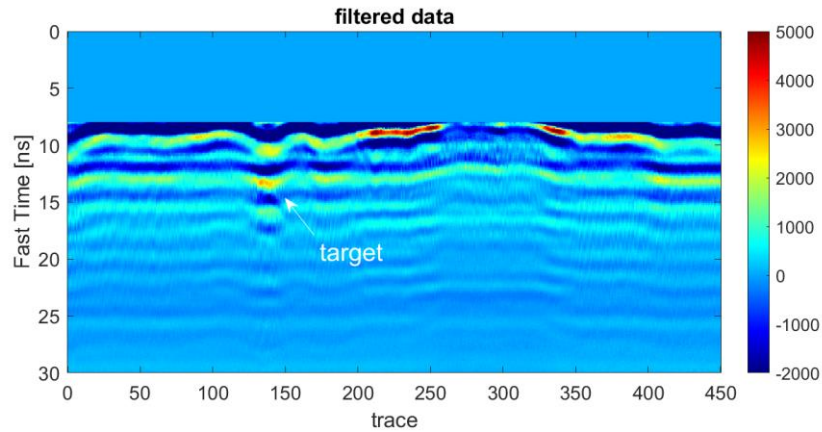


**Figure 56.** UAV GPR filtered radargram.

Figure 57 shows the focused image of the surveyed area. All the parameters adopted for the radar data processing are listed in Table 19. Specifically, after setting the zero time at 2 ns, the filtered data in Figure 56 were transformed into the frequency domain and then focused via back-projection by assuming a soil relative permittivity of  $\epsilon_r = 16$ . This value is justified by the fact that the soil was wet (i.e. see material properties in [36]) due to rain that fell the day before the test. In order to reduce the computation effort related to the focusing procedure, the shift and zoom processing strategy described in Section 3.3.1 was applied by considering a synthetic aperture of 2 m. The domain under test was a rectangular domain  $D$  with size of  $13.6 \text{ m} \times 1 \text{ m}$ , whose  $x$  axis and  $z$  axis correspond to the along-track direction and depth, respectively. The domain  $D$  was evenly discretized in square pixels with size of  $0.02 \text{ m} \times 0.02 \text{ m}$ . As can be seen, the focused image depicts the shallow soil stratigraphy as well as the target, which appears to be located at a depth around 0.3 m. Despite the simple proof-of-concept example, the achieved result demonstrates the potential of the considered UAV-GPR system to detect buried objects.

**Table 19.** Signal-processing parameters.

Parameters	Specification
Zero time	2 ns
Time-gating window	8–30 ns
Background relative permittivity	16
Frequency range	200–800 MHz
Frequency step	18.75 MHz

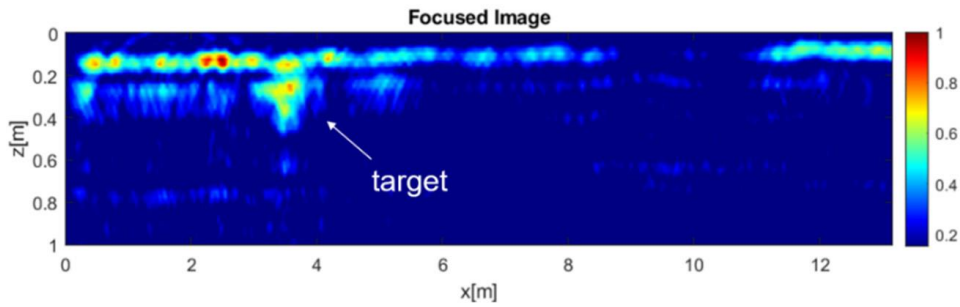


**Figure 57.** Focused image.

### 7.3 PRELIMINARY RESULTS WITH SYSTEM LII

This section shows the VNA calibration procedure and the preliminary experimental results obtained with System LII.

#### 7.3.1 VNA Calibration

The first step performed to set up the System LII consisted into a calibration procedure for the VNA. Table 20 shows VNA parameters for calibration. Specifically, the VNA was positioned in front of a target with a rectangular cross-section (Figure 58). Three different VNA-target distances were considered: 48 cm, 88 cm and 128 cm. Therefore, three static tests were carried out with the aim of certifying the capability of the system of detecting and representing the target at the actual distance in the radargram. Since an anechoic chamber was not available, the first step consisted into acquiring data in absence of the target in order to use the received signal as the one characterizing the scene and the antennas direct coupling. This allowed to know the antennas direct coupling range position, which appears as a peak at 58 cm in the time-domain response plot (Figure 59). Then the target was positioned at 48 cm from the VNA antennas. The A-scan is shown in Figure 60. Since the response of the target is difficult to see in Figure 60, the difference between the A-scan with target and the A-scan without target is shown in Figure 61. By plotting the difference between the A-scan with target and the A-scan without target (Figure 61) it is possible to localize the response of the target as a peak at the range 1.06 m, which corresponds to the actual VNA-target relative distance by considering the range at which antennas direct coupling appears (i.e.  $1.06 - 0.58 = 48$  cm). Figure 62 shows the radargram of the signals difference. The target is visible at 1.06 m, as shown by the bright yellowish line.

**Table 20.** VNA parameters for calibration.

Frequency Range	1500-2000 MHz
Central Frequency	1750 MHz
Free-space Wavelength	~17 cm
No. of frequency points	40
IF bandwidth	100 KHz
Power	0 dBm

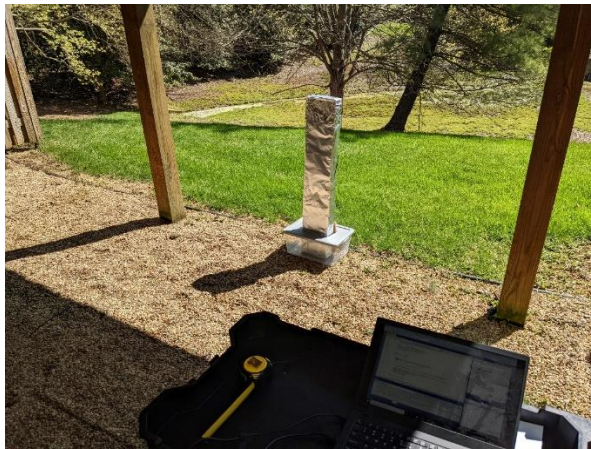


**Figure 58.** Metallic target with a rectangular cross-section.

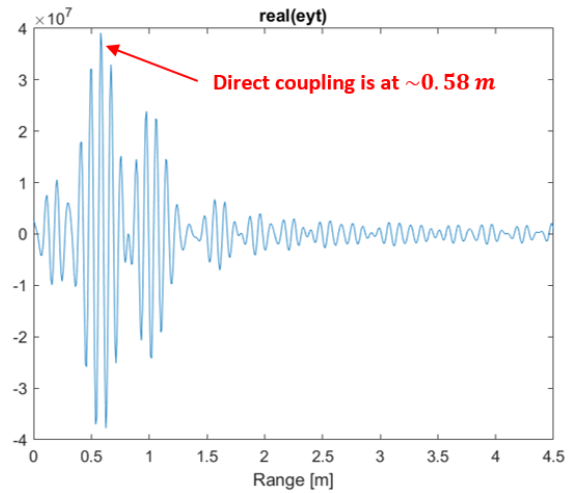


**Figure 59.** A-scan without target.

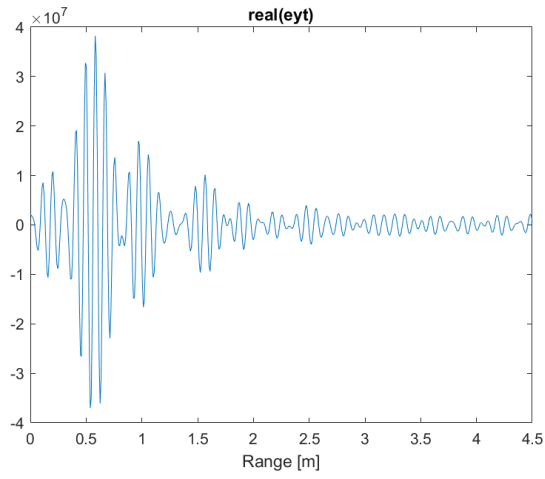


**Figure 60.** A-scan with the target.

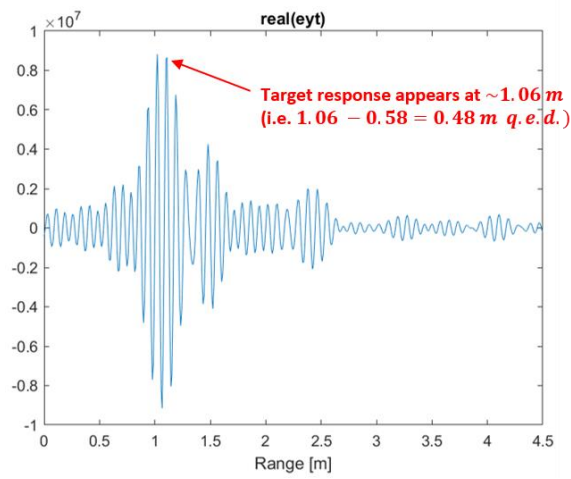


**Figure 61.** Difference between the A-scan with target and the A-scan without target.

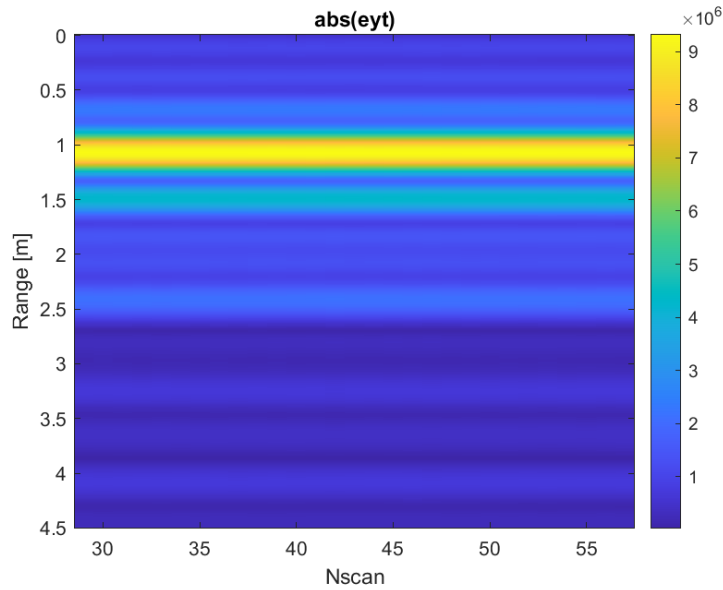


**Figure 62.** Radargram of the signal difference.

The same experiment was repeated for two additional VNA-target relative distances, i.e. 88 cm and 128 cm. In both cases, the target localization was successful (Figures 63 and 64). Figure 63a shows the target response as a peak at 1.46 m, which results in 0.88 m by subtracting the antennas direct coupling position. Figure 63b shows the radargram of the signals difference and the target as a bright yellowish line at 1.46 m. Figure 64a shows the target response as a peak at 1.86 m, which results in 1.28 m by subtracting the antennas direct coupling position. Figure 64b shows the radargram of the signals difference and the target as a bright yellowish line at 1.86 m.

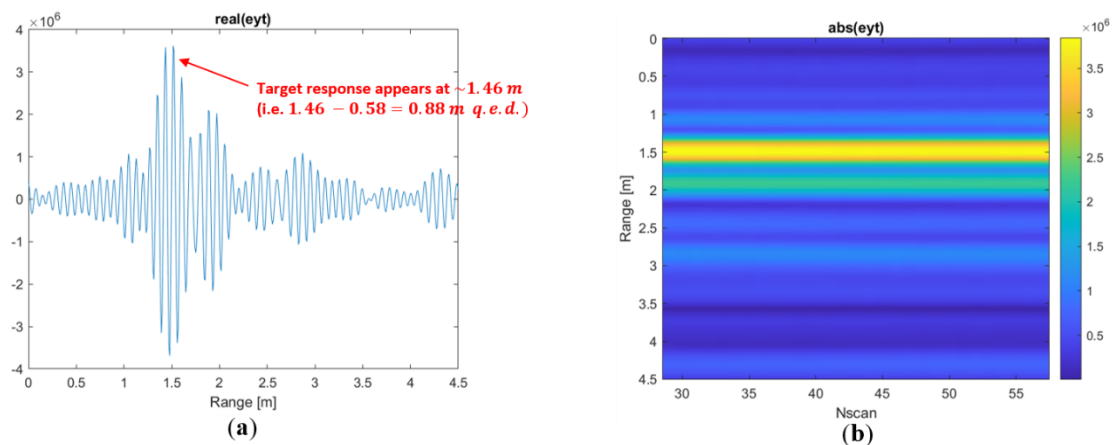


**Figure 63.** Target at 88cm: (a) Difference between the A-scan with target and the A-scan without target. (b) Radargram of the signals difference.

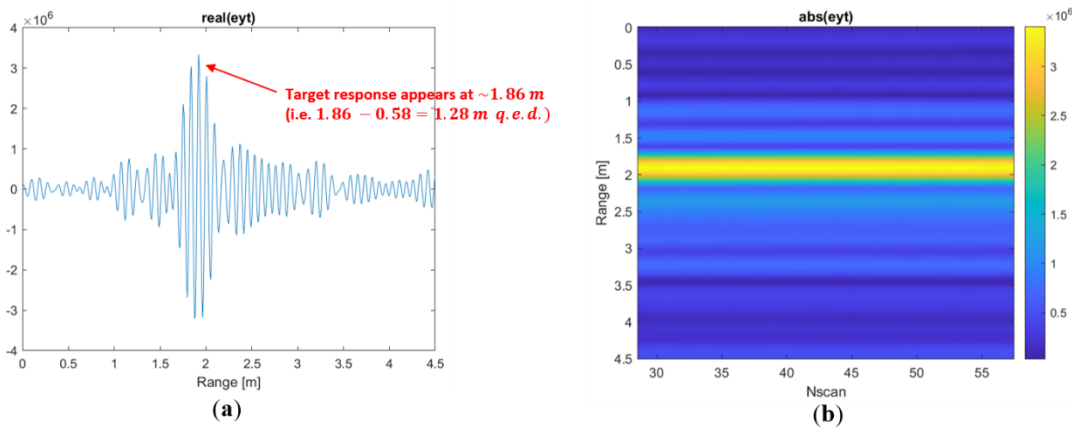


**Figure 64.** Target at 128cm: (a) Difference between the A-scan with target and the A-scan without target. (b) Radargram of the signal difference.

### 7.3.2 High Bay Lab test

After the calibration phase, the VNA was tested by inspecting a reinforced concrete wall at the High Bay Lab of University of Illinois at Chicago. Figure 65 shows the inspected wall. Figure 66 shows the sketch of an horizontal slice of the wall generated according to the available information about wall design. The inner structure of the wall is composed by horizontal and vertical rebars with 2.5 cm and 2.85 cm diameters, respectively. The wall has also holes (Figure 65) that cross it along its entire thickness, each one with a diameter of 7.5 cm and distant 62 cm from the nearest holes. Despite the inner structure of the wall is not the easiest one to investigate, this wall was the only one for which an approximate map of the inner structure was available. Therefore it was used for testing the VNA. The VNA was placed on a cart 150 cm distant from the wall and it was manually moved along the measurement line (Figure 66) with steps of 2 cm. The measurement frequency range was set to 0.9-2.4 GHz with 100 frequency points and the transmit power was set to 5 dBm. The measured results are shown in Figure 67. The response of the wall appears at a range distance of 185 cm (i.e. 150cm by considering that the direct coupling of the antennas starts at 35cm). Given the distance of the antennas from the wall, the expected hyperbolas are not clearly visible in Figure 67, and only two strong signals appear around 2m.



**Figure 65.** High Bay Lab concrete wall with buried reinforced rebar.

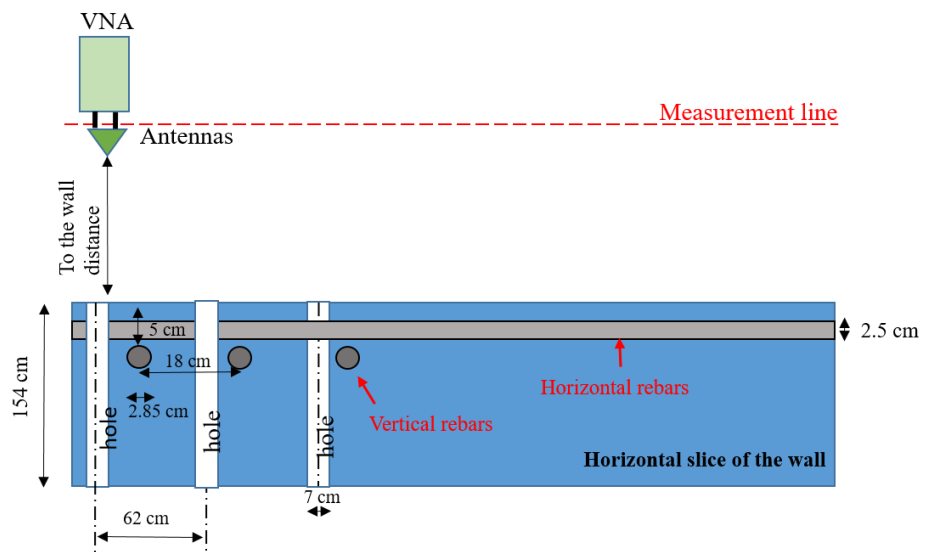


**Figure 66.** Horizontal slice of the wall.

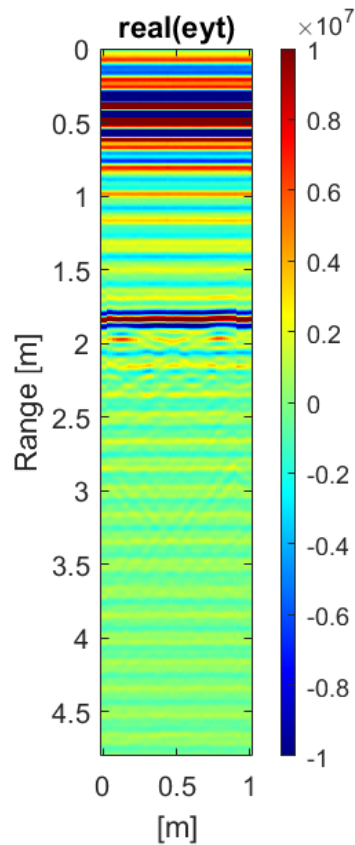


**Figure 67.** Measured results.

In order to better understand the measured results, four simulations have been run in gprMax software with the aim of understanding how the distance of the VNA antennas to the wall affects the radargram. A 2D scenario approximating the horizontal slice of the wall was considered (Figure 68), where five rebars are placed in a concrete medium with relative permittivity 6. These rebars have been modelled as PEC with the same geometrical size of the real ones and their centers are at the x coordinates of 0.70, 0.88, 1.06, 1.24, 1.42 m, respectively, and the y coordinates is 1.4757 m, i.e. 6.43 cm below air-wall interface. Antennas were modelled as a hertzian dipole source with a Ricker waveform of central frequency 1.65 GHz. Four different distances  $d$  of the VNA antennas to the wall were considered, i.e. 25 cm, 50 cm, 100cm and 150 cm.

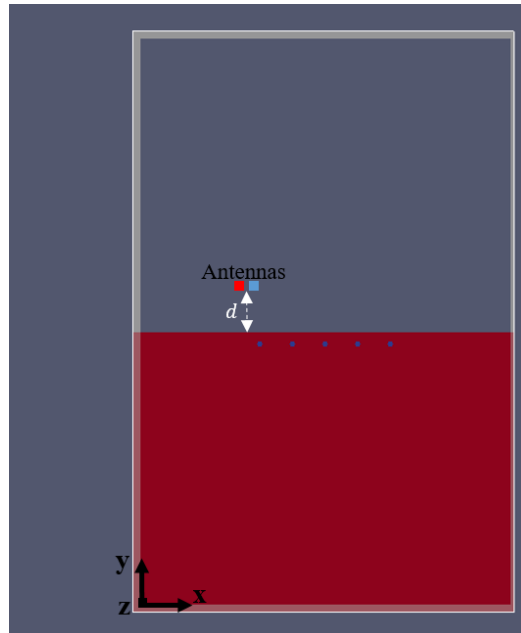


**Figure 68.** Simulated scenario.

Figure 69 shows the simulation results obtained for  $d=25\text{cm}$  (Figure 69a),  $d=50\text{cm}$  (Figure 69b),  $d=100\text{cm}$  (Figure 69c),  $d=150\text{cm}$  (Figure 69d). The range distance has been evaluated by considering the free-space wave propagation velocity. In Figure 69a the response of the wall appears at  $0.35\text{m}$  (i.e.  $0.25\text{m}$  by considering that the direct coupling of the antennas starts at  $0.1\text{m}$ ), while the five rebars correspond to the peaks of the strong continuous signal around the range  $0.47\text{m}$ . Figure 69a is the only one in which hyperbolas are clearly visible, while they become more and more flat by increasing the distance  $d$  of the antennas from the wall (Figure 69b, 69c, 69d), finally resulting as a single flat signal in Figure 69d. Simulations results suggest that distance of the antenna from the wall affects the way in which the rebars appear in the radargram.

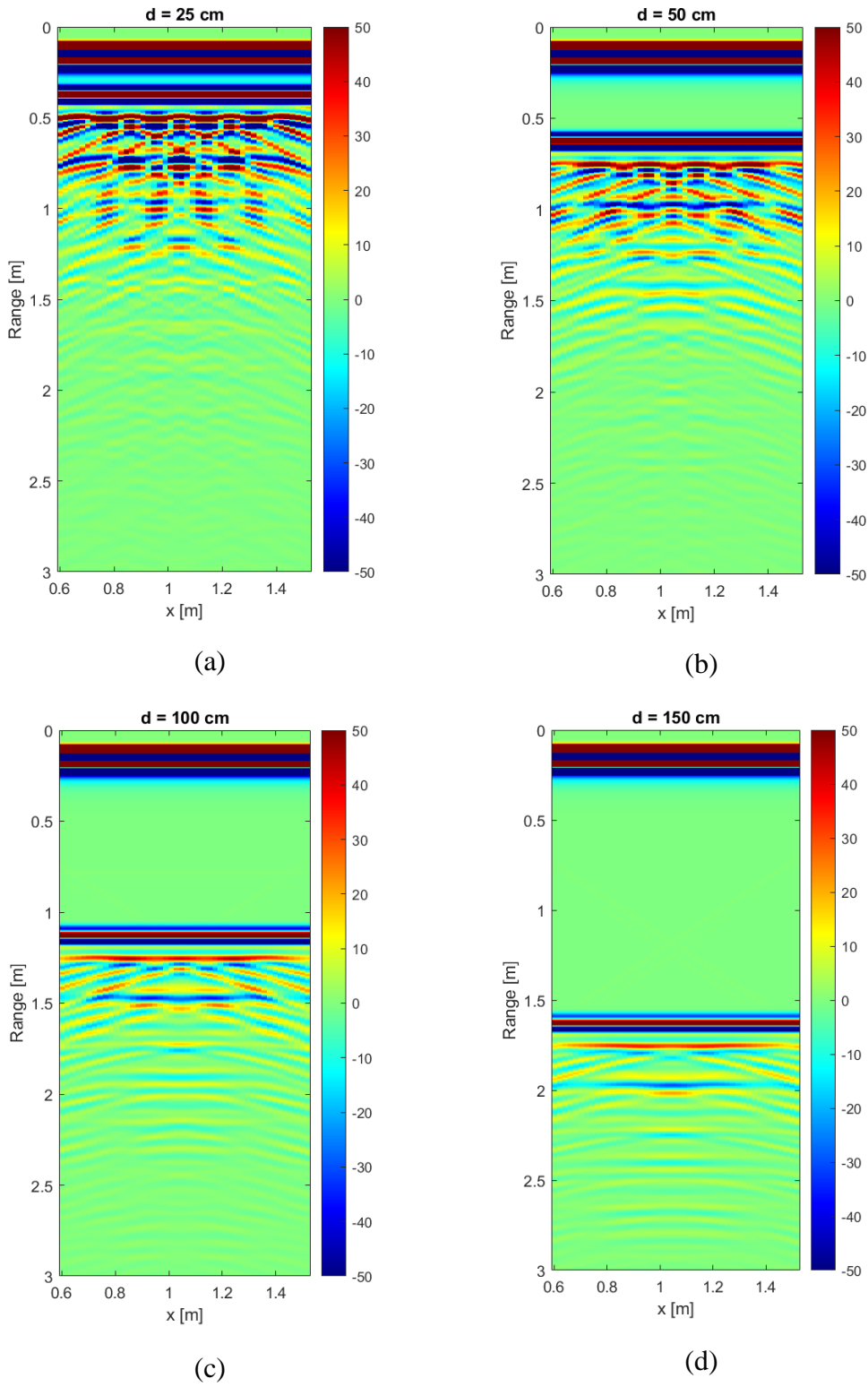


**Figure 69.** Simulation results.

## Chapter 8: Conclusions

---

This thesis dealt with mini-UAV-based radar imaging enhanced by MWT approaches. After a brief description of the state-of-the-art, this thesis addressed the main issues inherent in this type of technology, such as clutter, the need for accurate UAV flight positions estimation during radar data acquisition, and the need for obtaining high-resolution images of the observed scene with reasonable computing times and computer resources in terms of memory space and processor velocity. At this regard, this thesis proposed two different processing strategies, called Strategy ‘A’ and Strategy ‘B’ respectively, both based on the use of time domain filtering procedures and implementing microwave tomography approaches addressing the imaging as an inverse linearized problem of electromagnetic diffusion. Strategy ‘A’ and Strategy ‘B’ refer to data acquired along a single measurement line and differ in the way in which the positioning information provided by the GNSS system is exploited. These two strategies can be regarded as general tools that can be applied to face different kind of radar imaging problems since the adopted MWT approach can be modeled according to the specific imaging problem to be solved.

Specifically, Strategy ‘A’ implements the Motion Compensation and the Shift and Zoom approaches. Strategy ‘A’ allows processing data on partially overlapping intervals and combining the images in such a way to get an overall focused image, thus drastically decreasing the computational time for the overall reconstruction process.

Strategy ‘B’ exploits differential positioning information directly into the focusing step, thus avoiding any treatment of the collected data and so preventing from possible unaccuracy due to the alignment and resampling operations. In addition, Strategy ‘B’ is suitable for arbitrary flight geometries, i.e. not only for straight trajectories.

Another fundamental contribute of this thesis regarded the design of MWT approaches to face the imaging of surface or subsurface targets from radar data collected by using a mini UAV as observation platform. Specifically, the radar imaging problem was addressed in the case of two-dimensional geometry considering both the vertical imaging plane, i.e. the plane defined by the flight path and the pointing

direction of the transmitting and receiving radar antennas, and the horizontal imaging plane, i.e. the plane at constant altitude. Accordingly, after a brief review of the basic concepts regarding MWT, the approaches developed during the PhD activity have been presented in Chapter 5. These MWT approaches differ from each other for the scattering model adopted to describe signal propagation while using the same mathematical tools to solve the inverse scattering problem and allowing the exploitation of some figures of merit for analysing the achievable spatial resolution limits.

At this regard, a strategy called MIA (Multiline Imaging Approach) was also proposed. MIA considers the imaging in the vertical plane and exploits the radar data collected on one or more measurement lines to reconstruct 2D domains (slices), which are then interpolated to provide a pseudo-3D representation of the investigated volume. The computational burden of MIA is significantly reduced compared to that required by a full 3D approach.

Finally, this thesis proposed four mini UAV-based radar imaging systems for inspections of surface and subsurface scenarios. Specifically, two high frequency radar systems were presented, namely System HI and System HII, and two low frequency radar systems, System LI and System LII. These systems were used in various measurement campaigns concerning objects placed on the surface (Systems HI and HII) and buried (Systems LI and LII) and the acquired radar data were used for the experimental validation of the developed strategies and the designed MWT approaches.

Strategy ‘A’ was successfully tested on data acquired with System HI in two different locations, i.e. Acerra (Test 1) and San Nicola la Strada (Test 2). Two flight tests (Track 1 and Track 2), which differ in the flight altitude, were performed in Acerra, both flying the UAV over three targets arranged on the ground along a straight line: a cylindrical wood trunk and two metallic trihedral corner reflectors. The latter was covered with a cardboard box. Also, two flight tests (Track 1 and Track 2), which differ in the flight altitude, were performed in San Nicola la Strada (CE), both flying the UAV over four targets arranged on the ground along a straight line: a couple of chipboard shelves, a wood trunk, a void inside small box of plasterboard, and a tuff brick. Results demonstrated that targets are detectable if their backscattered signals collected by the radar are distinguishable from clutter and noise. Besides, depending

on their radar cross section, some targets are more clearly visible than other ones. In addition, experimental results allowed to establish that CDGPS positioning data allow better imaging capabilities than standalone GPS data. Indeed CDGPS positioning data made possible to estimate the horizontal distance occurring between targets as well as the target elevation from the ground with a reduced amount of error with respect to standalone GPS data (even if the achieved CDGPS accuracy was not the same for all the considered examples). On the other hand, experimental results also demonstrated that it is sometime possible that standalone GPS-based motion compensation provides acceptable radar imaging performance, and that this happens when space-time correlation of positioning errors is significant. In other words, the imaging degradation experienced by using standalone GPS occurs when positioning data are affected by drifts, while biases play a less significant role. The final remark is about the computational time. Since the MoCo allows the use of the same scattering operator for the Shift and Zoom implementation of the TSVD-based inversion strategy, then the SVD computation is performed in one single shot and it is used for all the subdomains. Computational time required to obtain the tomographic images are compliant with that expected for quasi real-time imaging.

Strategy 'B' was tested on data acquired with System HI. For this purpose, Strategy 'B' implemented a free-space propagation horizontal imaging model. Experimental results showed good reconstruction capabilities and correct localization of the targets. In addition, an analysis of the reconstruction capabilities was carried out by showing the effect of the radar parameters, of the flight altitude and of the spatial offset between targets and flight path, on the resolution limits. The consistency of these results with the theoretical resolution limits was confirmed. At this regard, it was shown that cross-track resolution improves when targets are observed in off-nadir, and that slightly curved trajectories can help to mitigate the left-right ambiguity occurring for targets observed in off-nadir.

Strategy 'B' was also tested on data acquired with System LI. For this purpose Strategy 'B' adopted the Equivalent Permittivity (EP) model for vertical imaging in non-homogeneous media. Specifically, the EP model was adapted to the case of a two-layered scenario where the upper half-space is air and the lower half-space is soil. Results demonstrated the capability of the system to correctly localize a metal plate having size of  $0.25 \times 0.35$  m, which was buried into the ground at a depth of 0.3 m.

MIA was tested on data acquired with System HII and results demonstrated good target focalization and localization capabilities. The processing of radar data through the MIA strategy confirmed the computational advantage of the proposed strategy.

Finally, System LII was tested in no-fly conditions in order to assess the performance of the on-board radar payload, i.e. the VNA. The VNA calibration was done by looking at a target with a rectangular cross-section and by considering three different VNA-target distances (i.e. 48 cm, 88 cm and 128 cm). Calibration allowed to know the antennas direct coupling range position in the acquired A-scan. After, the VNA was tested by inspecting a reinforced concrete wall and results were compared with those obtained from four numerical simulations where the distance of the antennas from the wall was progressively increased. Simulations results suggest that for large antennas-wall distances, thin objects like the rebars appear as a continuous signal. The development of System LII is still in progress and additional measurement campaigns will be needed, together with further simulations to assess its imaging capabilities.

# Bibliography

---

1. PS, Ramesh, and Muruga Lal Jeyan. "Mini Unmanned Aerial Systems (UAV)-A Review of the Parameters for Classification of a Mini UAV." *International Journal of Aviation, Aeronautics, and Aerospace* 7.3 (2020): 5.
2. Cerquera, Manuel Ricardo Pérez, et al. "UAV for landmine detection using SDR-based GPR technology." *Robots Operating in Hazardous Environments* (2017): 26-55.
3. Jenssen, Rolf Ole Rydeng, Markus Eckerstorfer, and Svein Jacobsen. "Drone-mounted ultrawideband radar for retrieval of snowpack properties." *IEEE Transactions on Instrumentation and Measurement* 69.1 (2019): 221-230.
4. Eckerstorfer, Markus, et al. "UAV-Borne UWB Radar for Snowpack Surveys." (2018).
5. Wu, Kaijun, et al. "A new drone-borne GPR for soil moisture mapping." *Remote Sensing of Environment* 235 (2019): 111456.
6. Noviello, Carlo, et al. "Multilines imaging approach for mini-UAV radar imaging system." *IEEE Geoscience and Remote Sensing Letters* 19 (2021): 1-5.
7. Weib, Matthias, and J. H. G. Ender. "A 3D imaging radar for small unmanned airplanes-ARTINO." *European Radar Conference, 2005. EURAD 2005.. IEEE, 2005.*
8. Li, Chenchen J., and Hao Ling. "High-resolution, downward-looking radar imaging using a small consumer drone." *2016 IEEE International Symposium on Antennas and Propagation (APSURSI). IEEE, 2016.*
9. Colorado, Julián, et al. "An integrated aerial system for landmine detection: SDR-based Ground Penetrating Radar onboard an autonomous drone." *Advanced Robotics* 31.15 (2017): 791-808.
10. Burr, Ralf, et al. "Design and Implementation of a FMCW GPR for UAV-based Mine Detection." *2018 IEEE MTT-S International Conference on Microwaves for Intelligent Mobility (ICMIM). IEEE, 2018.*
11. Fernández, María García, et al. "Synthetic aperture radar imaging system for landmine detection using a ground penetrating radar on board a unmanned aerial vehicle." *IEEE Access* 6 (2018): 45100-45112.
12. García-Fernández, María, Yuri Alvarez-Lopez, and Fernando Las Heras. "Autonomous airborne 3D SAR imaging system for subsurface sensing: UWB-GPR on board a UAV for landmine and IED detection." *Remote Sensing* 11.20 (2019): 2357.
13. García-Fernández, María, et al. "Portable and easily-deployable air-launched GPR scanner." *Remote Sensing* 12.11 (2020): 1833.
14. Ludeno, Giovanni, et al. "Assessment of a micro-UAV system for microwave tomography radar imaging." *Remote Sensing of Environment* 212 (2018): 90-102.
15. Noviello, Carlo, et al. "Small-UAV radar imaging system performance with GPS and CDGPS based motion compensation." *Remote Sensing* 12.20 (2020): 3463.
16. Schreiber, Eric, et al. "Advanced buried object detection by multichannel, UAV/drone carried synthetic aperture radar." *2019 13th European Conference on Antennas and Propagation (EuCAP). IEEE, 2019.*
17. Wu, Kaijun, et al. "A new drone-borne GPR for soil moisture mapping." *Remote Sensing of Environment* 235 (2019): 111456.
18. Šipoš, Danijel, and Dušan Gleich. "A lightweight and low-power UAV-borne ground penetrating radar design for landmine detection." *Sensors* 20.8 (2020): 2234.
19. Saponaro, Annamaria, et al. "A UAV-GPR Fusion Approach for the Characterization of a Quarry Excavation Area in Falconara Albanese, Southern Italy." *Drones* 5.2 (2021): 40.
20. Francke, Jan, and Alexey Dobrovolskiy. "Challenges and opportunities with drone-mounted GPR." *First International Meeting for Applied Geoscience & Energy. Society of Exploration Geophysicists, 2021.*
21. Cobra Plug in GPR Web Site. Available online: <http://www.radarteam.se/index.html> (accessed on 9 June 2022)
22. Cobra Wireless GPR Web Site. Available online: <http://www.radarteam.se/cobra-wireless-gpr.html> (accessed on 9 June 2022)
23. Zond-12e GPR Web Site. Available online: <http://www.radsys.lv/en/products-soft/products/prod/7> (accessed on 9 June 2022)
24. Vergnano, Andrea, Diego Franco, and Alberto Godio. "Drone-Borne Ground-Penetrating Radar for Snow Cover Mapping." *Remote Sensing* 14.7 (2022): 1763.

25. Noviello, Carlo, et al. "An Overview on Down-Looking UAV-Based GPR Systems." *Remote Sensing* 14.14 (2022): 3245.
26. Lopez, Yuri Alvarez, et al. "Unmanned Aerial Vehicle-Based Ground-Penetrating Radar Systems: A Review." *IEEE Geoscience and Remote Sensing Magazine* (2022).
27. Groves, Paul D. "Principles of GNSS, inertial, and multisensor integrated navigation systems, [Book review]." *IEEE Aerospace and Electronic Systems Magazine* 30.2 (2015): 26-27.
28. Pavlenko, Tatiana, et al. "Wireless local positioning system for controlled UAV landing in GNSS-denied environment." 2019 IEEE 5th International Workshop on Metrology for AeroSpace (MetroAeroSpace). IEEE, 2019.
29. Santos, Nuno Pessanha, Victor Lobo, and Alexandre Bernardino. "A ground-based vision system for uav tracking." *OCEANS 2015-Genova*. IEEE, 2015.
30. Mendoza-Silva, Germán Martín, Joaquín Torres-Sospedra, and Joaquín Huerta. "A meta-review of indoor positioning systems." *Sensors* 19.20 (2019): 4507.
31. Pu, Junsong, Shuo Shi, and Xuemai Gu. "A Summary of UAV Positioning Technology in GPS Denial Environment." *International Conference on Artificial Intelligence for Communications and Networks*. Springer, Cham, 2020.
32. Schartel, Markus, et al. "An experimental study on airborne landmine detection using a circular synthetic aperture radar." *arXiv preprint arXiv:2005.02600* (2020).
33. Burr, Ralf, et al. "UAV-borne FMCW InSAR for focusing buried objects." *IEEE Geoscience and Remote Sensing Letters* 19 (2021): 1-5.
34. Catapano, Iliaria, et al. "Small multicopter-UAV-based radar imaging: Performance assessment for a single flight track." *Remote Sensing* 12.5 (2020): 774.
35. Won, I. J., Dean A. Keiswetter, and Thomas H. Bell. "Electromagnetic induction spectroscopy for clearing landmines." *IEEE Transactions on Geoscience and Remote Sensing* 39.4 (2001): 703-709.
36. Daniels, David J., ed. *Ground penetrating radar*. Vol. 1. Iet, 2004.
37. Chew, Weng Cho. *Waves and fields in inhomogeneous media*. Vol. 16. Inst of Electrical &, 1995.
38. Pastorino, Matteo. *Microwave imaging*. John Wiley & Sons, 2010.
39. Isernia, Tommaso, Vito Pascazio, and Rocco Pierri. "On the local minima in a tomographic imaging technique." *IEEE Transactions on Geoscience and Remote Sensing* 39.7 (2001): 1596-1607.
40. Ambrosanio, Michele, et al. "Performance analysis of tomographic methods against experimental contactless multistatic ground penetrating radar." *IEEE Journal of Selected Topics in Applied Earth Observations and Remote Sensing* 14 (2020): 1171-1183.
41. Bertero, M., and P. Boccacci. "Introduction to inverse problems in imaging. inst." *Physics Publ.*, London, UK (1998).
42. Catapano, Iliaria, et al. "Ground-Penetrating Radar: Operation Principle and Data Processing." *Wiley Encyclopedia of Electrical and Electronics Engineering* (1999): 1-23.
43. Persico, Raffaele. *Introduction to ground penetrating radar: inverse scattering and data processing*. John Wiley & Sons, 2014.
44. Persico, Raffaele, and Francesco Soldovieri. "Effects of background removal in linear inverse scattering." *IEEE Transactions on Geoscience and Remote Sensing* 46.4 (2008): 1104-1114.
45. Solimene, Raffaele, et al. "Ground clutter removal in GPR surveys." *IEEE Journal of Selected Topics in Applied Earth Observations and Remote Sensing* 7.3 (2013): 792-798.
46. Garcia-Fernandez, Maria, et al. "SVD-based clutter removal technique for GPR." 2017 IEEE International Symposium on Antennas and Propagation & USNC/URSI National Radio Science Meeting. IEEE, 2017.
47. Milbert, Dennis. "Dilution of precision revisited." *Navigation* 55.1 (2008): 67-81.
48. Kaplan, E.; Hegarty, C.J. *Understanding GPS—Principles and Applications*, 2nd ed.; Artech House: Boston, MA, USA; London, UK, 2006.
49. Farrell, Jay. *Aided navigation: GPS with high rate sensors*. McGraw-Hill, Inc., 2008.
50. Moreira, Joao R. "A new method of aircraft motion error extraction from radar raw data for real time motion compensation." *IEEE Transactions on Geoscience and Remote Sensing* 28.4 (1990): 620-626.
51. Härkegård, Ola, and S. Torkel Glad. "Flight control design using backstepping." *IFAC Proceedings Volumes* 34.6 (2001): 283-288.
52. Persico, Raffaele, et al. "Two-dimensional linear inversion of GPR data with a shifting zoom along the observation line." *Remote Sensing* 9.10 (2017): 980.
53. Gennarelli, Gianluca, et al. "A low frequency airborne GPR system for wide area geophysical surveys: The case study of Morocco Desert." *Remote Sensing of Environment* 233 (2019): 111409.
54. Soldovieri, Francesco, et al. "Forward-looking radar imaging: A comparison of two data processing strategies." *IEEE Journal of Selected Topics in Applied Earth Observations and Remote*

- Sensing 10.2 (2016): 562-571.
55. Balanis, Constantine A. *Advanced engineering electromagnetics*. John Wiley & Sons, 2012.
  56. Catapano, Ilaria, et al. "Contactless ground penetrating radar imaging: State of the art, challenges, and microwave tomography-based data processing." *IEEE Geoscience and Remote Sensing Magazine* (2021).
  57. Persico, Raffaele. "On the role of measurement configuration in contactless GPR data processing by means of linear inverse scattering." *IEEE transactions on antennas and propagation* 54.7 (2006): 2062-2071.
  58. Catapano, Ilaria, et al. "Tomographic airborne ground penetrating radar imaging: Achievable spatial resolution and on-field assessment." *ISPRS journal of photogrammetry and remote sensing* 92 (2014): 69-78.
  59. R. Solimene, F. Soldovieri, G. Prisco, and R. Pierri, "Three-dimensional microwave tomography by a 2-D slice-based reconstruction algorithm," *IEEE Geosci. Remote Sens. Lett.*, vol. 4, no. 4, pp. 556–560, Oct. 2007, doi: 10.1109/LGRS.2007.900741
  60. Catapano, Ilaria, Carlo Noviello, and Francesco Soldovieri. "Down-Looking Airborne Radar Imaging Performance: The Multi-Line and Multi-Frequency." *Remote Sensing* 13.23 (2021): 4897.
  61. Gennarelli, Gianluca, Ilaria Catapano, and Francesco Soldovieri. "Reconstruction capabilities of down-looking airborne GPRs: The single frequency case." *IEEE Transactions on Computational Imaging* 3.4 (2017): 917-927.
  62. Available online: <https://www.humatics.com/products/scholar-radar/> (accessed on 28 February 2020).
  63. Standard, G.S.P. Available online: <https://trade.ec.europa.eu/tradehelp/standard-gsp> (accessed on 28 February 2020).
  64. Esposito, Giuseppe, et al. "The UAV radar imaging prototype developed in the frame of the VESTA project." 2020 IEEE Radar Conference (RadarConf20). IEEE, 2020.
  65. Available online: <https://topview.it/en/> (accessed on 20 October 2020).
  66. Proakis, John G. *Digital signal processing: principles algorithms and applications*. Pearson Education India, 2001.
  67. Scherzer, Otmar, ed. *Handbook of mathematical methods in imaging*. Springer Science & Business Media, 2010.
  68. Richards, M.A. *Fundamentals of Radar Signal Processing*; Tata McGraw-Hill Education: New York, NY, USA, 2005.
  69. Cheney, M.; Borden, B. *Fundamentals of Radar Imaging*; Siam: Philadelphia, PA, USA, 2009; Volume 79
  70. Gašparović, Mateo, and Luka Jurjević. "Gimbal influence on the stability of exterior orientation parameters of UAV acquired images." *Sensors* 17.2 (2017): 401.
  71. Pérez, Juan Antonio, et al. "Accuracy and effectiveness of orthophotos obtained from low cost UASs video imagery for traffic accident scenes documentation." *Advances in Engineering Software* 132 (2019): 47-54.
  72. Available online: [http://www.rtklib.com/rtklib\\_document.htm](http://www.rtklib.com/rtklib_document.htm) (accessed on 28 February 2020).
  73. <https://coppermountaintech.com/vna/s5085-compact-2-port-vna/>
  74. <https://uavsystemsinternational.com/products/aurelia-x6-standard>
  75. [https://www.amazon.com/dp/B0781FH7T1?psc=1&ref=ppx\\_yo2ov\\_dt\\_b\\_product\\_details](https://www.amazon.com/dp/B0781FH7T1?psc=1&ref=ppx_yo2ov_dt_b_product_details)
  76. [https://www.digikey.com/en/products/detail/u-blox/EVK-M8T-0/6150726?utm\\_adgroup=xGeneral&utm\\_source=google&utm\\_medium=cpc&utm\\_campaign=Dynamic%20Search\\_EN\\_Product&utm\\_term=&utm\\_content=xGeneral&gclid=Cj0KCQjw8O-VBhCpARIsACMvVLP75zcB5PSjIXNK3ADE2Ih7e6nHaEbrhzPMrdbNqzd1C8h\\_PasQPkaAlp-EALw\\_wcB](https://www.digikey.com/en/products/detail/u-blox/EVK-M8T-0/6150726?utm_adgroup=xGeneral&utm_source=google&utm_medium=cpc&utm_campaign=Dynamic%20Search_EN_Product&utm_term=&utm_content=xGeneral&gclid=Cj0KCQjw8O-VBhCpARIsACMvVLP75zcB5PSjIXNK3ADE2Ih7e6nHaEbrhzPMrdbNqzd1C8h_PasQPkaAlp-EALw_wcB)
  77. [https://www.amazon.com/dp/B09G9B4P3B?psc=1&ref=ppx\\_yo2ov\\_dt\\_b\\_product\\_details](https://www.amazon.com/dp/B09G9B4P3B?psc=1&ref=ppx_yo2ov_dt_b_product_details)
  78. [https://www.amazon.com/TalentCell-Rechargeable-1200mAh-Multi-led-indicator/dp/B00ME3ZH7C/ref=sr\\_1\\_2?keywords=talentcell&qid=1656535464&sr=8-2](https://www.amazon.com/TalentCell-Rechargeable-1200mAh-Multi-led-indicator/dp/B00ME3ZH7C/ref=sr_1_2?keywords=talentcell&qid=1656535464&sr=8-2)
  79. Available online: <https://zoom.earth/> (accessed on 9 June 2022)
  80. Ludeno, Giovanni, et al. "A comparison of linear inverse scattering models for contactless GPR imaging." *IEEE Transactions on Geoscience and Remote Sensing* 58.10 (2020): 7305-7316.
  81. Renga, A., Fasano, G., Accardo, D., Grassi, M., Tancredi, U., Rufino, G., & Simonetti, A. (2013). Navigation facility for high accuracy offline trajectory and attitude estimation in airborne applications. *International Journal of Navigation and Observation*, 2013.